Nanoporous Gold-Based Sensing

Francesco Ruffino * and Maria Grazia Grimaldi

Dipartimento di Fisica e Astronomia "Ettore Majorana", Università di Catania and MATIS CNR-IMM, via S. Sofia 64, 95123 Catania, Italy; mariagrazia.grimaldi@ct.infn.it
* Correspondence: francesco.ruffino@ct.infn.it

Abstract: In recent years, the field of nanoporous metals has undergone accelerated developments as these materials possess high specific surface areas, well-defined pore sizes, functional sites, and a wide range of functional properties. Nanoporous gold (NPG) is, surely, the most attractive system in the class of nanoporous metals: it combines several desired characteristics as occurrence of surface plasmon resonances, enormous surface area, electrochemical activity, biocompatibility, in addition to feasibility in preparation. All these properties concur in the exploitatiton of NPG as an efficient and versatile sensing platform. In this regard, NPG-based sensors have shown exceptional sensitivity and selectivity to a wide range of analytes ranging from molecules to biomolecules (and until the single molecule detection) and the enormous surface/volume ratio was shown to be crucial in determining these performances. Thanks to these characteristics, NPG-based sensors are finding applications in medical, biological, and safety fields so as in medical diagnostics and monitoring processes. So, a rapidly growing literature is currently investigating the properties of NPG systems toward the detection of a multitude of classes of analytes highlighting strengths and limits. Due to the extension, complexity, and importance of this research field, in the present review we attempt, starting from the discussion of specific cases, to focus our attention on the basic properties of NPG in connection to the main sensing applications, i.e., surface enhanced Raman spectroscopy-based and electrochemical-based sensing. Owing to the nano-sized pore channels and Au ligaments, which are much smaller than the wavelength of visible light (400–700 nm), surface plasmon resonances of NPG can be effectively excited by visible light and presents unique features compared with other nanostructured metals, such as nanoparticles, nanorods, and nanowires. This characteristics leads to optical sensors exploiting NPG through unique surface plasmon resonance properties that can be monitored by UV-Vis, Raman, or fluorescence spectroscopy. On the other hand, the catalytic properties of NPG are exploited electrochemical sensors are on the electrical signal produced by a specific analyte adsorbed of the NPG surface. In this regard, the enourmous NPG surface area is crucial in determining the sensitivity enhancement. Due to the extension, complexity, and importance of the NPG-based sensing field, in the present review we attempt, starting from the discussion of specific cases, to focus our attention on the basic properties of NPG in connection to the main sensing applications, i.e., surface enhanced Raman spectroscopy-based and electrochemical-based sensing. Starting from the discussion of the basic morphological/structural characteristics of NPG as obtained during the fabrication step and post-fabrication processes, the review aims to a comprehensive schematization of the main classes of sensing applications highlighting the basic involved physico-chemical properties and mechanisms. In each discussed specific example, the main involved parameters and processes governing the sensing mechanism are elucidated. In this way, the review aims at establishing a general framework connecting the processes parameters to the characteristics (pore size, etc.) of the NPG. Some examples are discussed concerning surface plasmon enhanced Uv-Vis, Raman, fluorescence spectroscopy in order to realize efficient NPG-based optical sesnors: in this regard, the underlaying connections between NPG structural/morphological properties and the optical response and, hence, the optical-based sensing performances are described and analyzed. Some other examples are discussed concerning the exploitation of the electrochemical characteristics of NPG for ultra-high sensitivity detection of analytes: in this regard, the key parameters determing the NPG activity and

selectivity selectivity toward a variety of reactants are discussed, as high surface-to-volume ratio and the low coordination of surface atoms. In addition to the use of standard NPG films and leafs as sensing platforms, also the role of hybrid NPG-based nanocomposites and of nanoporous Au nanostructures is discussed due to the additional increase of the electrocatalytic acticvity and of exposed surface area resulting in the possible further sensitivity increase.

Keywords: nanoporous gold; optical sensing; plasmonics; SERS; electrochemical sensing; electrocatalysis

1. Introduction

The fabrication of sensing devices based on metal nanostructures has received a great attention by the scientific community in the last years due to their unprecedented performances, in terms of sensitivity, limit of detection, selectivity, chemical and structural flexibility [1–4]. In this framework, Au and Ag nanostructures and nanostructured materials represent key elements in order to produce innovative cutting-edge sensors finding applications in any technological field. This characteristic relies in some peculiar properties as enormous surface area, plasmonic behavior, and biocompatibility [1–4]. The successful development of nanomaterials is strictly related to the capability in fabricating shape-, size-, and structure-designed nanostructures [5]. These nanomaterials can be, then, integrated into the final functional devices. However, to be industrially attractive, the nanofabrication processes need to be simple, versatile, cost-effective, with high throughput and should allow the easy control of the nanomaterial's morphology and structure. In fact, referring, in particular, to the sensing applications, complex-morphology metal nanostrucutres are highly desirable in order to enhance their exposed surface area and plasmonic response (in which the enhancement of the incident electromagnetic radiation by the so-called hot-spot effect which is of paramount importance in Surface Enhanced Raman Spectroscopy, SERS) [1–13]. Plasmonic effects in metal nanostructures [14–16], for example, greatly renewed the interest in the use of these systems: the collective oscillation of electrons in a metal nanostructure resonates with particular wavelengths of light, generating the localized surface plasmon resonance (LSPR). The LSPR results in absorption and scattering of incoming photons. Absorption leads to photothermal generation of heat, photoluminescence, and quenching of fluorophores in close proximity. Scattering results in reflected photons and its amplification of the local electromagnetic field can enhance fluorescence, phosphorescence, and Raman scattering. These optical properties make plasmonic nanostructures ideal candidates for sensing, biomedical, drug delivery applications [4]. Plasmonic nanostructures are particularly suitable for Raman-based sensing because of the massive enhancement factor that can be achieved with precisely shaped particles. When a Raman-active dye is adsorbed to the surface of the plasmonic nanomaterials, fluorescence is quenched, minimizing its competing signal. Raman-based detection can be performed with label-free assays or Raman reporters. Label-free detection is often utilized for the detection of small molecules [4]. In addition, regarding sensing applications, the catalytic ability of metal nanomaterials has proven to be very powerful in the electrochemical detection of analytes [1–4]. Electrochemical sensors are based on the electrical signal produced by a specific analyte [17–19]. The increased catalytic activity of nanomaterials in comparison to the corresponding bulk materials is due to the highly curved morphology of the nanoscale material, determining a high density of steps, holes, and kinks [17–20]. These areas are host to low coordination atoms, in contrast to the normal high coordination associated with a close-packed surface. These low coordination sites interact more strongly with target molecules and these molecues, also in a very low amount, once adsorbed on the nanomaterial surface, determine a significant change in the electrical properties of the system.

In order to further improve the sensing properties of metal nanomaterials, the highest possible surface area is required to enhance the material reactivity to probing molecules. In this regard, nanoporous metals acquired the key role towards the development of the best-performance sensing

devices [21,22]. The field of nanoporous metals has undergone accelerated developments in the last years as these materials possess enormous specific surface area, well-defined pore sizes, and functional sites [20–22]. In addition, one of the reasons for the feasibility of nanoporous metals relies in the relative simplicity of preparation (exploiting, for example, a dealloying approach) allowing to generate bulk samples of a few millimeters (or even larger) which are porous on nanoscale, thus avoiding more expensive techniques such as lithographic-based ones. Nanoporous metals present, also, chemical and structural flexibility and the fabrication methodologies allow, often, the wide-range tuning of the pores and ligaments sizes from ~5 nm to several microns, without losing the typical bicontinuous structure of the material. Nanoporous gold (NPG) is, surely, the most attractive system in the class of nanoporous metals: it combines several desired characteristics as occurrence of LSPR, high surface area (~10 m^2/g), electrochemical activity, biocompatibility, in addition to feasibility in preparation [20–26].

NPG is a three-dimensional nanostructured bulk material. It is typically generated from an alloy of gold (Au) and a less noble metal, such as for example Silver (Ag) or Copper (Cu). With the chemical or electrochemical removal (through a "dealloying" approach) of the less noble component, the remaining Au undergoes a "self-organization" process forming a porous and continuous three-dimensional network of interconnected ligaments with peculiar optical, electrical, mechanical, reactivity properties [20–46].

Depending on the preparation conditions for the NPG, the pore sizes can vary from 5 nm (smaller sizes) to 30 or 40 nm (larger sizes). Thanks to its high porosity, this material has a specific surface in the "range" of 10 m^2g^{-1}. The pore volume mainly depends on the concentration of less noble metal in the starting alloy. With the emergence of nanotechnology in the late 1990s and early 2000s, many researchers have used the potential of this material for a variety of technological aspects. Two of the characteristics that make NPG so "special" among nanoporous materials are the relative ease and inexpensive method of preparation using corrosion techniques and its structural and chemical flexibility. So, recent years have seen a plethora of reports on the use of NPG for innovative sensing devices ranging from SERS-based [20–26,47–73] and electrochemical-based [20–26,74–87] sensing to amperometric-based and chemoresistive-based sensing [20–26,88–92]. The dealloying technique [20–24], typically used for the production of NPG, has been very successful, because it is a simple, versatile, and inexpensive method to manufacture NPG with a three-dimensional bi-continuous structure. This technique is much simpler and more versatile than other techniques (based for example on the use of appropriate "templates") which, while providing precise control over the size and morphology of porosity, generally require longer fabrication times. The NPG produced by the dealloying technique has unique structural properties such as mechanical rigidity, electrical conductivity, and stability.

NPG-based sensors have shown exceptional sensitivity and selectivity to a wide range of analytes ranging from molecules to biomolecules (and until the single molecule detection) and the enormous surface/volume ratio was shown to be crucial in determining these performances. In this regard, recently, a further development was identified in the use of nanoporous Au nanostructures (as nanoparticles and nanowires [92–103]), in addition to nanoporous Au films and leafs, due to the additional increase of the exposed surface area reaching, also, the value of 10^5 g/m^2 [97] resulting in the possible further sensitivity increase.

Thanks to these characteristics, NPG-based sensors are finding applications in medical, biological and safety fields so as in medical diagnostics and monitoring processes. So, a rapidly growing literature is currently investigating the properties of NPG systems toward the detection of a multitude of classes of analytes highlighting strengths and limits. In this sense, Table 1 reports a short and exemplificative list of the specific NPG-based systems with the corresponding application and reference. This literature shows the growing importance of NPG-based sensing and the importance to design NPG-based structures with a more complex morphology than standard bulk leafs (Figure 1a,b) and films (Figure 1c) as NPG nanoparticles (Figure 1d), NPG nanowires (Figure 1e), NPG leafs decorated by nanoparticles (Pt nanoparticles in Figure 1f), and NPG patterned microstructures (column in Figure 1g) so as to obtain structured-designed materials with improved performances.

Table 1. This table summarizes some recent literature in which nanoporous gold (NPG)-based systems are used in sensing applications. The table groups the literature works on the basis of Surface Enhanced Raman Spectroscopy (SERS-), electrochemical-, amperometric-based sensing. The table is not exhaustive; however, it shows the wide-range of used NPG-based sensing systems and the corresponding wide range of analytes which can be detected by these systems.

System	Application	Reference
Nanoporous Au Leafs from AuAg dealloying	SERS detection (Probe molecules: crystal violet, rhodamine-6G)	[53,55,61–63,73]
Nanoporous Au Leafs from AuAg dealloying	Fluorescence enhancement and SERS detection (Probe molecules: cyanine-3, rhodamine-6G)	[56,64]
Nanoporous Au Leafs from AuAg dealloying	SERS detection (Hg^{2+})	[57]
Nanoporous Au Leafs from AuAg dealloying+Imprint patterning	SERS detection (Probe molecule: benzethiol)	[59]
Nanoporous Au Leafs from AuAg dealloying	SERS detection (Human serum albumine)	[65]
Nanoporous Au Films from Oblique Angle Deposition	SERS detection (Biotin-streptavidin)	[66]
Nanoporous Au Leafs from AuAg dealloying	Electrochemical Detection (p-nitrophenol)	[74]
Nanoporous Au Leafs from AuAg dealloying	Electrochemical detection (hydrogen peroxide)	[75]
Nanoporous Au Leafs from AuAg dealloying	Electrochemical detection (glucose)	[76]
Nanoporous Au Films from AuAg dealloying	Electrochemical detection (DNA)	[77]
Nanoporous Au Leafs from AuAg dealloying	Electrochemical detection (glucose oxidase)	[78]
Nanoporous Au Leafs decorated by Pt nanoparticles	Electrochemical detection (glucose)	[82]
Nanoporous Au Leafs decorated by Pt nanoparticles	Electrochemical detection (methanol)	[83]
Nanoporous gold/copper oxide nanohybrids	Electrochemical detection (glucose)	[84]
Nanoporous Au Leafs decorated by Au nanoparticles	Electrochemical detection (DNA)	[85]
Nanoporous Au Leafs from AuAg dealloying	Amperometric detection (ethanol, glucose)	[86]
Nanoporous Au Films from AuSi dealloying	Amperometric detection (phenol, catechol)	[87]
Nanoporous Au Leafs from AuAg dealloying	Amperometric detection (nitrite)	[88]
Nanoporous Au Films by electrochemical deposition	Amperometric detection (glucose)	[89,90]
Nanoporous Au coated by Cu by electrochemical deposition	Amperometric detection (glucose)	[91]
Nanoporous gold nanowire by AuAg dealloying	Chemiresistive detection (octadecanethiol)	[92]

| Nanoporous Au Disks by top-down lithographic nanosphere patterning and bottom-up dealloying | SERS detection (Octadecanethiol Self-Assembled Monolayer) | [93] |
| Nanoporous Au disks | Fluorescence enhancement (cancer biomarker detection) | [94] |

Due to the extension, complexity, and importance of this research field, in the present review we attempt, starting from the discussion of specific cases, to focus our attention on the basic properties of NPG in connection to the main sensing applications, i.e., SERS-based and electrochemical-based sensing. Starting from the discussion of the basic characteristics of NPG, the review aims to a comprehensive schematization of the main classes of sensing applications highlighting the basic involved mechanisms and processes. In each discussed specific example, the main involved parameters and processes governing the sensing mechanism are elucidated. In this way, the review aims at establishing a general framework connecting the processes parameters to the characteristics (pore size, etc.) of the NPG. This could be a step ahead towards the use of NPG for the controlled design and fabrication of sensing devices with desired performances. In particular, the review is organized as follows:
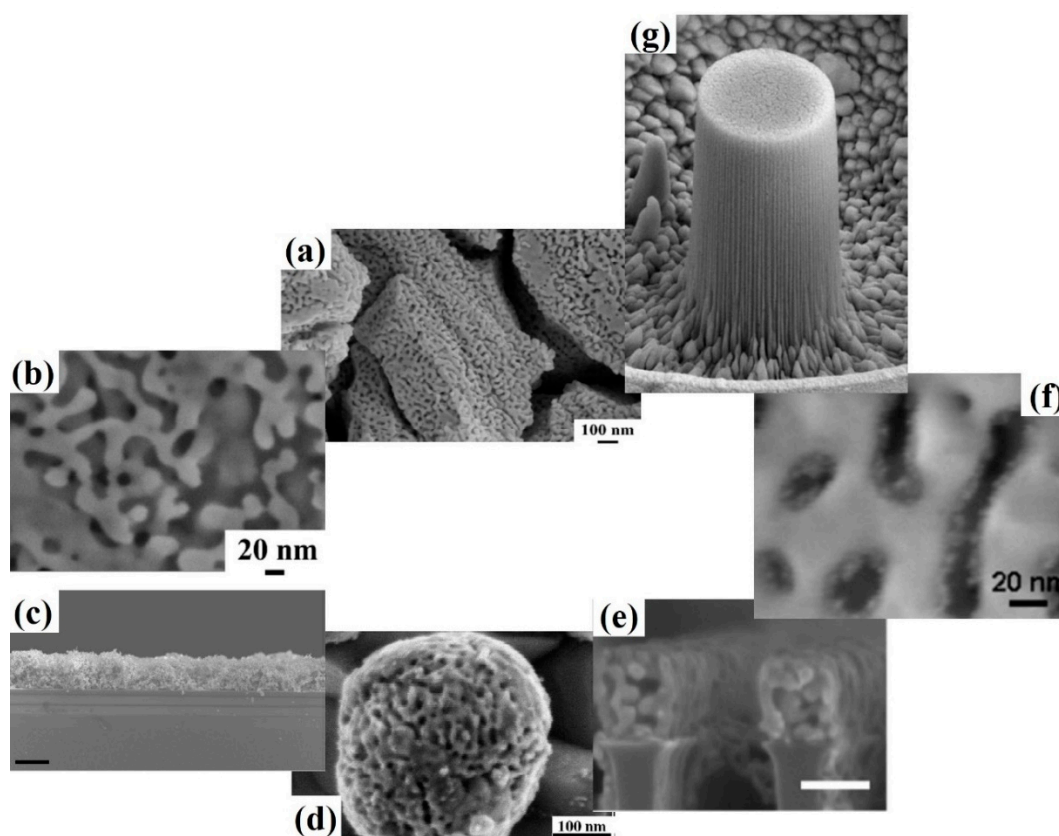

Figure 1. Examples of NPG-based structures: plan-view scanning electron microscopy images of (**a**) cracked NPG-leaf and (**b**) magnified image of the surface of NPG-based leaf. Reproduced with permission from [28]. Copyright Elsevier, 2016; (**c**) cross-sectional scanning electron microscopy image of a NPG film on a substrate, with the scale bar 20 μm. Reproduced with permission from [29]. Copyright Nature, 2013; (**d**) plan-view scanning electron microscopy image of NPG nanoparticles. Reproduced with permission from [30]. Copyright Elsevier, 2017; (**e**) cross-sectional scanning electron microscopy image of NPG-based nanowires, with scale bar 100 nm. Reproduced with permission from [103]. Copyright American Chemical Society, 2016; (**f**) plan-view scanning electron microscopy image of NPG-based leaf decorated by Pt nanoparticles. Reproduced with permission from [83]. Copyright American Chemical Society, 2007; (**f**) NPG-based column with diameter of 3.6 μm and height of 6.9 μm. Reproduced with permission from [31]. Copyright American Physical Society, 2006.

The first part (Section 2) is devoted to a synthetic discussion of the possibility to controllably change the morphological characteristic of NPG during the fabrication steps or by specific processes following fabrication. Starting from general concepts and descriptions, the attention is focused on the phenomena and parameters determining characteristics evolution (pore size, porosity, etc.) as a function of process parameters. The role of the process parameters on the morphological/structural characteristics are particularly highlighted so as to establish general working ranges for the fabrication process impacting, then, on the sensing properties. The second part (Section 3) focuses on the illustration and discussion of some seminal literature experimental works on the use of various NPG systems (leafs, films, nanostructures, nanostructured composites) for various sensing applications based on the two main classes of sensing approaches: SERS-based sensing and electrochemical-based sensing. In addition, in each case, the effect of the NPG morphology/structure on the sensing results is discussed so to draw insights on possible evolutions by further morphology/structure improvements. The third part (Section 4) describes the latest developments regarding fabrication of NPG nanostructured systems and their potential use in sensing applications to reach cutting-edge unprecedent performances and focuses on future perspectives and challenges. Finally, the concluding part (Section 5) summarizes main conclusions and discusses open points.

2. Nanoporous Gold: General Considerations

There are several approaches available for the production of NPG [20–25]. The easier and most used method used to fabricate NPG is, however, by chemical or electrochemical dealloying [25,104]. By means of this process, one or more components are selectively leached from a homogeneous, single phase alloy alloy, leaving a residual nanoporous structure for the remaining metal. For the production of NPG, Ag-Au (in particular) and Cu-Au alloys are used as the starting mixtures, from which, after removing the less-noble metal (Ag or Cu), see the scheme in Figure 2, the characteristic three-dimensional bicontinuous, self-affine, nanoporous morphology for the residual Au is obtained, see Figure 3.

Au-Cu thin film deposition → **Dealloying in nitric acid** → **Nanoporous Au thin film**

Figure 2. Schematic picture of the free-corrosion dealloying process of Au-Cu alloy film for the production of NPG film. Reproduced with permission from [39]. Copyright American Chemical Society, 2015.
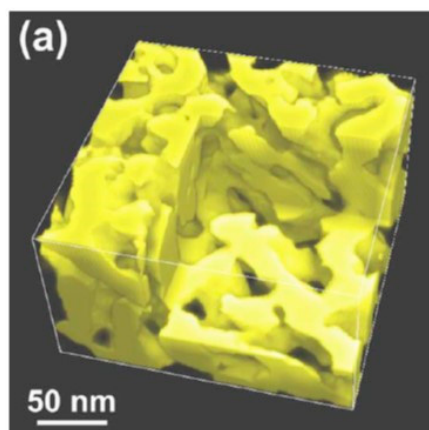
Figure 3. Three-dimensional tomographic reconstruction of NPG. This image reveals the internal bicontinuous structure of NPG. Reproduced with permission from [38]. Copyright American Physical Society, 2008.

In the case of Ag-Au alloys, Ag can easily be removed by etching the alloy sample in 50%–75% HNO$_3$ (dealloying by free corrosion, being Ag easily oxidized to a nitrate salt by HNO$_3$ whereas Au is not) or by applying an electrochemical driving force in a less corrosive electrolyte (electrochemical dealloying) [20–25,48–52]. In the free corrosion dealloying, the less-noble metal is, typically, etched away from the alloy in a short amount of time, some minutes. The electrochemical dealloying is performed by using an electrochemical cell involving, typically, the etching a Ag-Au alloy in which the alloy surface works as the working electrode and a noble metal works as the counter electrode. A constant voltage is applied to the cell for a defined time whereas the voltage value is determined by the oxidizing range for the metal that needs to be removed. The metal that is being oxidized is losing electrons to the working electrode and is being deposited onto the counter electrode. During dealloying, process parameters as dealloying time, dealloying temperature or applied potential can be controlled to tune the pore sizes. The NPG average pore size increases by increasing the system temperature during dealloying and can also change in dependence of exposure time and type of acid. However, regarding the Ag-Au alloy, the nitric acid dealloying is the most common process to obtain NPG since it is a straightforward process that provides consistent results and producing a NPG surface which is clean and particularly desirable for surface electrode reactions. In addition, the pore volume depends on the amount of the less noble element in the starting alloy. This approach works for Ag-Au bulk alloy leafs (i.e., thin foils, typically 50–100 μm thick, made by hammering) [20–25,28,31–38,41–45], films [20–25,29,39,40], and nanostructures [20–25,30,92–103]. Several excellent reviews describe the thermodynamics and kinetic processes involved in the dealloying mechanism of alloys toward the formation of NPG [20–25,51,52,104]. Here we focus, instead, on methodologies and approaches to control the NPG morphological and structural characteristics.

As an example [24], Figure 4a shows an optical image of a Ag-Au 12 carat leaf, 1:1 ratio by weight, and Figure 4b reports the optical image of the same leaf after dealloying in concentrated HNO$_3$ for 15 min. Figure 4c–e report scanning electron microscopy images of the surface of the dealloyed leaf with increasing magnification from (c) to (e). The typical nanoporous structure is clearly observable as composed by Au ligaments (with width until 2 nm) and pores; the inset in (c) shows a region on the sample surface where a grain boundary is located. As a further example [24], Figure 5 shows a series of plan-view and cross-sectional scanning electron microscopy images of NPG films obtained on the surface of Ag-Au alloy leafs produced by leaving the leafs immersed in HNO$_3$ for increasing time (5, 15, 60 min, 1 day, 5 and 10 days). The dealloying process is complete after 5 minuted of immersion [24], however the continued immersion of the sample in HNO$_3$ results in pore coarsening so that while the average pores diameter is about 8 nm in the sample after 5 min of immersion, the average pores diameter increases to about 20 nm after 15 min of immersion and to about 40 nm after 10 days of immersion.
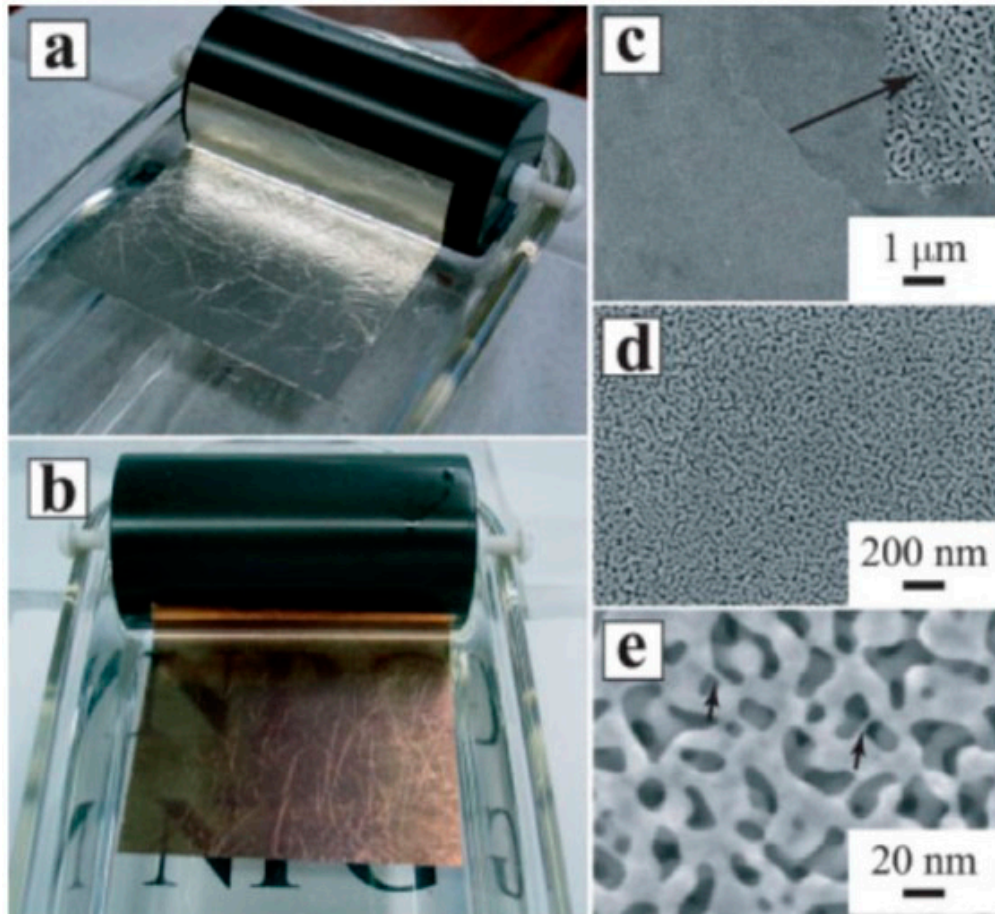
Figure 4. (**a**) shows an optical image of a Ag-Au 12 carat leaf, 1:1 ratio by weight, and (**b**) reports the optical image of the same leaf after dealloying in concentrated HNO_3 for 15 min; (**c–e**) report scanning electron microscopy images of the surface of the dealloyed leaf with increasing magnification from (**c–e**). The typical nanoporous structure is clearly observable as composed by Au ligaments (with width until 2 nm) and pores; the inset in (**c**) shows a region on the sample surface where a grain boundary is located. Reproduced with permission from [24]. Copyright Wiley, 2004.
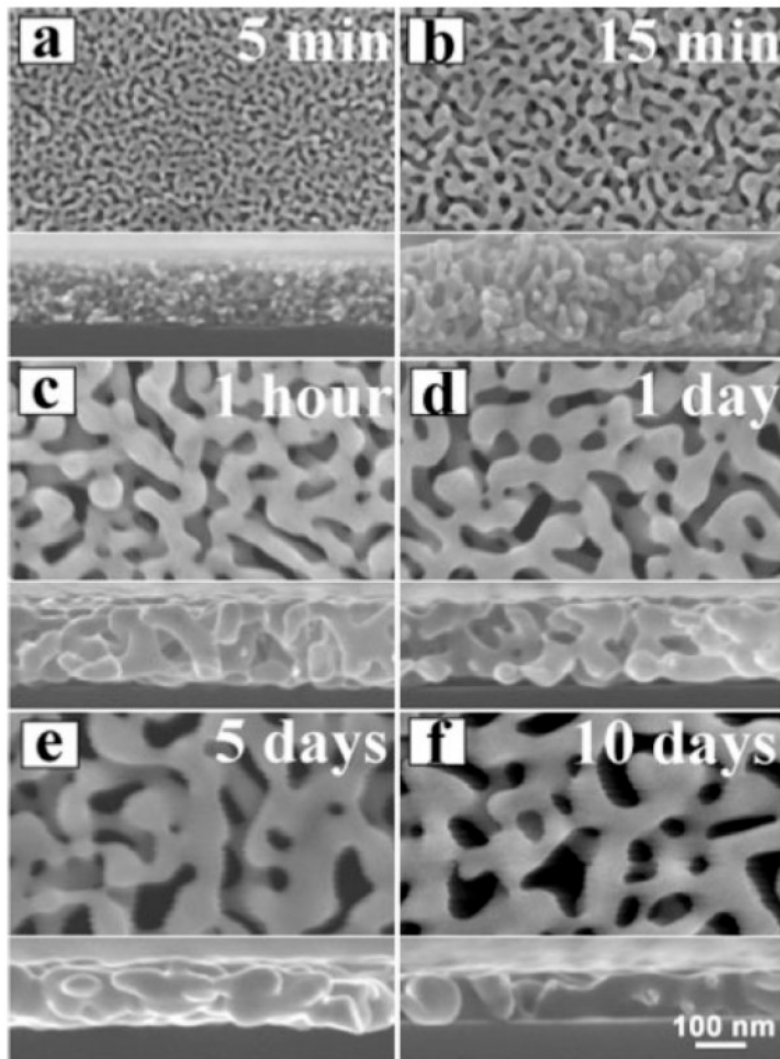
Figure 5. Plan-view and cross-sectional scanning electron microscopy images (**a**–**f**) of the resulting nanoporous structure of Au leaf after immersion of the Ag-Au leaf in HNO_3 for 5, 15, 60 min, 1 day, 5 and 10 days. Reproduced with permission from [24]. Copyright Wiley, 2004.

In particular, from a quantitative point of view, Qian et al. [32] studied the kinetics of the pore formation by dealloying in NPG leafs. Their results are summarized in Figure 6: they used $Ag_{65}Au_{35}$ (atomic ratio) leafs and produced, on the leaf's surface, NPG films by dealloying the leafs in 70% (mass ratio) HNO_3 for various times and temperatures (−25 °C, 0, 25 °C).
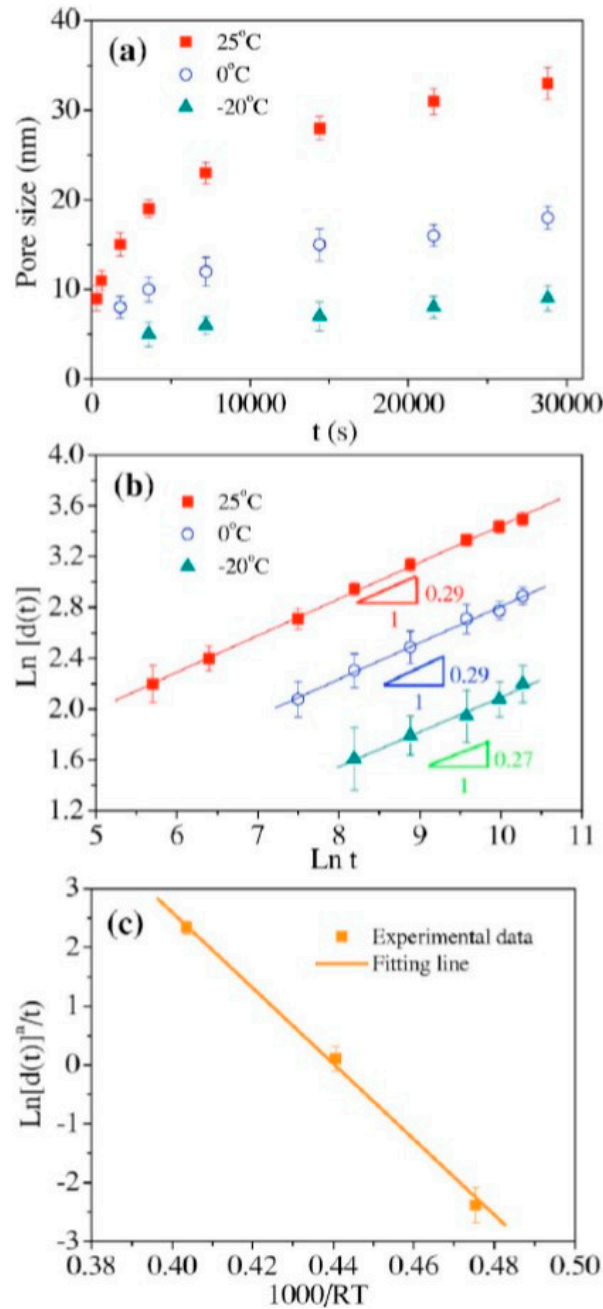
Figure 6. Characteristics of the pores size for the pores formed in $Ag_{65}Au_{35}$ (atomic ratio) leafs by dealloying in 70% (mass ratio) HNO_3 for various times and temperatures (−25 °C, 0 °C, 25 °C), whereas the NPG is formed as a film on the surface of the leaf. (**a**) Evolution of the mean pore size d with dealloying time and temperature of the HNO_3 etching slution; (**b**) Measurement of the coarsening exponent n by plotting lnd vs. lnt at each etching temperature. (**c**) Measurement of the activation energy for the pore formation by plotting $[(lnd)^n]/t$ versus 1000/RT. Reproduced with permission from [32]. Copyright American Physical Society, 2007.

According to the authors [32], the Ag chemical selective dissolution leads to the self-assembly of Au atoms at alloy/electrolyte interface resulting in pore sizes increase with etching time and temperature. In particular, the behavior of the mean pores size d versus the dealloying time t at each temperature (temperature of the HNO_3 etching solution), as plotted in Figure 6a, suggested to the authors an underlying kinetic process that the coarsening rate similar to the isothermal grain growth in polycrystalline materials [105]. This observation, therefore, suggested to the authors the following relationship between d and t

$$d^n = Kt = k_0 D_s t = k_0 D_0 [\exp(-E_A/RT)]t \tag{1}$$

being d the mean pore size, n the coarsening exponent, t the etching time, and K the coarsening rate (which is the proportionality constant between d^n and t). In addition, $K = k_0 D_s$ being D_s the temperature-dependent diffusion coefficient for the Au atoms in the acid and k_0 the proportionality constant between K and D_s. Finally, D_s can be expressed in an Arrhenius form, i.e., as $D_s = D_0 \exp(-E_A/RT)$ with T the etching temperature, R the gas constant, E_A the activation energy for the Au atoms diffusion process (which can be identified, hence, with the activation energy for the pores formation). The fit of the experimental data in Figure 1b allows to estimate, for each etching temperature T, n~4 indicating a process which is limited by the surface relaxation of roughened metals in solutions. The Arrhenius plot in Figure 1c, then, allows to estimate the activation energy for the processa s E_A~63.4 kJ/mol which is very close to the value for the activation energy for the surface diffusion of Au atoms in acid, and suggesting, so, that the pores coarsening process is controlled by the Au atoms diffusion at the alloy/electrolyte interface. The strong temperature dependence is justified by the exponential dependence of the diffusion coefficient. On the basis of the diffusion-controlled coarsening mechanism, D_s can be expressed as

$$D_s = d^4 kT/32\gamma ta^4 \tag{2}$$

being k the Boltzmann constant, γ the metal surface energy and a the metal lattice parameter. So, at -20 °C, 0 °C, 20 °C, the authors were able to estimate D_s as 9.0×10^{-22}, 1.5×10^{-20}, 2.0×10^{-19} m²/s, respectively. This strong temperature dependence for the pores size evolution is in agreement with kinetic Monte Carlo simulation in which lower diffusivity of Au atoms at the solid/electrolyte interfaces leads to a smaller nanoporous size [106]. These data clearly show the possibility to controllably tune the NPG morphological characteristics by controlling the dealloying process parameters (time and temperature).

There have been, also, several efforts in controlling the morphology of NPG, for example by inducing coarsening of the ligaments (ligament size refers to the dimensions of the regions that surround the pores on the surface of the structure) and the pores either by thermal treatments. Thermal annealing studies have been performed on NPG leafs and films to study the porosity changes as well as the pore size distribution across the sample. As an example, Chen et al. [33], after producing NPG films, studied the effect of post-annealing atmosphere on the evolution of the porous morphology. In particular, the authors used $Au_{35}Ag_{65}$ (at.%) films with a thickness of 100 nm to produce NPG through chemical dealloying in 65% (wt.%) HNO_3 and then these samples were annealed for two hours in the temperature range 100–600 °C under the atmospheres of oxidative air (O_2), inert Ar and reductive CO gas (5% CO + 95% Ar), respectively. As an example, Figure 7 reports some representative scanning electron microscopy images of the surface of the NPG films after annealing at different temperatures and under the different atmospheres. Figure 8 reports, hence, the mean ligaments and pores size as a function of the annealing temperature under the different annealing atmospheres: both the pores and Au ligaments grow exponentially as a function of annealing temperature. However, the annealing atmosphere significantly influences the growth of the ligaments and pores: generally, the authors find that NPG films posses the higher stability in the reductive atmosphere (CO) and the lower stability in oxidative air. In particular, the NPG films thermally processed in air show a significant pores growth at 200 °C while at 300 °C the porous morphology is lost; in air, in fact, the surface oxidation limits the diffusion of the oxygen into the interior of the NPG, however the thermal-induced coarsening of NPG films in air is due to the desorption of O_2 from the NPG surface above 200 °C and at 300 °C the NPG film collapses. In this condition, the three-dimensional porous structure disappears and an apparent ligament fusion is observed above 300 °C, as indicated by arrows in Figure 7b,c. The NPG films processed in CO environment maintain the porous structure until 600 °C. With respect to the annealing in air, the annealing of the NPG films in CO gas leads to the stabilization of the porous structure by strong bindings of the CO molecules to the Au atoms resulting in an adsorption layer on the Au surface inhibiting the Au atoms surface diffusion. So, also by post-dealloying thermal processes, the kinetic evolution of the NPG is established by the Au atoms diffusion behaviour.
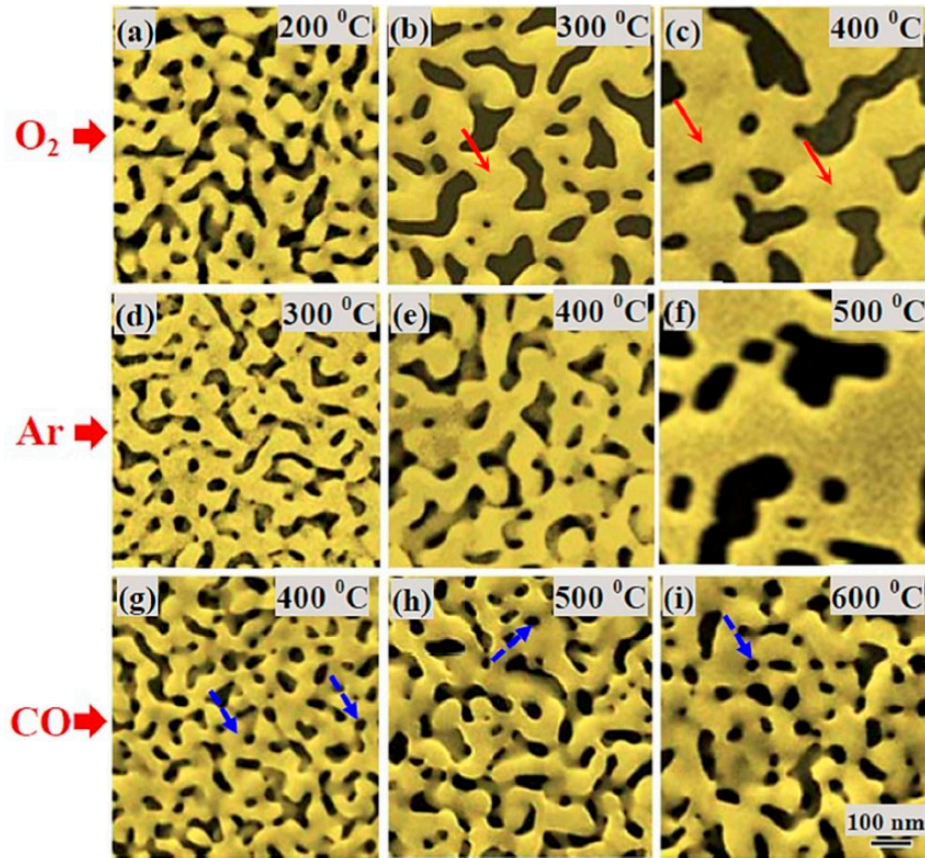
Figure 7. Scanning electron microscopy images of NPG film thermally processed for two hours under different atmospheres: (**a**–**c**) at 200, 300, 400 °C in O_2, (**d**–**f**) at 300, 400, 500 °C in Ar, (**g**–**i**) 400, 500, 600 °C in CO. Reproduced with permission from [33]. Copyright Elsevier, 2015.
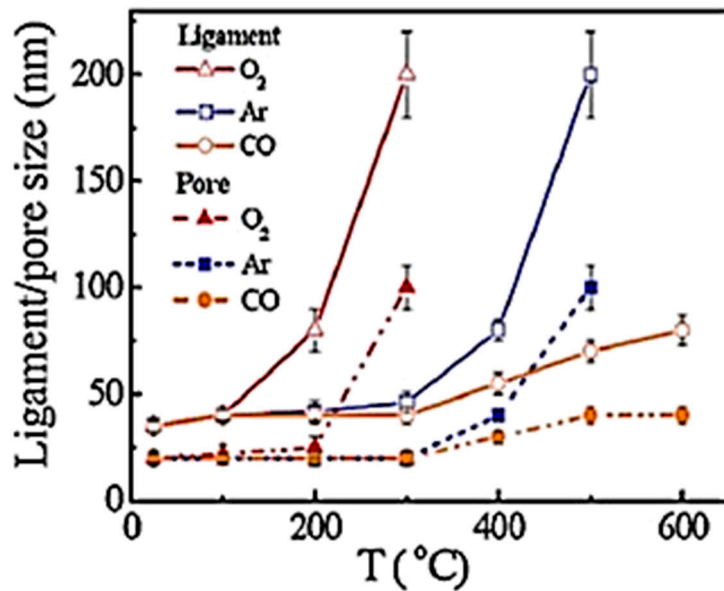

Figure 8. Evolution of the ligaments and pores sizes of the NPG films versus annealing temperature under the different annealing atmospheres. Reproduced with permission from [33]. Copyright Elsevier, 2015.

The effect of the annealing temperature and atmosphere is, also, evident on the porosity (area fraction of pores), as reported in Figure 9: the porosity (i.e., area fractions of the pores) is constant for the NPG films annealed in air below 200 °C and in Ar below 400 °C. However, in these conditions,

the sizes of the ligaments and pores increase: this overall behavior is due, then, to the curvature-driven diffusion of surface atoms. The increase of the annealing temperature T results in the increase of the area fraction of the pores both for the NPG films annealed in air and Ar due to the Au ligaments densification (which can be mediated by surface migration and inter-diffusion). In contrast to this behavior, the porosity of the NPG films annealed in CO gas decreases by increasing T: this is the signature of the incomplete curvature-driven coarsening of the pores result of the inhibited Au atoms surface diffusion caused by the interaction with the CO adsorbates. The main difference between the three types of annealing atmospheres discussed is the interaction of O_2 or CO with Au atoms on the surface except the Arfor with its inert chemical property. To analyze this aspect the author performed XPS analyses: the resulting data indicate that oxygen chemisorbed on the NPG surface is dissociated after annealing at 200 °C. So, the oxygen-depleted surface is much more reactive than the coordinated Au one, facilitating the growth of clusters or islands. Thereafter, the releasing of chemisorbed oxygen from Au atoms accelerates the coarsening kinetics of NPG above 200 °C through the formation of surface vacancies and then, shrinking and densification occur, as observed for NPG annealed in air: in air, the adsorption of oxygen stabilizes the NPG three-dimensional structure below 200 °C, and then a significant pore growth occurs subsequently at higher temperature induced by the desorption of chemisorbed oxygen. When the NPG film is annealed in CO, however, the data indicate that the CO molecules adsorbed on the Au surface exist in a complex form of O–Au–C≡O resulting in an enhanced σ-bond of CO to Au atom. The impurities of O–Au–CO complex could effectively block surface diffusion of Au atoms. This results in a stabilizing effect of the CO atmosphere on the NPG structure: the reduction of adsorbed O_2 and the strong adsorptionof CO onto the Au surface inhibits the pore/ligament growth.

These data clearly show the possibility to controllably tune the morphological characteristics of the NPG by tuning the parameters of an annealing process (temperature, atmosphere) to be performed after the dealloying process.
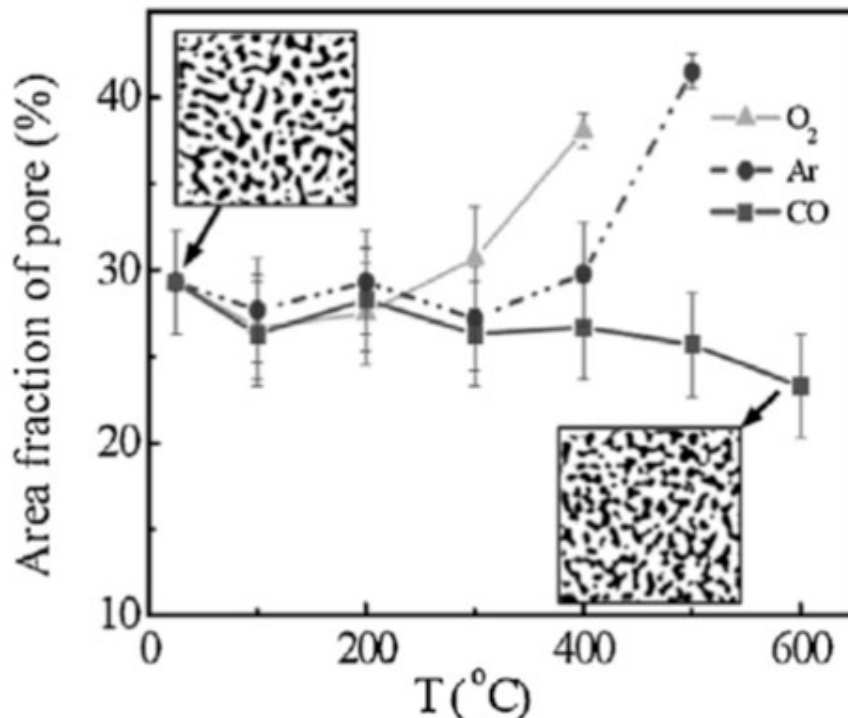

Figure 9. Area fraction of the pores versus the annealing temperature T in the various annealing atmospheres. The insets show the digitalized images of NPG film (**upper left**) and that annealed in CO at 600 °C (**lower right**), from which porosity was estimated. Reproduced with permission from [33]. Copyright Elsevier, 2015.

We conclude this section mentioning that, obviously, pores size and population are related to the corrosion and mechanical properties of the alloy used for the dealloying process and then to the corrosion and mechanical properties of the NPG. First of all, we observe that Parida et al. [107] reported, for the dealloying of AuAg bulk systems, that the formation of NPG is accompanied by ~30% volume shrinkage. Since the original crystal lattice is maintained during the process, they suggest that the formation of NPG is accompanied by the creation of a large number of lattice defects and by local plastic deformation. Such a volume shrinkage is consistent with a very large density of defects (lattice dislocations, stacking faults, twins) generated by the dealloying process in the Au crystal structure, but also, a considerable Au crystal plastic deformation needs to be taken into in account to justify the entity of the shrinkage. Regarding the microstructural evolution of NPG during the dealloying process, Dotzler et al. [40] monitored the strain development and porosity evolution in NPG foil during the dealloying process of the AuAg alloy foil by combining synchroton small angle X-ray scattering and X-ray diffraction. In particular, they followed the time dependence of the dealloying as a function of the acid concentration. Firstly, they observed a fast initial dissolution stage with an increase in surface area due to pore and mound formation; this leads to strain in the NPG that results from an increase in capillary pressure. After dissolution is complete, there is rapid coarsening of the pore–ligament morphology. During this later stage, strong strain anisotropies occur that can be explained by preferred crystallographic orientation of ligaments. Hence, there is a strong correlation between the morphology evolution, i.e., pores sizes and population, and strain development. However, Biener et al. [41] reported, also, on the fracture behaviour of NPG finding that, despite its macroscopic brittleness, NPG is microscopically a very ductile material as ligaments strained by as much as 200% can be observed in the vicinity of crack tips. They investigated the mechanical properties of NPG under compressive stress by depth-sensing nanoindentation and determined a yield strength of ~145 MPa and a Young's modulus of ~11.1 GPa. More specifically, Mathur and Erlebacher [42] determined the Young's modulus of NPG with controlled porosity variation between 3 and 40 nm by mechanical testing of 100 nm thick, free standing, large-grained, stress-free films of NPG: the results indicated a dramatic rise in the effective Young's modulus (from about 5 GPa to abou 40 GPa) of NPG with decreasing ligament size (from about 40 nm to about 3 nm).

3. Nanoporous Gold-Based Sensing Applications

3.1. Optical Sensing

The exceptional optical properties of NPG find promising applications in optical sensors [20–26,47–73,93–102]. When the dimensions of metals such as Au are reduced to the scale of the mean free path of electrons within the material, the oscillations of electrons generate localized surface plasmon resonance (LSPR) [14,15]. These electron waves may interact with their surroundings, which can be used to enhance spectroscopic characterization techniques, such as surface enhanced Raman spectroscopy (SERS). This technique is based on the inelastic scattering of electromagnetic radiation by molecules absorbed on the surface of NPG and depends on the characteristics of the surface as pores size. In particular, the smaller the pores sizes, the stronger the amplification factor of the electromagnetic field resulting in large increases the sensitivity of detection techniques based on the SERS effect. In addition, NPG is a promising substrate for scattering analysis due to its chemical inactivity and thermal stability. Generally, NPG acts as a high surface area template to adsorb molecules as well as enzymes or biomolecules. The nanopore size enhances, also, molecular fluorescence.

In this section we describe and discuss some applications of the optical properties of NPG for optical detection of adsorbates.

Kucheyev et al. [53] reported on the use of NPG leafs as active, stable, biocompatible, reusable, and low-cost SERS substrate. They produced NPG samples by dealloying $Ag_{0.7}Au_{0.3}$ alloy leafs in 70% HNO_3 for 48 h at room temperature. The resulting NPG is shown by scanning electron microscopy image, in Figure 10a, characterized by pores with a mean size of ~25 nm.
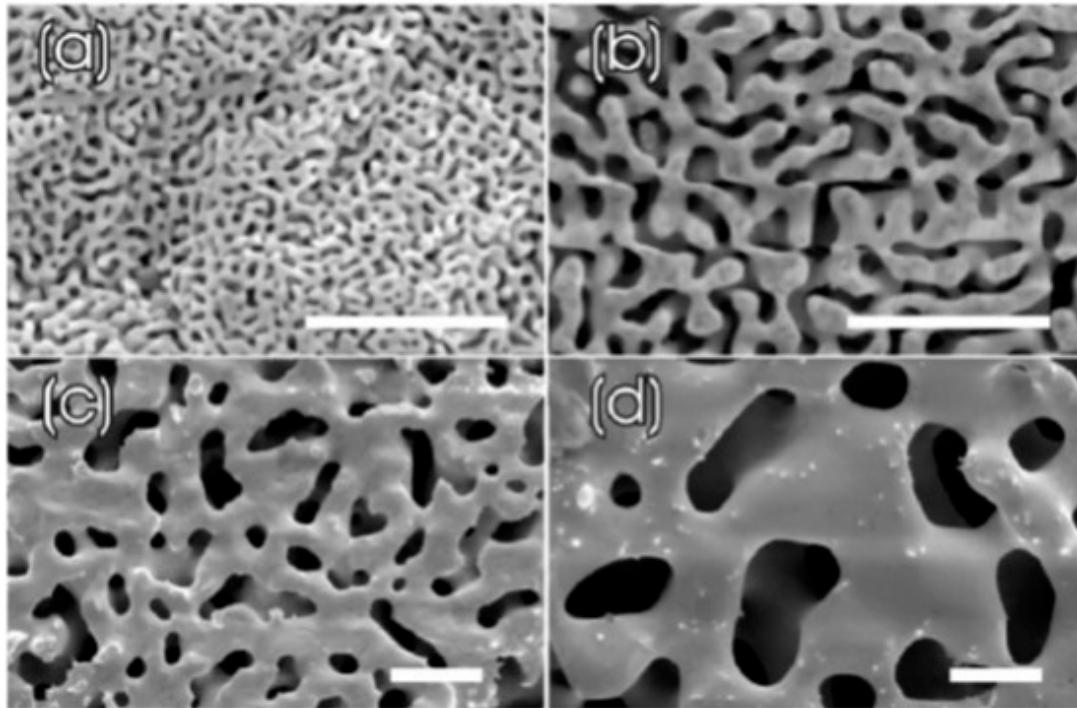
Figure 10. Representative scanning electron microscopy of the surface of NPG: (**a**) as obtained by the dealloying process, (**b**) after dealloying and annealing at 300 °C for 120 min, (**c**) after dealloying and annealing at 450 °C for 120 min, (**d**) after dealloying and annealing at 550 °C for 120 min. Scale bars: 1 µm. Reproduced with permission from [53]. Copyright American Physical Society, 2006.

In addition, the authors perfomed annealing processes (in Ar atmosphere, in the 100–600 °C temperature range, for two hours) on the as-dealloyed NPG to controllably tune the ligaments and pores size (Figure 10b–d show typical scanning electron microscopy images of the NPG after some annealing processes). Overall, Figure 11 reports the experimental derived mean pores size versus the annealing temperature showing that the mean pores size can be increased from about 25 nm to about 600 nm. Concerning the SERS measurements, the authors adsorbed crystal violet molecules on the NPG surface and acquired SERS spectra for the various NPG samples investigating the effect of the pores size. Examples of the experimental SERS spectra, at some annealing temperatures for the used NPG, are shown in Figure 12: these spectra clearly indicate that the SERS enhancement strongly depends on the annealing temperature and, therefore, on the mean size of the pores and/or ligaments, and the highest enhancement is obntained for the pores with mean size of ~250 nm (NPG annealed at 500 °C). In particular, samples annealed at temperatures around 500 °C exhibit the highest SERS signal. The SERS enhancement arises from the enhancement mechanism correspondent to the efficient excitation and trapping of surface plasmons coupled with the strong field localization in the NPG pore regions.

However, in this study of Kucheyev et al. [53] the highest SERS enhancement is not obtained in correspondence of the smaller pores size and it is unexpected. Genenerally, experimental and theoretical results concerning systems of electromagnetically coupled nanoparticles, the SERS enhancement factor should increase by decreasing the mean nanoparticles distance [108]. However, even if one can expect, then, that decreasing the pores size, the SERS enhancement should increase, additional factors could play a key role in determining the best condition for light-plasmon coupling as the dielectric filling the pores such as size and shape, and geometrical arrangement of pores.

So, this specific aspect was widely studied in several papers.

As a first example, Chen et al. [54] studied the pore-size tuning and optical properties of NPG films. They fabricated 100 nm-thick NPG films using pulse electrochemical dealloying and chemical dealloying with averge pore size ranging from 4 nm to 140 nm by controlling the dissolution rate of Ag atoms and surface diffusion rate of Au atoms along the alloy-solution interfaces. In particular,

Figure 13 reports, according to the authors, the plot (both in linear scales (a) and in Log-Log scale (b)) of the evolution of the mean pores size versus the etching time for samples produced by various dealloying approaches (electrochemical dealloying, PED, low-temperature chemical dealloying, LT-CD, room-temperature chemical dealloying, RT-CD, low-concentration of electrolyte chemical dealloying, LC-CD, surface-assisted chemical dealloying, SA-CD).
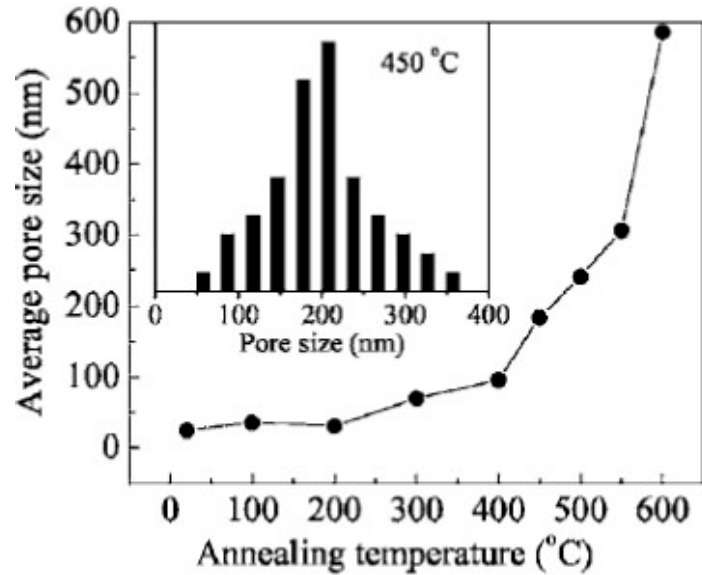

Figure 11. Evolution of the mean pores size in NPG annealed for two hours from 100 °C to 600 °C in Ar. The inset reports the distribution of the pores sizes after annealing at 450 °C. Reproduced with permission from [53]. Copyright American Physical Society, 2006.
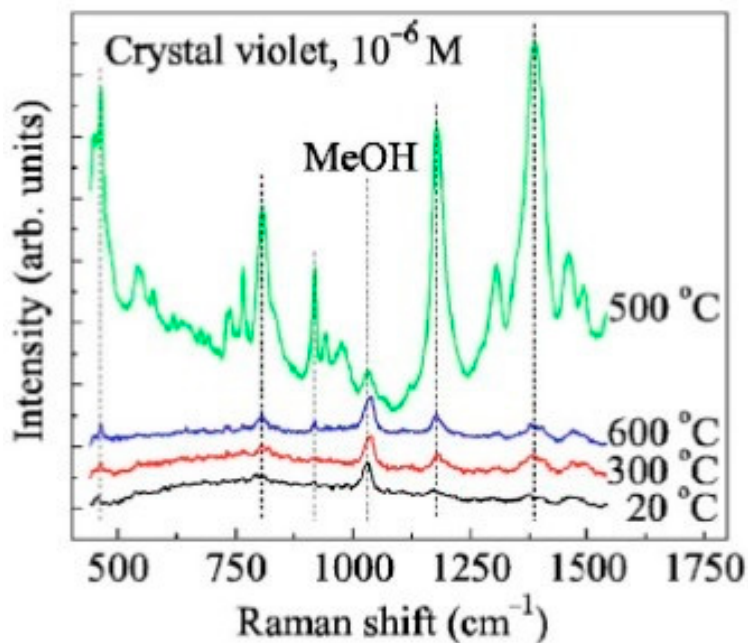
Figure 12. SERS spectra of NPG obtained by dealloying and subsequent annealing processes (at the temperatures indicated within the figure) and after immersion in a 10^{-6} M solution of crystal violet. Spectra are offset for clarity. A methanol-related peak is labeled MeOH. Reproduced with permission from [53]. Copyright American Physical Society, 2006.

The following aspects can be inferred from Figure 13: (i) the pore size increases with etching time and attains a saturation level of 45 nm for RT-CD, 40 nm for LT-CD, 8 nm for PED, and 140 nm for SA-CD. Therefore, the distribution of pore size prepared by CD methods is from 7 to 140 nm, including the LT-CD (7–40 nm), LC-CD (9–40 nm), and SA-CD (12–140 nm), while that is 4–8 nm for PED. These measures are, however, self-consistent since the authors, in addition measured, also, the NPG films surface roughness by quantifiying the RMS (Root-Mean-Square) using atomic force microscopy imaging. So, the RMS resulted lower than 10 nm for the PED, LT-CD, RT-CD, LC-CD samples, and about 20 nm for the SA-CD sample. Therefore, the pores size as evaluated by the paln-view scanning electron microscopy images furnish, for each sample, values much higher than the NPG surface roughness, also for the SA-CD sample for which the pores size plot in Figure 13a could seem strange; (ii) The coarsening of pore exhibits a time-dependent change. Putting the variation of pore size, d, against etching time, t, in a double-log diagram, the fittings roughly follow a power law relationship: $d^\alpha = rt$ (with α the coarsening exponent and r the coarsening rate). The fitting equations and linear coefficient, R^2, are given in Figure 13b and indicating, in particular, $\alpha \approx$ 3, 2.3, 2.2, 1.8, and 1.0 for the RT-CD, LT-CD, PED, LC-CD, and SA-CD samples, respectively (and suggesting that the formation of pores in these cases is not simply a material removal process).
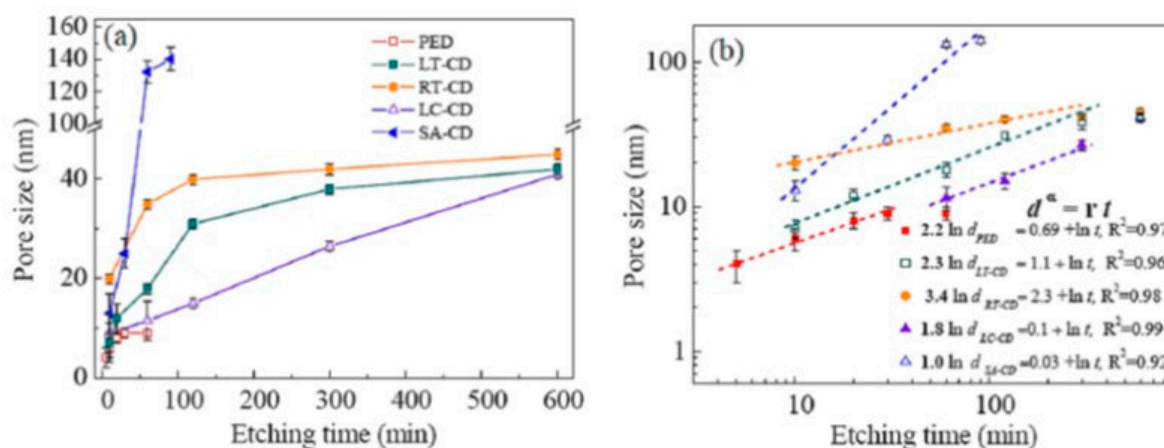

Figure 13. Evolution of the mean pores size versus the etching time for samples produced by various dealloying approaches (electrochemical dealloying, PED, low-temperature chemical dealloying, LT-CD, room-temperature chemical dealloying, RT-CD, low-concentration of electrolyte chemical dealloying, LC-CD, surface-assisted chemical dealloying, SA-CD), in (**a**) in a linera scale and in (**b**) in a Log-Log scale. Reproduced with permission from [54]. Copyright Elsevier, 2015.

Correspondently, Figure 14 reports, for some selected samples (i.e., for some selected pores size) UV-vis absorption spectra (Figure 14a) and SERS spectra (Figure 14b) of NPG films, prepared by various dealloying approaches, with different average pores size indicated by the number in the caption within the figures (so, for example, NPG-8 means the NPG film with average pores size of 8 nm). The UV-vis absorption spectra corresponding to NPG films with pore sizes of 7, 12, and 18 nm produced by LT-CD present a single, low-value absorbance band. On the contrary, NPG films produced by RT-CD and with mean pores size of 20, 35, 40 nm and produced by SA-CD and with mean pores size of 140 nm present in the UV-vis absorption spectra two intrinsic peaks at ~480 and ~525 nm. The absorbance peak centered at 525 nm (marked by the solid arrow) red shifts when the average pores size increases while the peak at 480 nm does not shift. In addition, regarding the NPG films with average pores size from 7 to 140 nm fabricated by CD, the corresponding absorption value increases when the pore size increases. However, the NPG-8 film fabricated by PED does not follow this behavior and this fact is attributed to the superfine pore size and the lowest residual Ag content. The SERS spectra were acquired by using crystal violet as probe molecules: the NPG films were immersed in 10^{-5} M crystal violet solution for 6h so to adsorbate these molecules on the NPG surface. The SERS spectra in Figure 14b clearly indicate the enhancement of the SERS signal by reducing the average pores size from 140 nm to 7 nm with the exception of the sample with pores size of 8 nm

presenting the highest enhancement. However, this result is due to the combination of stronger field localization by reducing the pores size, larger residual Ag, and higher NPG surface roughness. In fact, the NPG-8 film shows the strongest SERS enhancement corresponding to the conditions of the lowest Ag content and the smallest surface roughness. In addition, the authors conclude, from the comparison between NPG-8 produced by PED and NPG-7 fabricated by LT-CD, that a more homogeneous pore results in a much higher adsorption of organic molecules on the surface of NPG.
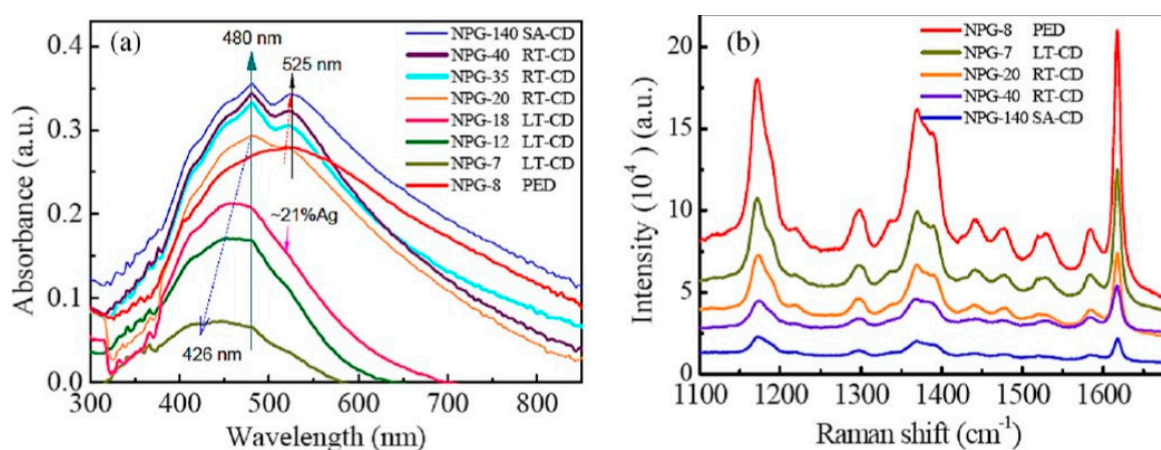
Figure 14. UV-vis absorption spectra (**a**) and SERS spectra (**b**) of NPG films, prepared by various dealloying approaches, with different average pores size indicated by the number in the caption within the figures (so, for example, NPG-8 means the NPG film with average pores size of 8 nm). The SERS spectra are acquired by using crystal violet molecules adsorbed on the NPG surface as probe molecules. Reproduced with permission from [54]. Copyright Elsevier, 2015.

Then, Lang et al. [55] performed a combined experimental and theoretical investigation on the SERS properties of NPG at temperatures ranging from 80 to 300 K using rhodamine 6G (R6G) as probe molecules. Their results show that the SERS intensity increases as pores size and temperature of the sample during the measure decrease. In particular, starting from the experimental results, the theoretical analysis performed on the basis of a discrete dipole approximation approach suggest that the improved SERS enhancements by decreasing temperature and pores size arise from the combined effects of the electron-phonon scattering, finite ligament size effect, and the electromagnetic coupling between neighboring Au ligaments. In particular, the authors fabricated 100 nm-thick NPG films by dealloying $Ag_{75}Au_{25}$ (at.%) alloy leafs in a concentrated HNO_3 solution at the different temperatures 293, 273, and 253 K and different dealloying times so to controllably change the mean size D of the pores. Then R6G molecules were physisorbed on the NPG surface (by immersing the samples in 10^{-7} mol/L R6G solution) and the SERS spectra were acquired to analyze their dependence on the pores size and temperature of the sample during the measure. So, Figure 15a reports the SERS spectra acquired by decreasing the pores size D from 41 nm to 12 nm: it is clear that the SERS enhancement increases by decreasing D, whereas the high intensity peaks in the spectra correspond to the vibrational modes of th R6G molecule. To quantitatively analyze this effect, the authors considered the relative integrated intensity of the R6G Raman peak located at 1650 cm^{-1} as $m_{SERS} = I_{SERS}(T_0, D)/I_{SERS}(T_0)$ (with $I_{SERS}(T_0, D)$ the Raman intensity corresponding to the sample with pores size D and at temperature T_0 during the spectrum acquisition, and with $I_{SERS}(T_0)$ the SERS intensity af the sample with D = 50 nm which is chosen as sample reference since 50 nm is, about, the electrons mean free path in bulk Au). The factor m_{SERS} is plotted versus D in Figure 15b and showing a rapid increase by decreasing D (in the plot, the rhombohedral dots correspond to the data acquired with the amples at 293 K, the circular dots to the data acquiredwith the samples at 273 K, and the triangular dots to the data acquired with the samples at 253 K). For example, we can observe that the SERS intensity of NPG films with D = 12 nm is about 20 times higher than that of the NPG film with D = 50 nm. Obviously, this continuous increase of the SERS enhancements with the decreasing pore size is

contrary to the maximum SERS enhancement at a pore size of 250 nm observed by Kucheyev et al. [53] (Figure 12), confirming that the anomalous enhancement from very large pores arises from additional effects, possibly from the rough surfaces of Au ligaments, which causes an antenna-like effect leading to the SERS enhancement. Therefore, as a general rule, smaller the pores size larger, from one hand, the exposed surface area from NPG for the adsorption of target molecules (enhancing the Raman signal) and, from the other hand, greater the SERS enhancement due to the electromagnetic field enhancement caused by plasmon excitation of NPG through incident laser light. The authors analyzed, also, the SERS enhancement effect versus the temperature T_0 of the samples during the SERS spectra acquisition.
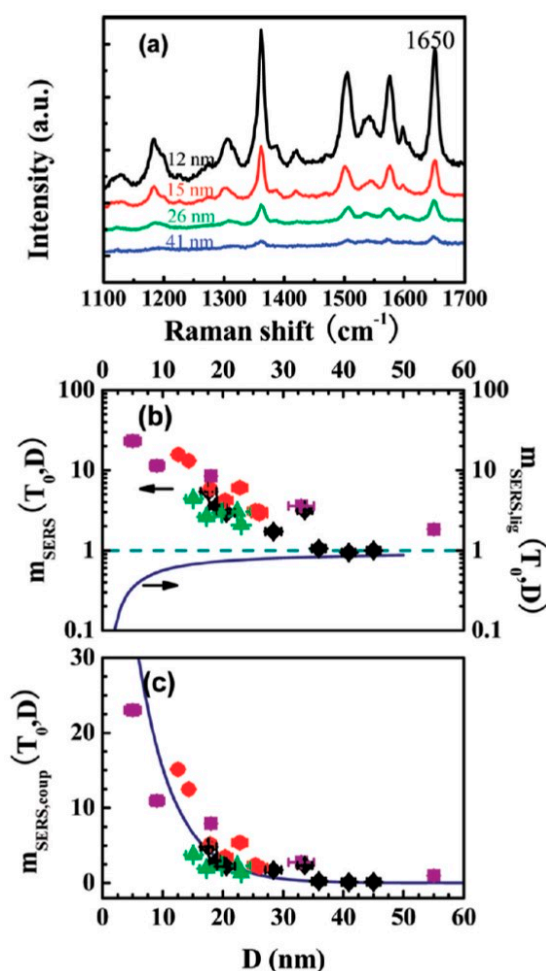
Figure 15. (**a**) Representative SERS spectra of NPG films with different pores size D, after R6G molecules physisorbtion on the surface. (**b**) Plot the relative integrated intensity of the R6G Raman peak located at 1650 cm^{-1} as $m_{SERS} = I_{SERS}(T_0, D)/I_{SERS}(T_0)$ versus the pores size D (with $I_{SERS}(T_0, D)$ the Raman intensity corresponding to the sample with pores size D and at temperature T_0 during the spectrum acquisition, and with $I_{SERS}(T_0)$ the SERS intensity af the sample with D = 50 nm which is chosen as sample reference since 50 nm is about the electrons mean free path in bulk Au). The rhombohedral dots correspond to the data acquired with the amples at 293 K, the circular dots to the data acquiredwith the samples at 273 K, and the triangular dots to the data acquired with the samples at 253 K. In addition, the function $m_{SERS,\ lig}$ is plotted versus the samples temperature, being $m_{SERS,\ lig} = I_{SERS,\ lig}(T_0, D)/I_{SERS}(T_0)$ with $I_{SERS,\ lig}$ the contribution to the SERS intensity from the individual Au ligament. (**c**) Plot of the experimental data (dots) corresponding to the relative SERS intensity $m_{SERS,\ coup} = I_{SERS,\ coup}(T_0, D)/I_{SERS}(T_0)$ with $I_{SERS,\ coup}$ the SERS intensity arising from the electromagnetic coupling between neighboring Au ligaments. The full line represents the exponential function $m_{SERS,coup}(T_0,D) = A\exp(-D/l)$ with A = 81 and l = 6 nm. Reproduced with permission from [55]. Copyright American Chemical Society, 2009.

So, Figure 16 reports, as examples, SERS spectra for the NPG films with pores size of 15 nm (a), 26 nm (b), 41 nm(c) acquired changing the sample temperature from 80 K to 300 K, and showing that the SERS enhancement increases by decreasing the temperature, as summarized in Figure 16d where the intensity of the Raman peak at 1650 cm^{-1} is plotted, for the three samples, versus the sample temperature.
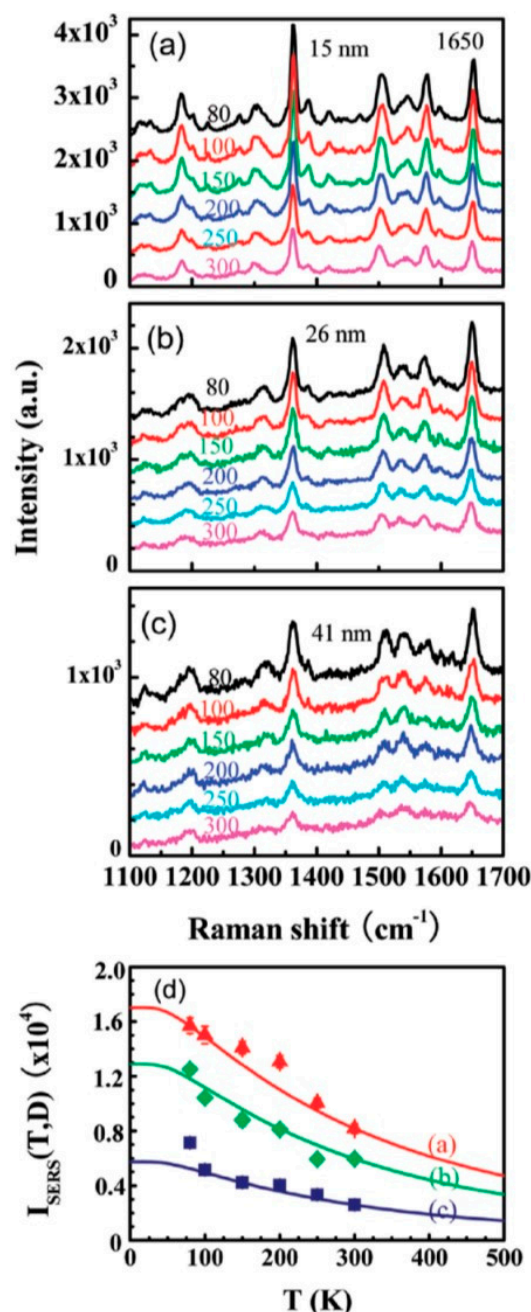

Figure 16. SERS spectra of NPG films with pores size of (**a**) 15 nm, (**b**) 26 nm, and (**c**) 41 after R6G molecules physisorbtion on the surface, and acquired with the samples at 80, 100, 150, 200, 250, and 300 K. (**d**) Integrated SERS intensity of the paek at 1650 cm^{-1} for the three samples versus the sample Table 15. nm-sample, green: 26 nm-sample, blue: 41 nm-sample). Reproduced with permission from [55]. Copyright American Chemical Society, 2009.

The authors were able to develop a model based on the electromagnetic field enhancement caused by plasmonic excitation of NPG through the incident laser light to explain the observed experimental dependences of the SERS signal on the pores size D and temperature T. The model

predicts that the pore size and temperature-dependence of the SERS intensity $I_{SERS}(T,D)$, under an electromagnetic field resonance frequency, is as

$$I_{SERS}(T,D) \propto 1/[\omega_c(T,D)]^4 \qquad (3)$$

where $\omega_c(T,D)$ is the collision frequency of electrons depending on T and D. This collision frequency is formed by two components, $\omega_c(T,D) = \omega_c(T) + \omega_c(D)$, the first depending only on temperature T, arises from the phonon-electron scattering, the second depending only on the pores size D, arises from the electron mean free path. So, the relation $[I_{SERS}(T,D)]/[I_{SERS}(T_0,D)] = [\omega_c(T_0,D)/\omega_c(T_0,D)/]^4$ follows which can be regarde as the temperature dependence of the relative SERS intensity for each fixed pores size D: the predictions of this relation, for each fixed D, are plotted as the full lines in Figure 16d obtaining an excellent agreement with the experimental data. Then, the authors conclude that the increases of $I_{SERS}(T,D)$ by decreasing T is due to the reduced effect of electron-phonon scattering. At low temperatures (<30 K) the SERS intensity saturates to a constant value and this constant value increases by decreasing D similarly to the inverse of temperature dependence of the electronic resistivity in nanostructured Au: this is the signature of the underlying correlation between the SERS effect and the characteristics of the electron transport, i.e., the electron mean free path, in nanostructured Au. On the basis of this model, the full line in Figure 15b reports, also, the calculated $m_{SERS, lig}$ as $m_{SERS, lig} = I_{SERS, lig}(T_0, D)/I_{SERS}(T_0) = I_{SERS, lig}(T_0, D)/I_{SERS}(T_0) = [\omega_c(T_0)/\omega_c(T_0,D)/]^4$: according to the result, the decrease of the Au ligament size determines the weakening of SERS enhancements due to the dramatic increase of electronic scattering at the inner surface and this is in contrast with the experimental observation in Figure 15.

Therefore, in addition to the finite size effect of an individual ligament, there should be other factors responsible for the large SERS enhancements of NPG with a small nanopore size: this is identified by the authors in the electromagnetic coupling between neighboring ligaments and enhanced localized surface plasmon resonances. They, in fact, performed near-field calculations with the method of the discrete dipole approximation (DDA), whose results are reported in Figure 17. To simplify the similations, the authors pictured the NPG as a two-dimensional structure with identical pores and ligament having the same size D (Figure 17a). Then, using the DDA approach they calculated the near-field distributions on the top surfaces (Figure 17b–j) considering D = 10, 50, 80 nm, and an electromagnetic plane wave with wavelength of 514 nm impinging along the direction normal to the top surface. Figure 17h–j reports the electromagnetic field enhancements due to the electromagnetic coupling between neighboring ligaments, E_{coup}, with $E_{coup} = E–E^*$ where E is the total field distributions of NPG (Figure 17b–d), calculated for the geometry of the nanostructure reported in Figure 17a with materials A and B being Au, and E^* is the localized electric field distribution without the electromagnetic coupling effect (Figure 17e–g), which is the sum of electric field distributions of the regions in Figure 17a corresponding to material A (Au) and material B (Au) of the nanostructure. These results on E_{coup} show the large enhancements of the electromagnetic field of NPG with decreasing D as arising from both the localized electromagnetic increments and the electromagnetic coupling between the spatially opposite ligaments, in particular in NPG with the 10 nm pore. The experimentally measured SERS intensity of NPG films as reportd in Figure 16c are consistent with the size effect of individual Au ligaments and the electromagnetic coupling between neighboring ligaments. In particular, in fact, Figure 16c reports, as dots, the experimental relative SERS intensity $m_{SERS, coup} = I_{SERS, coup}(T_0, D)/I_{SERS}(T_0)$ with $I_{SERS, coup}$ the SERS intensity arising from the electromagnetic coupling between neighboring Au ligaments: these data, as a function of D (which in the simulations is, also, the Au ligament size) rapidly increase by decreasing D by an exponential function, which can be well-fitted by the scaling behavior of distance decay of plasmon coupling between metal ligaments (corresponding to the effect of the evanescent field), $m_{SERS,coup}(T_0,D) = A\exp(-D/l)$, where A is a constant and l denotes the decay length, which is the fitting full line in Figure 16c resulting, in particular, in l = 6 nm. Therefore, this agreement suggests, clearly, that the electromagnetic coupling between neighboring Au ligaments gives rise to a high number of "hot spots" in the NPG nstructure when nanopore sizes become small and thus resulting in the SERS spectra with high enhancement from the whole samples.
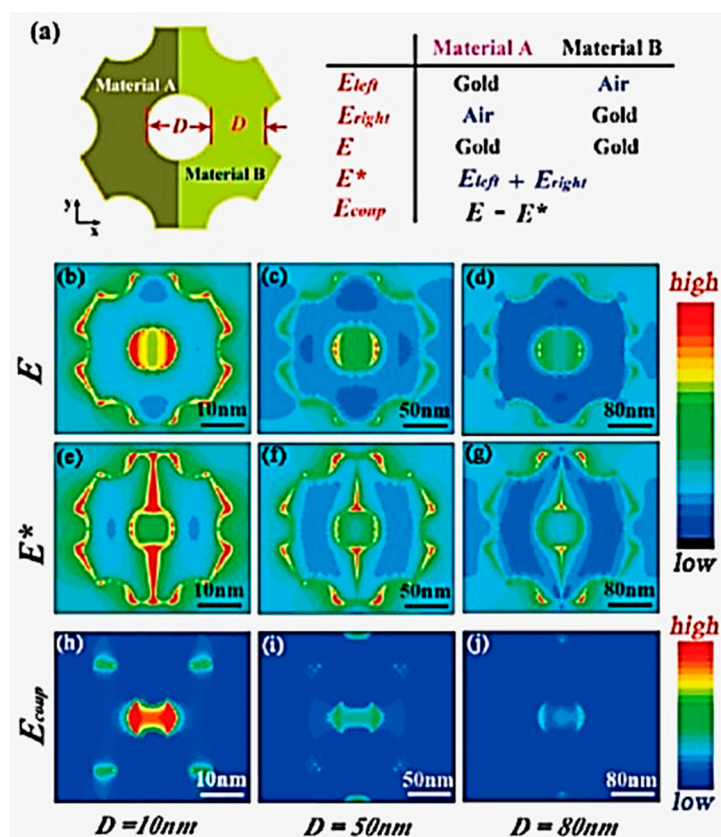
Figure 17. (**a**) Representation of the nanostructure geometry emplyed for discrete dipole approximation-based (DDA) simulations. Calculated total electric field (E) (**b–d**), localized electric field (E*) (**e–g**), and electromagnetic coupling electric field (E$_{coup}$) distributions (**h–j**) on the top surface of the NPG with D = 10, 50, and 80 nm, respectively. Reproduced with permission from [55]. Copyright American Chemical Society, 2009.

In addition, Lang et al. further employed the use of NPG films for sensing based on molecular fluorescence enhancement [56]. They developed a method to tailor the NPG porosity by a combination of dealloying and electroless Au plating and verified that the combined effect of improved quantum yield and excitation of fluorophores determines a significant fluorescence enhancement from molecues (cyanine-3, Cy3, or rhodamine-6G, R6G) adsorbed on the NPG surface. This result was interpreted as caused by the near-field enhancement of NPG, due to the strong electromagnetic coupling between neighboring ligaments, and to the weakening of plasmon damping of the large ligaments because of the small pore size and large ligament size. In this case, the authors fabricated NPG by dealloying (in 70% HNO$_3$ solution) free-standing Ag$_{65}$Au$_{35}$ (atomic ratio) films for 5 min, or 10 min, or 15 min, or 30 min, obtaining, respectively, NPG with pores size D and Au ligaments width d corresponding to D = 10 nm and d = 10 nm, D = 15 nm and d = 15 nm, D = 20 nm and d = 20 nm, D = 30 nm and d = 30 nm. In addition, some NPG samples were plated by Au so to deposit additional Au on the pre-existing Au ligaments and, consequently, so to vary the Au ligaments width and pores size. Therefore, additional NPG films were obtained characterized by D = 10 nm and d = 30 nm, D = 12 nm and d = 28 nm, D = 15 nm and d = 25 nm corresponding to diffrent plating times. The NPG films deposited on glass slides and then immersed into a human serum albumin (HSA) aqueous solution so that the HSA can act, then, as binding elements between NPG and Cy3 or R6G molecules. To this end, then, the NPG/HSA samples were immersed in the Cy3 (0.9 mM) or R6G (0.01 mM) aqueous solutions to induce the molecules adsorption. Finally, the authors acquired the fluorescence emission spectra of Cy3 or R6G/HSA/NPG systems, and some examples, for th case of Cy3, are reported in Figure 18a for Au-plated NPG films (GP-NPG) and in Figure 18b for as-dealloyed NPG films (AD-NPG). In particular, spectra are reported for samples with different

couples of pores size D and Au ligaments width d. In addition, these measurements are compared to the emission spectrum of Cy3 or R6G molecules attached directly on the glass substrate, see the inset (plots in the first line, right) in Figure 18.
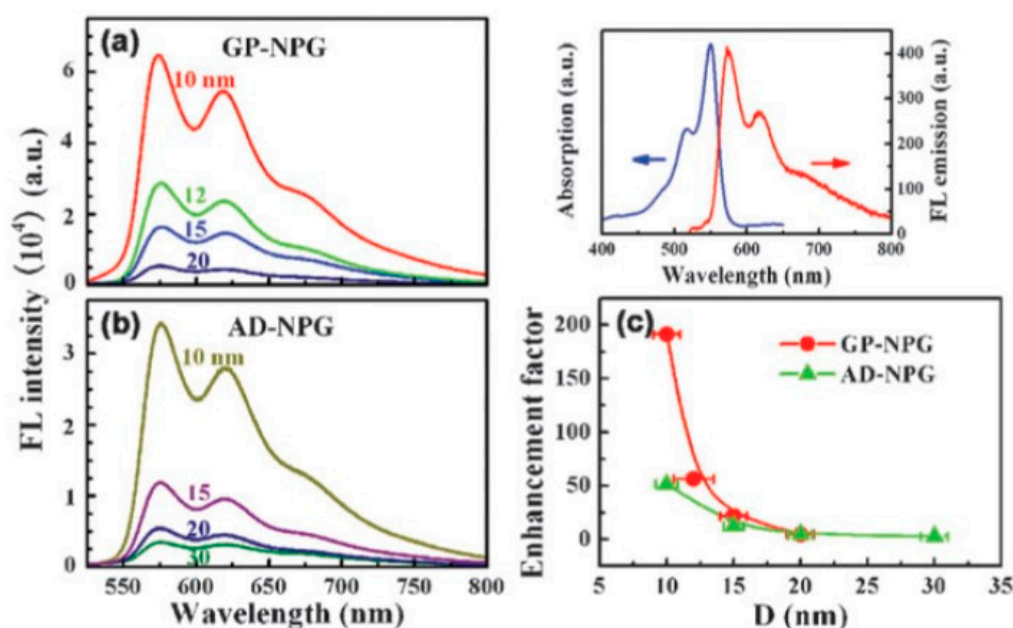

Figure 18. (**a**) Fluorescence emission spectra of Cy3 on human serum albumin (HSA) covered Au-plated (GP-NPG) films with D = 10 nm and d = 30 nm (red line), D = 12 nm and d = 28 nm (red line), D = 15 nm and d = 25 nm (light blue line), D = 20 nm and d = 20 nm (dark blue line). (**b**) Fluorescence emission spectra of Cy3 on HSA covered as-dealloyed NPG (AD-NPG) films with D = 10 nm and d=10 nm (brown line), D = 15 nm and d = 15 nm (violet line), D = 20 nm and d = 20 nm (dark blue line), D = 30 nm and d = 30 nm (green line). (**c**) Coverage corrected enhancement factor of fluorescence emission from Cy3/HSA/GP-NPG and AD-NPG films versus the pores size D. Inset: absorption and fluorescence emission spectra of Cy3 on a reference glass substrate. Reproduced with permission from [56]. Copyright Royal Society of Chemistry, 2011.

To quantitatively evaluate the fluorescence enhancement of the NPG films, the authors reported, see Figure 18c, the coverage corrected fluorescence enhancement factors for Au-plated and as-dealloyed NPG films versus D and d, calculated as $m_{NPG}(D,d) = I_{NPG}(D,d)/I_0$, being $I_{NPG}(D,d) = I_f(D,d)/N(D,d)$ and $I_0 = I_{f0}/N0$, where $I_f(D,d)$ and I_{f0} represent the fluorescence intensities obtained from an area covered with the fluorophore/HSA on a NPG film and a glass sheet, respectively, $N(D,d)$ and N_0 represent the number of fluorescent molecules in the given beam area. Therefore, Figure 18c indicates that the enhancement factors rapidly increase by decreasing D and this behaviour is more pronounced for the Au-plated NPG films D due to the nanoporous structure consisting of larger Au ligaments and smaller pores. The overall enhanced fluorescence mechanism is dictated by the enhanced absorption due to the near field enhancement of NPG ($|E_{NPG}(D,d)|^2$), and the improved radiative decay rate ($\Gamma_{NPG}(D,d)$), which increases the quantum yield ($Q_{NPG}(D,d)$), or $Q_{NPG}(D,d) = \Gamma_{NPG}(D,d)/(k_{nr}+\Gamma_{NPG}(D,d))$], with k_{nr} the intrinsic nonradiative decay rate of fluorophores. So, the fluorescence enhancement factor is modeled as

$$m_{NPG}(D,d) = I_{NPG}(D,d)/I_0 = |E_{NPG}(D,d)|^2 [Q_{NPG}(D,d)/Q_0] \qquad (4)$$

being $Q_0 = \Gamma_0/(k_{nr}+\Gamma_0)$ and Γ_0 the intrinsic radiative decay rates of fluorophores. As a consequence, in view of this modeling, Figure 19 shows in (a) that the local field enhancements of Au-plated NPG films, increases by the factors of about 2.2 to about 64 as D decreases from about 20 nm to about 10 nm and as d increases from about 20 nm to about 30 nm, and these local field enhancements are larger than those obtained for the as-dealloyed NPG films.
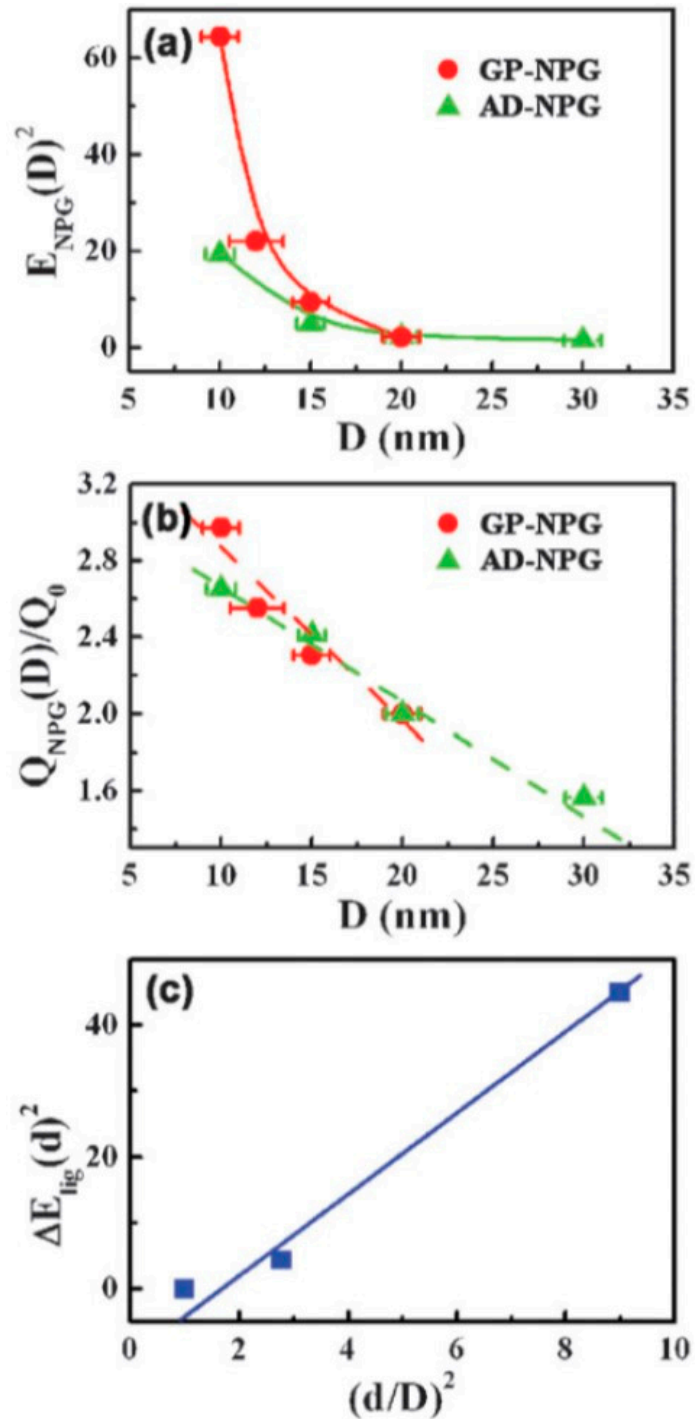
Figure 19. (**a**) Near-field contribution versus pores size D. (**b**) Quantum yield versus pores size D. (**c**) Local field enhancement contributed from larger ligaments versus the ratio $(d/D)^2$. Reproduced with permission from [56]. Copyright Royal Society of Chemistry, 2011.

On the other hand, Figure 19b shows that enhancement of the quantum yield of Cy3 is smaller by decreasing D, so the authors conclude that the enhanced absorption of the fluorescent molecules due to the near-field enhancement of NPG is the main factor in determining the overall improved fluorescence enhancement. Therefore, from one hand, smaller pores originate stronger localized surface plasmom resonances corresponding to larger near-field enhancement, while, from another hand, the accompanied small Au ligaments size limits the further improvement of the local field, and so further enhancement of the fluorescence signal as a consequence of the strong plasmon damping arising from the high electron-surface scattering in very thin ligaments. This is evident for the as-

dealloyed NPG films. In contrast, in the Au-plated NPG films, the pore size can be reduced without reducing the ligaments width, and so the fluorence signal can be further enhanced. This combined effect of the pores size D and ligaments width d is summarized in Figure 19c: it reports the increment of the local field enhancement $(\Delta E_{lig})^2 = (E_{GP\_NPG})^2 - (E_{AD\_NPG})^2$ with $(E_{GP\_NPG})^2$ and $(E_{AD\_NPG})^2$ the local field intensities of the Au-plated and as-dealloyed NPG films, respectively, versus the ratio d/D. This plot indicates a linear relation implying that the increasing $(\Delta E_{lig})^2$ results from the increase of the Au ligaments size. The conclusion should be that the Au surface plasmon polaritons of large ligaments strongly contribute to the electric field enhancement through improving the localized field and near-field coupling between neighboring ligaments. This conclusion is, finally, supported by the results of the discrete dipole approximation calculation reported in Figure 20 and by the experimental UV-Visible extinction spectra reported in Figure 21.
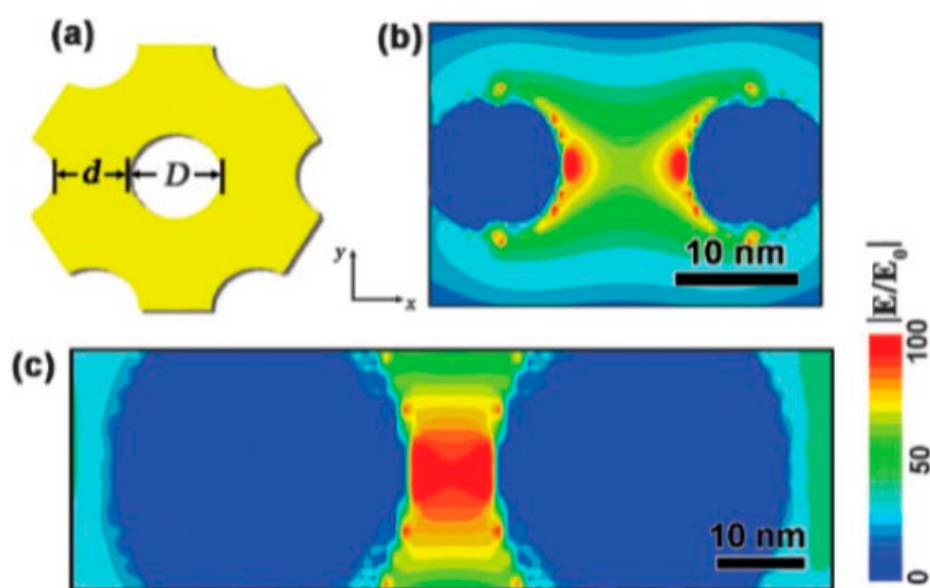

Figure 20. (**a**) Geometry of the nanostructure (pore of size D and ligament of size d) used for the discrete dipole approximation calculation. (**b**) Result of the calculation for the electric field distribution ($|E/E_0|$) in the vicinity of the Au ligament in the case of the as-dealloyed NPG (AD-NPG) sample characterized by D = 10 nm and d = 10 nm. (**c**) Result of the calculation for the electric field distribution ($|E/E_0|$) in the vicinity of the Au ligament in the case of the Au-plated NPG (GP-NPG) sample characterized by D = 10 nm and d = 30 nm. The calculations are performed considering an incident light of 514 nm polarized in the x direction. Reproduced with permission from [56]. Copyright Royal Society of Chemistry, 2011.

The calculation in Figure 20 reports the resulting electric field distributions (E/E_0) (under the plane wave of wavelength 514 nm propagating along the x direction) as produced by a nanostructure (pore of size D and Au ligament of size d) corresponding to D = 10 nm and d = 10 nm (as-dealloyed NPG) and corresponding to D = 10 nm and d = 30 nm (Au-plated NPG) showing that in the case of the Au-plated NPG (i.e., larger Au ligaments) a stronger electric field is obtained as a consequence of the slow plasmon damping resulting from the larger Au ligaments. In addition, the experimental UV-Vis extinction spectra of the HSA-coated Au-plated and as-dealloyed NPG films with different values of D and d (Figure 21a,b) allow to extract a linear increase of the wavelength at which the surface plasmon resonance peak occurs with D both in the case of the Au-plated and as-dealloyed NPG, however with different slopes (Figure 21c): a higher slope is obtained in the case of the Au-plated NPG films confirming that the surface plasmon polaritons of the Au ligaments greatly affect the optical properties of NPG in addition to the local surface plasmon resonances induced by the curvatures of the nanopores.
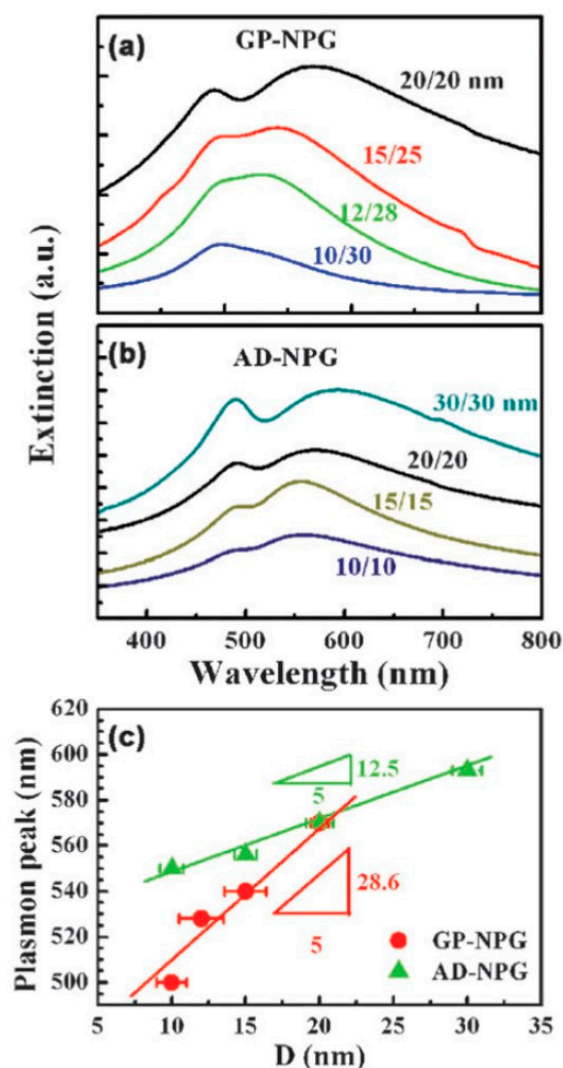
Figure 21. (**a**) UV-Visible extinction spectra of Au-plated NPG films (GP-NPG), coated with a HSA monolayer, and with D = 10 nm and d = 30 nm, D = 12 nm and d = 28 nm, D = 15 nm and d = 25 nm, D = 20 nm and d = 20 nm. (**b**) UV-Visible extinction spectra of as-dealloyed NPG films (AD-NPG), coated with a HSA monolayer, and with D = 10 nm and d = 10 nm, D = 15 nm and d = 15 nm, D = 20 nm and d = 20 nm, D = 30 nm and d = 30 nm. (**c**) Wavelength of the plasmon resonance peaks of HSA/GP-NPG and AD-NPG films versus the pore size D. Reproduced with permission from [56]. Copyright Royal Society of Chemistry, 2011.

To conclude this section, we discuss a specific application developed by Zhang et al. [57], which used NPG films as optical sensor for sub-ppt detection of Hg^{2+}. In particular, the authors prepared NPG by dealloying 100 nm-thick $Ag_{65}Au_{35}$ (at.%) in 69% HNO_3 solution at room temperature. Then, aptamers and oligonucleotide were immobilized on the NPG surface: in order to detect Hg^{2+} and other metal ions, the NPG sample was immersed in PBS buffer solution containing 0.5 M NaCl, 0.1 M $NaClO_4$, Hg^{2+}, and other metal ions for 30 min at room temperature, followed by in situ Raman measurements and the spectra were acquired by changing the concentration, in the solution, of the metal ions. The authors, in addition, to investigate the selectivity of the sensor, added various metal ions in the buffer solution as $Hg(NO_3)_2$, $Cu(NO_3)_2$, $Pb(NO_3)_2$, $Zn(NO_3)_2$, $Ni(NO_3)_2$, KCl, $FeCl_3$, $CoCl_2$, $CaCl_2$, $MgCl_2$, $BaCl_2$, and $Mn(CH_3COO)_2$.

The characteristic length of the pores in the NPg film is ~20 nm (see Figure 22a,b). The aptamer is attached on the Au ligament surface of NPG by the thiol anchor (see Figure 22c). The detection of the Hg^{2+} ions is obtained by monitoring the intensity changes of Cy5 Raman peaks with Hg^{2+} concentrations (see Figure 22d).
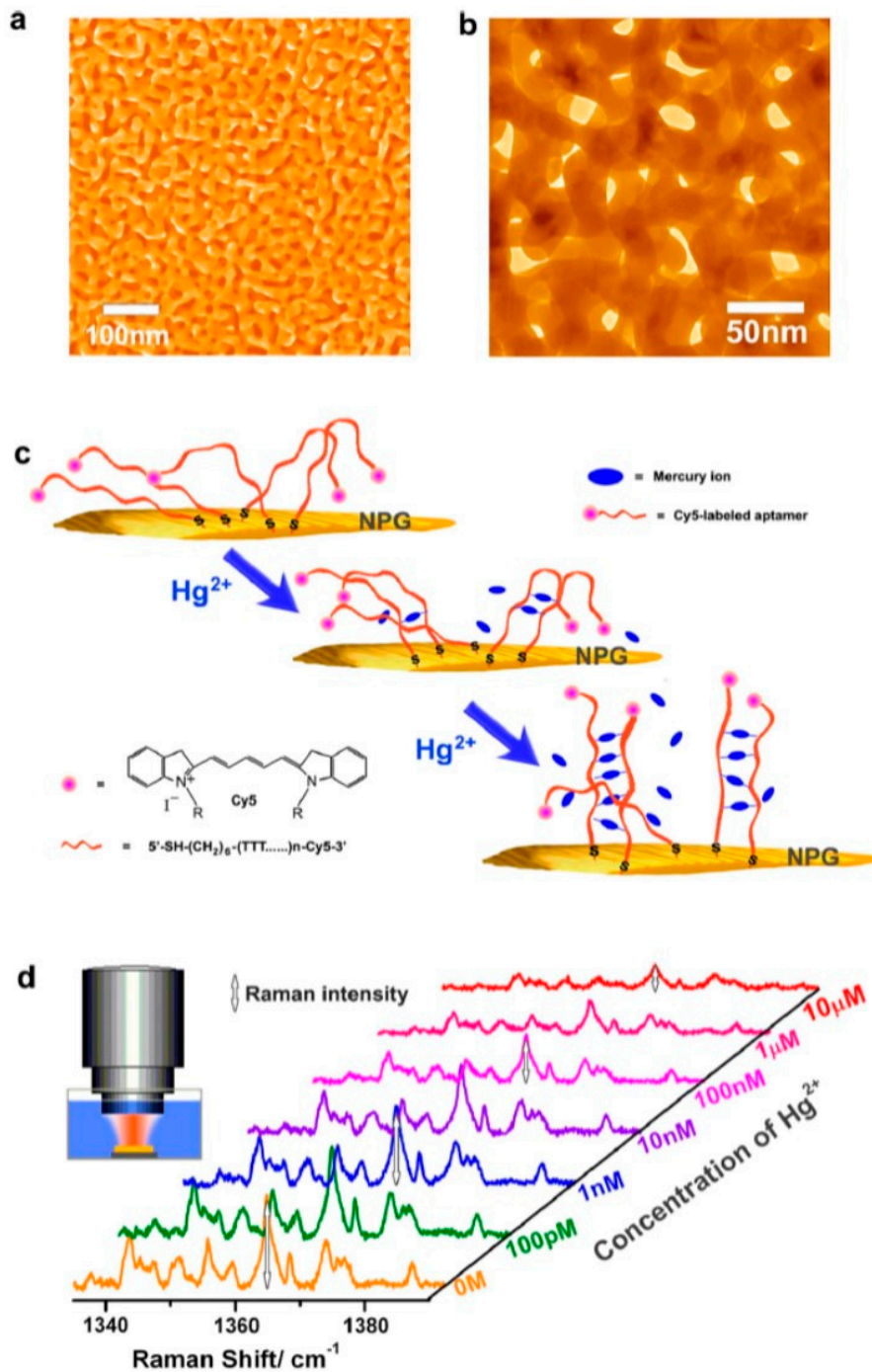
Figure 22. (**a**) Representative scanning electron microscopy image of the NPG film. (**b**) Representative transmission electron microscopy image of the NPG film. (**c**) Schematic representation of the Raman-based sensing of Hg^{2+} using the aptamer modified NPG film. (**d**) Quantitative detection of Hg^{2+} by measuring the Raman signal drop of Cy5 tags using Apt15@NPG sensor. The inset shows the experimental setup for the Hg^{2+} detection. Reproduced with permission from [57]. Copyright American Chemical Society, 2013.

The sensitivity to Hg^{2+} of the NPG/aptamer sensor is based on the changes of the Cy5 Raman intensity determined by the cooperative coordination of a pair of poly-T oligonucleotides with Hg^{2+} ions as shown in Figure 22c. In the absence of Hg^{2+}, the single strand poly-T oligonucleotides display a flexible and random structure. Most Cy5 tags lay on the NPG surface and the Raman signals of Cy5-tags can be maximally enhanced by the local surface plasmon resonance originating from NPG. The

T-Hg^{2+}-T coordination complex may not be the exact antiparallel or parallel duplex. As a result, the Cy5 tags are pulled away from the NPG substrate, resulting in a decrease in the Raman signals of the Cy5 tags.

Therefore, the decrease of the Raman signals from Cy5 tags by increasing the Hg^{2+} concentration results in the ultra-sensitive detection of the Hg^{2+} ions. Figure 22d illustrates Raman spectra taken from the Apt15 functionalized NPG substrate (Apt15@NPG) with different Hg^{2+} concentrations. The strongest Cy5 Raman band at 1365 cm^{-1} was chosen for quantitative analysis based on the intensity dependence of the characteristic Raman peak on Hg^{2+} concentrations, as reported in Figure 23a. In addition, Figure 23b reports the plot of the normalized intensity (normalized to the intensity of the peak with PBS buffer only) of the peak at 1365 cm^{-1} versus the Hg^{2+} concentration. The comparison of the data obtained by using aptamer with 15 T (15 number of thymine bases, Apt15) and 8 T (8 number of thymine bases, Apt8) is reported. It is recognizable that the detection sensitivity of the Apt15@NPG sensor for Hg2þ is better than 1 nM with a dynamic detection range from 1 nM to 10 μM. The sensitivity of Hg^{2+} detection is related to the distance between Cy5-tags and the plasmonic surface of NPG. The more thymine bases are in the oligonucleotide, the more Hg^{2+} ions are required to form a duplex-like structure that hauls up Cy5-tags from the substrate surface for the corresponding Raman signal reduction. Therefore, the short aptamer Apt8 is expected to be more responsive to Hg^{2+}. Furthermore, the authors, to verify the selectivity recognition of Hg^{2+}, replaced Hg^{2+} by other metal ions as Pb^{2+}, K^{+}, Fe^{3+}, Co^{2+}, Mn^{2+}, Ca^{2+}, Ba^{2+}, Ni^{2+}, Cu^{2+}, Zn^{2+}, and Mg^{2+}, finding that the sensor shows appreciable Raman intensity change in the response to Hg^{2+} with respect to the other ions. The sensor selectivity was, also, verified with respect to mixtures of Hg^{2+} and other cations as Pb^{2+}, Ni^{2+}, Fe^{3+}, Co^{2+}, and Mn^{2+} finding that these have no response to the sensor. Finally, it is important to comment on the re-usability of the sensors, as reported in Figure 24. The authors show that the NPG/aptamer optical sensor is readily regenerated in 100 mM ascorbic acid solution for 1 h, followed by washing with a 33 mM PBS buffer (pH 6.9) solution containing 0.5 M NaCl and 0.1 M NaClO$_4$ for 15 min. Figure 24 allows to infer that the sensor practically maintains the initial sensitivity after 10 typical cycles of the regeneration for detecting 1 nM and 1 μM Hg^{2+} in aqueous solutions.
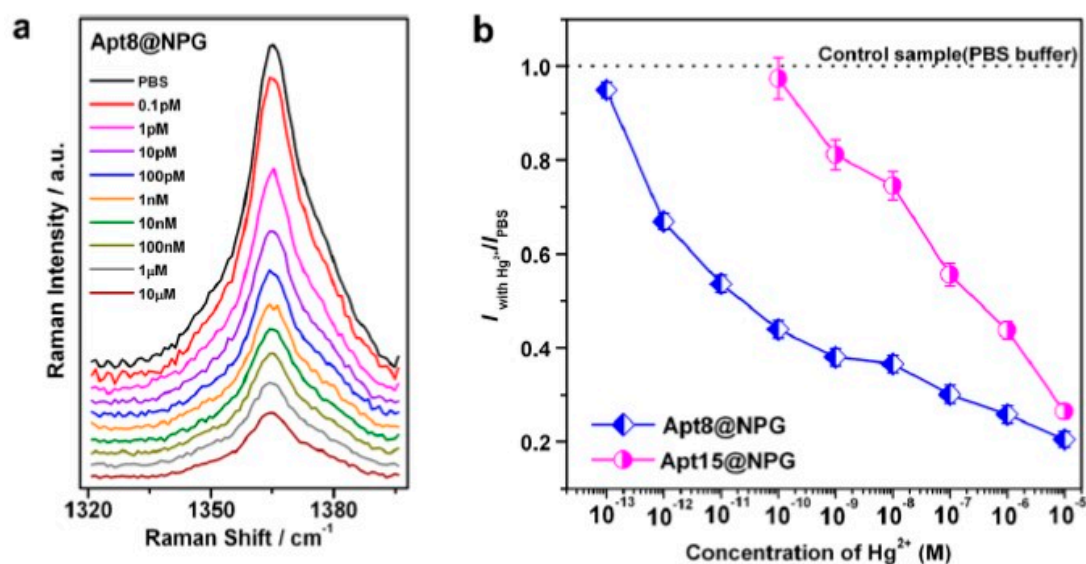

Figure 23. Quantitative response of the NPG sensor: (**a**) the main Raman peak of Cy5, at 1365 cm^{-1} changing the concentration of Hg^{2+} in the buffer solution. A significant decrease of the intensity of the peak is observed by increasing the Hg^{2+} concentration. (**b**) Plot of the normalized intensity (normalized to the intensity of the peak with PBS buffer only) of the peak at 1365 cm^{-1} versus the Hg^{2+} concentration. The comparison of the data obtained by using aptamer with 15 T (15 number of thymine bases, Apt15) and 8 T (8 number of thymine bases, Apt8) is reported. Reproduced with permission from [57]. Copyright American Chemical Society, 2013.
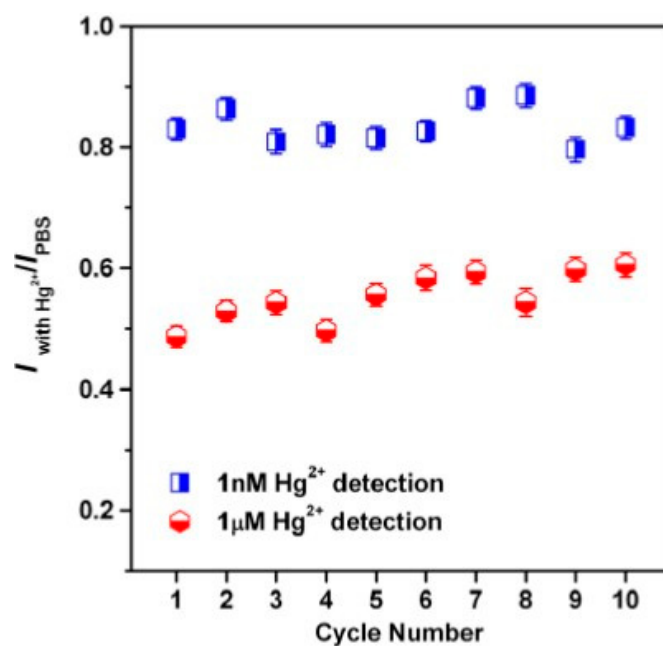
Figure 24. Recyclability test of the NPG/aptamer sensor. Normalized peak intensities of the 1365 cm^{-1} band with 1 nM or 1 μm Hg^{2+} in the aqueous solution for 10 cycles. Reproduced with permission from [57]. Copyright American Chemical Society, 2013.

3.2. Electrochemical Sensing

Electrochemical sensors operate by the target material coming into contact with the electrode surface and undergoing a redox reaction, which produces an electrical signal that can then be attributed to the specific analyte material. In this section, we illustrate the use of NPG system as the electrode surface for the electrochemical detection of some notable analytes, highlighting the peculiar role played by the NPG, through its specific properties, in the sensing mechanism.

Liu et al. [74] used dealloyed prepared NPG as the working electrodes to investigate the redox behavior of p-nitrophenol (p-NP) by cyclic voltammetry (CV), so to fabricate a high-performance (high sensitivity and selectivity) electrochemical sensor to be used in detecting traces of p-NP in wastewaters. In particular, the authors produced NPG leafs by dealloying Au$_{42}$Ag$_{58}$ alloy leafs in concentrated HNO$_3$. Then, they performed cyclic voltammetric measurements (at room temperature) by using a standard three-electrode cell: a saturated calomel electrode (SCE) was used as the reference electrode, a Pt slab as the counter electrode, and the NPG leaf as the third electrode. The measurements were performed with the electrodes within a H$_2$SO$_4$ solution containing selected concentrations of the p-NP. As an example, Figure 25 reports cyclic voltammograms for the redox of p-NP in 0.1 mol/dm^3 H$_2$SO$_4$ solution on an NPG electrode and, for comparison, on bulk Au (a polycrystalline Au electrode, indicated as poly-Au, which is a 0.8 mm-diameter Au wire). The voltammograms of poly-Au electrode are formed by a couple of reversible redox peaks around 0.5 V and an intense reduction peak starting at about 0.1 V in the cathodic scan. Instead, the cyclic voltammograms obtained by using the NPG electrode show the redox peaks at about 0.5 V and these peaks are sharper and more symmetric with slight positive shift of peak potentials; in addition, the reduction peak at about 0.1 V turned into a very small peak in the second potential sweep, and remained unchanged thereafter. This changes with respect to bulk Au are attributed to the fact that the p-NP molecules adsorb more easily on the rough surface of NPG than on the smooth surface of poly-Au. As a consequence, on the NPG surface a higher coverage of p-NP is realized and only a small amount of p-NP from the bulk electrolyte is allowed to be electroreduced at the electrode/solution interface, thereby generating a small current signal since the second potential scan. So, clearly, the redox behavior of p-NP on the Au surface is dictated by the microstructure and surface morphology of the electrodes.
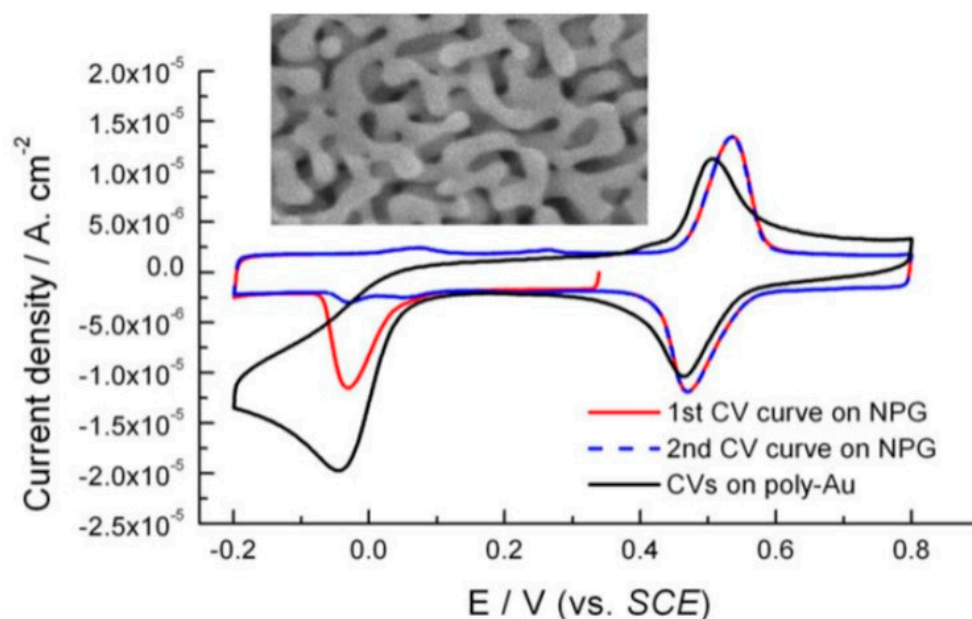
Figure 25. Comparison of cyclic voltammograms (acquired at scan rate of 50 mV/s) for a polycrystalline Au (poly-Au) electrode and an NPG electrode immersed in 0.1 mol/dm^3 H$_2$SO$_4$ with 12.5 mg/dm^3 p-nitrophenol (p-NP). The inset shows a typical SEM image of NPG electrode. Reproduced with permission from [74]. Copyright Elsevier, 2009.

Figure 26a reports voltammograms acquired by using the NPG electrode in H$_2$SO$_4$ solutions changing the p-NP concentration of p-NP and showing that the voltammetric response is unaffected by the p-NP concentration in the 0.2–0.4 V range while the redox peaks, occuring between 0.40 V and 0.63 V, are highly sensitive to the p-NP concentration: the higher the p-NP concentration, the larger the currents of the redox peaks. In this regard, in particular, Figure 26b shows that the peak area of each peak increases linearly (dots) with the concentration of p-NP in the concentration range from 0.25 to 10 mg/dm^3. The linear fits (full lines) give the linear response of the NPG sensor. In addition, as reported in Figure 26c, the authors investigated the concentration dependence of absorbance of p-NP by using UV-visible absorbance measurements and obtaining, also in this case, a linear relationship between absorbance at 400 nm and p-NP concentration in the 0.25–10 mg/dm^3 range. These data clearly show the feasibility of the NPG-based electrochemical sensor, for monitoring trace p-NP in water. Additionally, the sensor selectivity in detection of p-NP was investigated: to this end, the authors proved that the currents and peak potentials for the reversible redox waves are not affected by other NP isomers, such as ortho-nitrophenol (o-NP) and meta-nitrophenol (m-NP) concluding that, for example, the concentrations of p-NP and o-NP in a mixture solution can be determined simultaneously based on the linear dependence between their concentration and peak current. The same is true for the mixture of p-NP and m-NP.
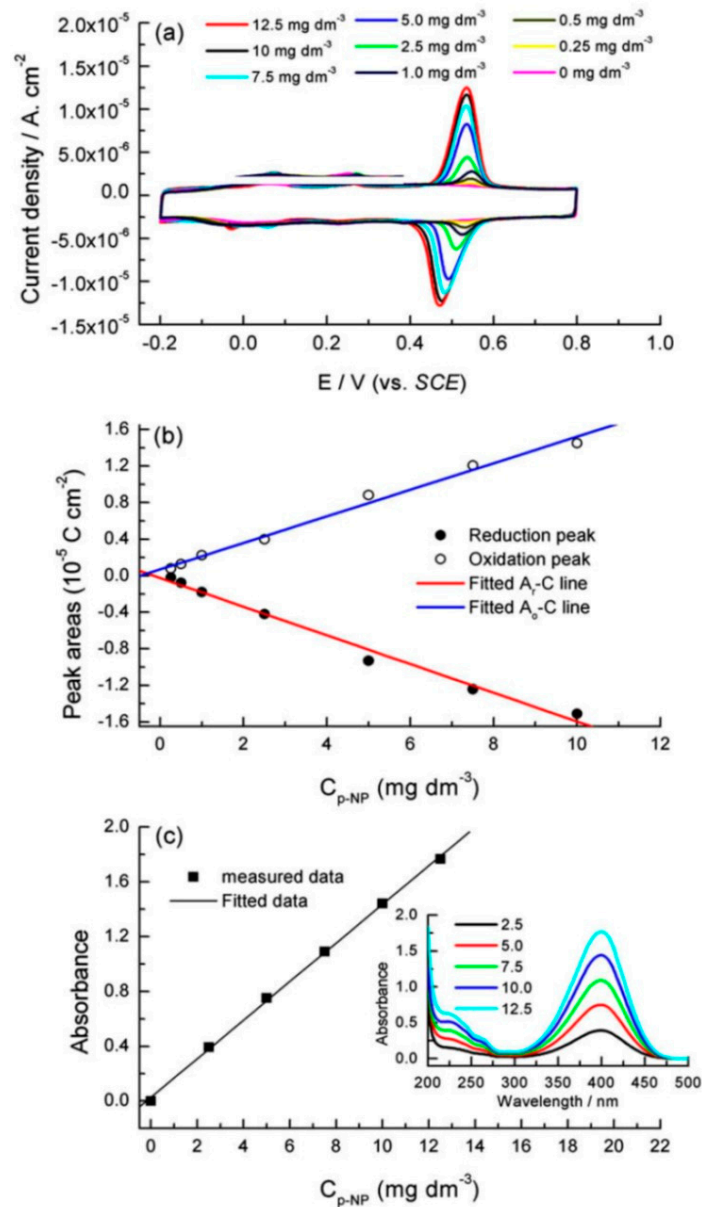
Figure 26. (**a**) Cyclic voltammograms (acquired at scan rate of 50 mV/s) corresponding to NPG electrode in 0.1 mol/dm³ H₂SO₄ containing different concentrations of p-NP. (**b**) Plot (showing a linear correlation) of the redox peak areas versus the p-NP concentration in the solution. (**c**) Plot (showing a linear correlation) of the absorbance intensity at the wavelength of 400 nm of the solution containing p-NP versus the p-NP concentration in alkaline solutions at pH 10–11. The inset shows series of UV-visible absorption spectra of p-NP at different concentrations (labels in mg/dm³) in alkaline solutions at pH 10–11. Reproduced with permission from [74]. Copyright Elsevier, 2009.

On the other hand, however, they observed that UV-visible measurements are not able to determine separately the concentration of each NP in the mixtures, highlighting the great advantage of NPG-based electrochemical sensor with respect to an NPG-based optical sensor. Concerning the stability of the NPG electrode and the consequent stability of its response after several measurements cycles, the authors observed that the surface morphology of the NPG electrode is unchanged (except for a tiny increase in the ligament sizes, see Figure 27) after thousands of potential cycling and, correspondetly, after thousands of voltammometric measurements, the system furnishes stable and unchanged peak current values during the measurements. In particular, after one electrochemical measurement, the NPG electrode can be cleaned easily and reused by holding the potential at more positive potentials (over 1.0 V) for tens of seconds to remove NPs and their intermediates adsorbed on the NPG surface.
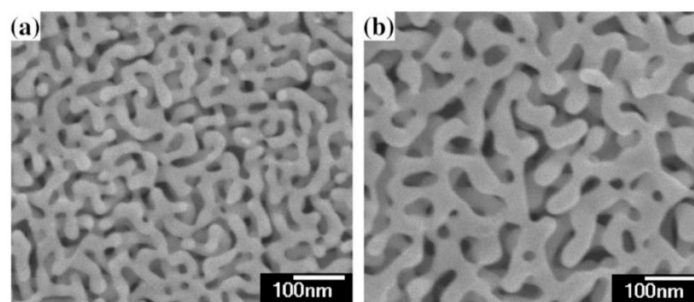
Figure 27. (**a**) Scanning electron microscopy image of the surface of NPG electrode before use (i.e., before cyclic voltammetry measurements); (**b**) Scanning electron microscopy image of the surface of NPG electrode after several uses (i.e., after several runs of cyclic voltammetry measurements). Reproduced with permission from [74]. Copyright Elsevier, 2009.

Another example is reported by Meng et al. [75], concerning the use of NPG as non-emzymatic electrochemical sensor of H_2O_2. In this work, NPG leafs were prepared by dealloying 12-carat AuAg alloy in concentrated HNO_3 for 30 min at 303 K. The leaf was then attached onto the glassy carbon electrode of a standard three electrodes electrochemical cell, including the NPG electrode as the working electrode, a saturated calomel electrode (SCE) as the reference electrode, and a Pt slab as the counter electrode. The electrodes were immersed in PBS (pH = 7) solutions containing selected concentrations of H_2O_2 so to exploit the H_2O_2 reduction (as dictated by the following reactions in sequence: (a) $H_2O_2 + e^- \rightarrow OH_{ad} + OH^-$, (b) $OH_{ad} + e^- \rightarrow OH^-$, (c) $2OH^- + 2H^+ \rightarrow 2H_2O$) as a sign of its presence in the cyclic voltammograms plots. Figure 28 shows the comparison of the cyclic voltammograms acquired by using an electrode as the bare glassy carbon, a bulk Au plate and the NPG, by fixing the concentration of 10 mM of H_2O_2 in the solution. It can be recognized that there is no current response from H_2O_2 in the potential range from −0.6 to 0.2 V (vs. SCE) when using bare glassy carbon electrode. On the other hand, in the same potential range, a current peak occurs when using bulk Au and NPG as electrodes, however a significant current increase is obtained when using NPG indicating an active catalytic performance of NPG toward H_2O_2 reduction. In addition, the higher NPG surface area determines a much larger current density, in the reduction potential region, than bulk Au electrode under the same H_2O_2 concentration. It can be observed that the potential of reduction current peak of NPG is almost 200 mV earlier than bulk Au indicating the rapid reduction of H_2O_2 at NPG dictated by the improved activity of the in and out curved nanoscale Au ligaments. The authors evaluated, also, the apparent activation energy of the H_2O_2 reduction process on the NPG surface by fitting, using the typical Arrhenius equation, the experimental polarization curves of NPG electrode in neutral PBS solution containing H_2O_2 and acquired at different temperatures in the potential region between −0.6 V and −0.1 V.
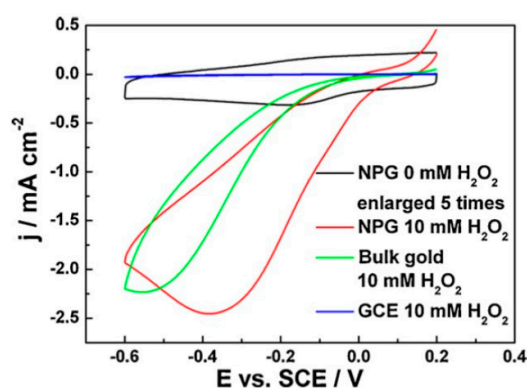

Figure 28. Cyclic voltammograms (acquired at scan rate of 50 mV/s) of reference glassy carbon electrode (GCE), bulk Au electrode and NPG electrode in neutral PBS solution containing 10 mM H_2O_2. Reproduced with permission from [75]. Copyright Elsevier, 2011.

Their results indicate a mean value of 30 kJ/mol for the reduction reaction of H_2O_2 over the NPG surface, which is a value much lower than the activation energy of the standard reduction reaction of H_2O_2 (~50 kJ/mol), confirming the electrocatalytic role of the NPG.

To complete this study, Figure 29A shows cyclic voltammetry curves of NPG in 0.1M PBS (pH = 7.0) changing the concentration of H_2O_2 in the solution: the cathodic peak currents increase by increasing the H_2O_2 concentration. Then, the value of the current peak at −0.4V vs. SCE was chosen for the detection of H_2O_2 due to its largest current response, and this peak current is plotted versus the H_2O_2 concentration in Figure 29B obtaining a linear response of the sensor in the investigated concentration range. Finally, as usual, the authors also tested the selectivity of the system in presence of some other possible co-existing compounds in real biological samples as methanol (1 mM), ethanol (1 mM), glucose (0.5 mM), and ascorbic acid (0.2 mM), see Figure 30A.
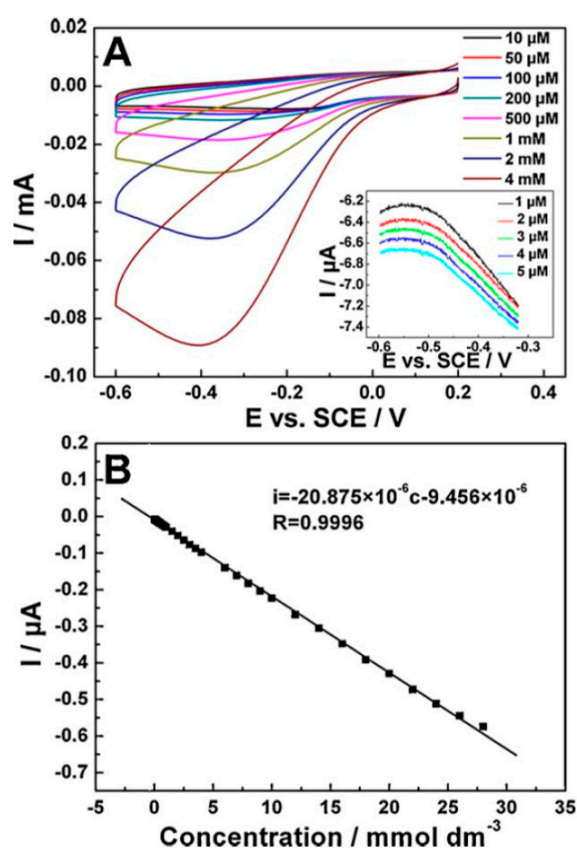

Figure 29. (**A**) Cyclic voltammograms (acquired at a scan rate of 50 mV/s) of NPG electrode in neutral PBS solution changing the H_2O_2 concentrations. (**B**) Plot of current response of the NPG electrode versus the H_2O_2 concentration in the solution. Reproduced with permission from [75]. Copyright Elsevier, 2011.
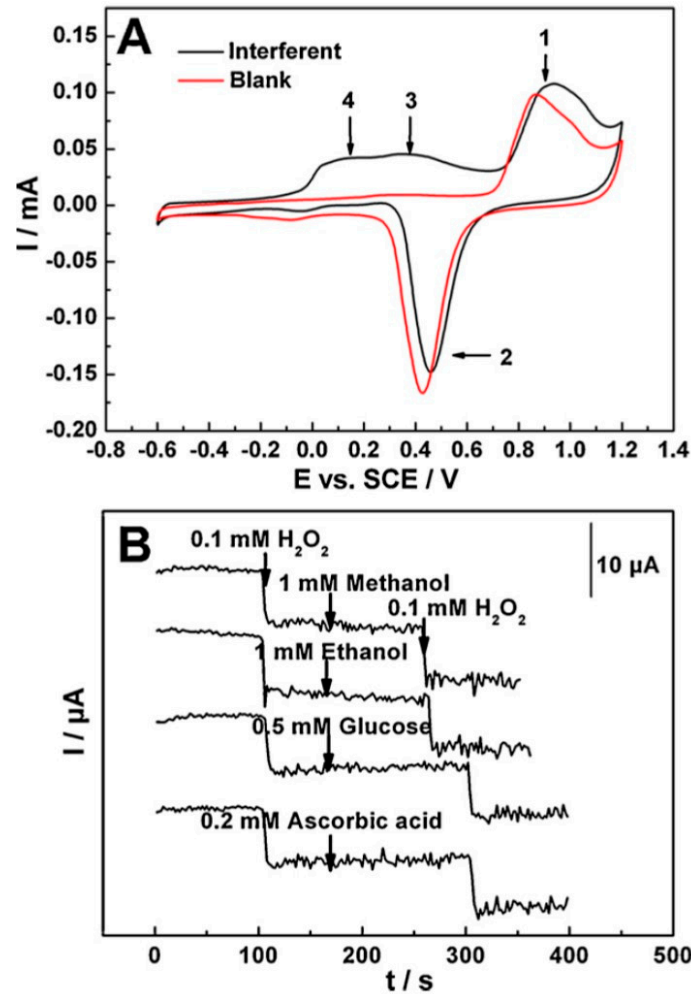
Figure 30. (**A**) Cyclic voltammograms of NPG electrode in blank and the interferent solutions; (**B**) Amperometric responses of NPG in PBS (pH = 7.0) toward 0.1 mM H_2O_2, 0.1 mM ascorbic acid, 1 mM methanol, 1mM ethanol, and 0. 5mM glucose at −0.4 V versus saturated calomel electrode (SCE). Reproduced with permission from [75]. Copyright Elsevier, 2011.

The results show that there is no evident reductive current in the H_2O_2 reducing potential from −0.6 V to 0 V (versus SCE). The current peaks 1 and 2 agree with the oxidation and reduction of Au, respectively, while current peaks 3 and 4 can be attributed to the oxidation of the interferents including methanol (1 mM), ethanol (1 mM), glucose (0.5 mM), and ascorbic acid (0.2 mM). Hence, the results suggest no response of NPG electrode toward the interferents in H_2O_2 reducing potential region. The selectivity of NPG leaf toward H_2O_2 reduction was also investigated by the amperometric response at −0.4V (versus SCE), see Figure 30B: in this test, the authors first added the H_2O_2 solution in the electrochemical cell and, then added the interferentt. It can be seen that an amperometric response occurs once 0.1mM H_2O_2 is added. Methanol (1 mM), ethanol (1 mM), glucose (0.5 mM), and ascorbic acid (0.2 mM) addition, instead, do not determine any further amperometric changes. When one more 0.1 mM H_2O_2 is added, the current changes proportionally even with the existence of the interferents, showing the strict selectivity of the NPG to H_2O_2. Interestingly, the authors evaluated, also, the selectivity and applicability of NPG electrode in real samples: they tested the electrochemical response of the NPG electrode in water samples such as drinking water, tap water, and river water containing H_2O_2. The detection results showed, in these cases, an excellent selectivity with a deviation lower than 15%. Finally, concerning stability of the NPG electrode under several measurements and passing time, the authors verified that before and after various tests the system showed a deviation no more than 5%, and the results of 9 equivalent electrodes showed a deviation no more than 15%.

Additionally, NPG electrode was placed in air to evaluate the long-term stability without any protection for three months after initial studies and the authors verified that (at the current of −0.4 V versus SCE) the NPG electrode in 10 mM H_2O_2 maintains 85% of original value, indicating an excellent long-term stability.

Chen et al. [76] reported on the use of free-standing NPG leafs for non-enzymatic electrochemical detection of glucose. In particular, the authors investigated the effects of pore sizes, detecting potentials and chloride ions on glucose oxidation and finding that NPG with smaller pore size possesses higher sensitivity. In addition, the NPG-based glucose sensor was found to be highly selective, avoiding interference from the oxidation of common organic interferents in body liquids. In this work, the authors prepared NPG leafs by dealloying $Au_{35}Ag_{65}$ (at.%) alloy leafs in concentrated HNO_3 solution at room temperature and increasing the dealloying time so to obtain NLG leafs with different pores size. In particular, using dealloying times of 15, 120, 240, 480 min, they obtained NPG leafs with mean pores sizes of 18, 30, 40, 50 nm, respectively. These NPG leafs were attached to a glassy carbon electrode so to be used as the working electrode in a three-electrodes standard electrochemical cell with the others two electrodes being a saturated Ag-AgCl electrode (reference electrode) and a Pt plate electrode (auxiliary electrode). The electrocatalytic activity of NPG electrodes toward glucose oxidation was investigated in a nearly neutral phosphate buffer solution (PBS, pH 7.4). As a first example, Figure 31a reports cyclic voltammograms by using NPG electrodes with different average pores sizes (18, 30, 40 nm), and the inset shows, as a comparison, the cyclic voltammogram acquired by using a bulk Au plate as an electrode. The voltammograms acquired by using NPG electrodes in the PBS solution without glucose show the OH^- adsorption process on Au starting from 0 V and giving origin to a broad peak between 0.3 and 0.4 V, according to the reaction $Au+H_2O \rightarrow Au(OH)_{ads}^{(\lambda-1)} + H^+ + \lambda e^-$. So, the OH^- adsorption plays a key role in the electro-oxidation of glucose. However, the electrochemical activity of the bulk polycrystalline Au sheet in the PBS solution does not show obvious peak corresponding to the OH^- adsorption process: hence, the authors conclude that the adsorption peak shift in Figure 31a indicates that NPG films with a smaller pore size contain a higher number of electrochemically active surfaces so enhancing the reaction efficiency. Figure 31b reports the cyclic voltammograms of a PBS solution with 50 mM glucose. Considering the positive potential cycle, the curves show two anodic oxidation peaks located at 0.1 and 0.3 V: the peak, at 0.1 V is determined by the formation of $Au(OH)_{ads}$, electrosorption of glucose and the generation of intermediates; the peak at 0.3 V is due to the oxidation of both intermediates and glucose by the formation of gluconolactone through the catalytic effect of $Au(OH)_{ads}$. As a comparison, the inset in Figure 31b reports the glucose oxidation voltammograms using as electrode the polycrystalline Au plate: due to the weak OH-adsorption, no electrocatalytic activity is detected on the bulk Au sheet. The decrease in current after the second peak is caused by the oxidation of Au surfaces that inhibits further electro-oxidation of glucose. During the negative scan, the Au oxide is reduced to form a fresh gold surface that catalyzes the direct glucose oxidation at 0.3 V. At lower potentials, the glucose electrosorption and the intermediate accumulation take place again on the gold ligament surfaces, as indicated by the current peak in the potential between 0.1 V and 0.2 V. Figure 31b clearly shows that the glucose oxidation is strongly affected by the pore sizes of NPG. For the second anodic peak both in positive and negative scans, the intensities of oxidation peak at 0.3 V clearly increase with decreasing pore size, whereas the intensities of the first current peaks at 0.1 V decrease, indicating that the nanoporous films with smaller pores size present an enhanced activity toward the oxidation reaction of glucose. To further analyze the NPG characteristics in the electrochemical detection of glucose, Figure 31c,d report the chronoamperometry curve of NPG electrode with average pore size of 18 nm in 0.1 M PBS solution with successive addition of 1 mM glucose at the constant potentials of 0.1 V (c) and 0.3 V (d). In both cases, the current density increases sensitively and rapidly with each addition of glucose. However, the incremental amount of current signal at 0.1 V tends to decrease gradually, while the current response at 0.3 V increases linearly with the increments in glucose concentration. The insets in these figures show the relationship between current density and glucose concentration: a linear relationship is obtained which, combined with the excellent sensitivity, indicates that the direct oxidation reaction of glucose catalyzed by NPG is

very sensitive to the concentration changes at 0.3 V, in particular. Regarding enzyme-free glucose detection, one challenging aspect concerns the tolerance of chloride ions in physiological environments. Hence, the authors investigated this point by the measures in Figure 32: Figure 32a shows the cyclic voltammogram of glucose oxidation catalyzed by NPG electrode (30 nm pores size) in a PBS solution containing 20 mM glucose and 0.1 M KCl, and the curve corresponding to glucose oxidation without KCl is, also, shown for comparison. The addition of chloride ions determines the decrease of the intensity of both electrosorption and direct oxidation peaks. The presence of the chloride ions also causes a slight peak shift of the direct oxidation reaction. However, the intensity reduction of electrosorption peak is much more significant than that of the direct oxidation. This may be associated with the competitive adsorption between chloride ions and glucose molecules.
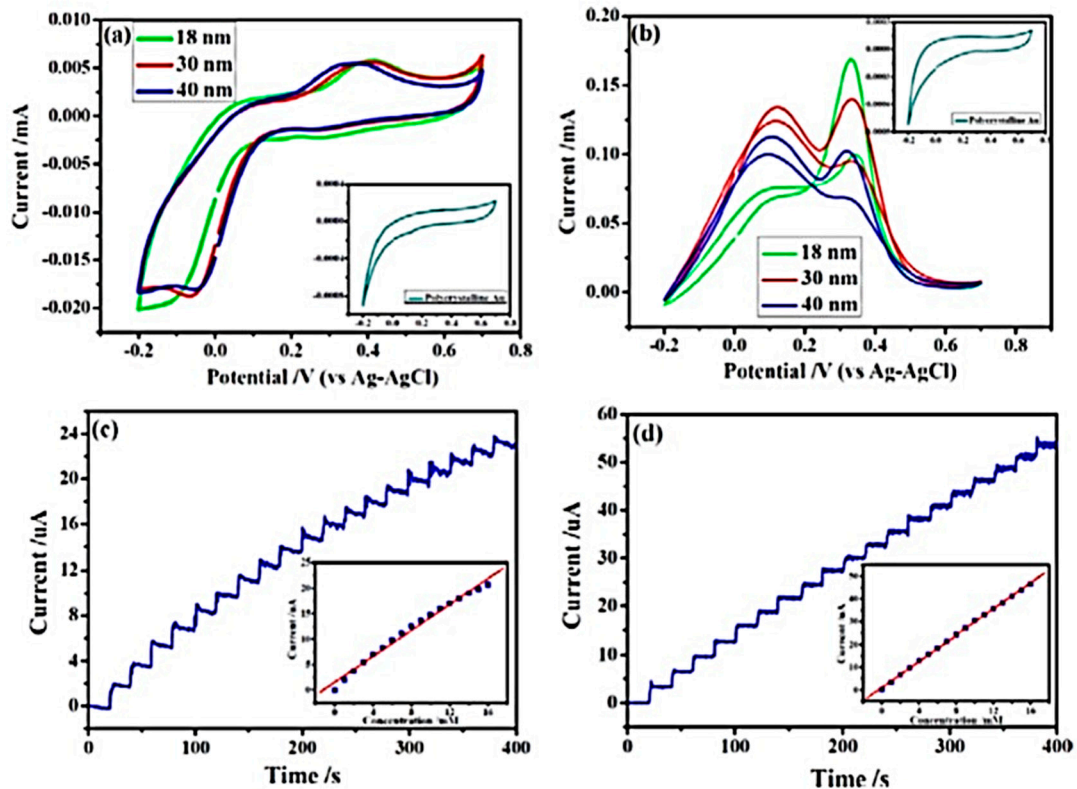

Figure 31. Cyclic voltammograms of NPG with different pore sizes (18, 30, 40 nm) and, for comparison, of polycrystalline Au (inset), acquired with the electrodes in 0.1 M PBS solution (**a**) and with the electrodes in 0.1 M PBS solution containing 50 mM glucose (**b**) (scan rate: 50 mV/s). Chronoamperometry curves of NPG with pore size of 18 nm in 0.1 M PBS solution with successive addition of 1 mM glucose at the constant potentials of (**c**) 0.1 V and (**d**) 0.3 V, respectively. Reproduced with permission from [76]. Copyright Elsevier, 2011.
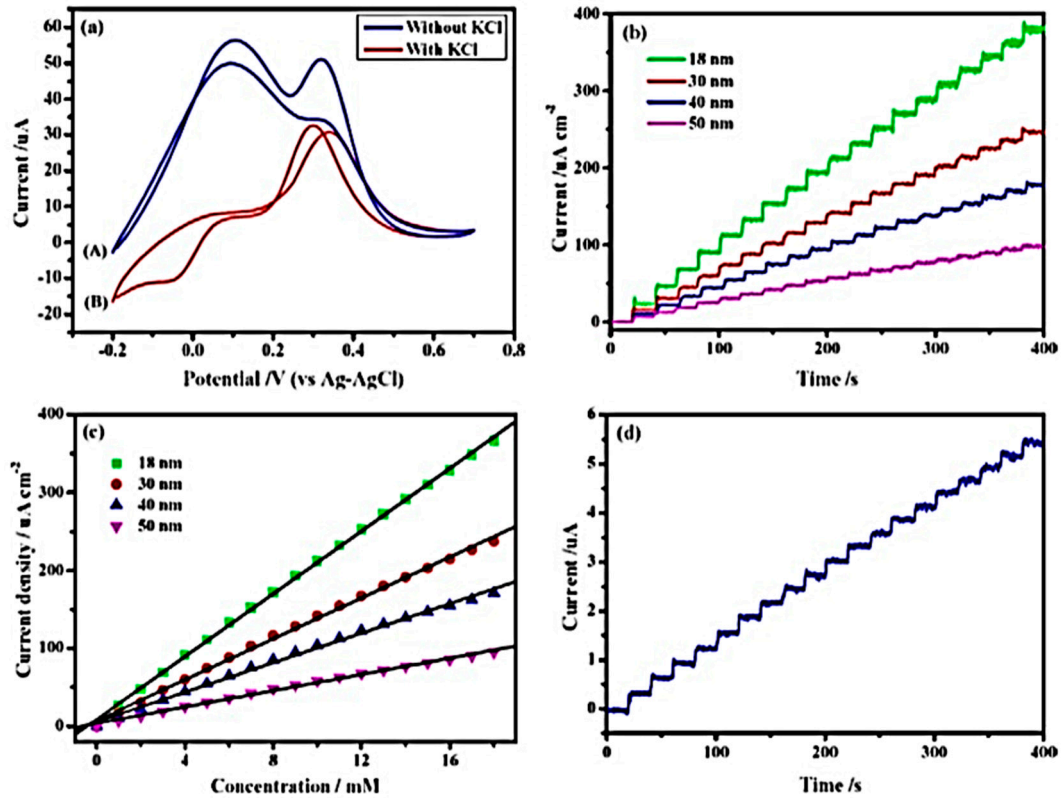
Figure 32. (**a**) Cyclic voltammograms corresponding to the NPG electrode with pore size of 30 nm in 0.1 M PBS solution containing 20 mM glucose (A) without KCl and (B) with 0.1 M KCl (scan rate: 50 mV/s). (**b**) Chronoamperometry mesurements and (**c**) calibration curves of NPG with different pore sizes (18, 30, 40, 50 nm) in 0.1 M PBS and KCl solution with successive addition of 1 mM glucose at the potential of 0.3 V. (**d**) Chronoamperometry curve of NPG with pore size of 18 nm in 0.1 M PBS and KCl solution with successive addition of 0.1 mM glucose at the potential of 0.3 V. Reproduced with permission from [76]. Copyright Elsevier, 2011.

The NPG pores size effect on the glucose sensitivity is studied by the measures presented in Figure 32b, presenting chronoamperometry curves for various NPG electrodes in a PBS solution containing 0.1 M KCl at a detecting potential of 0.30 V: the plots indicate that, with successive additions of 1 mM glucose to the solution, the current density increases sensitively and reaches 95% of the steady-state value within 2 s. The smaller the pore sizes of NPG, the higher the current response. From the corresponding calibration plots in Figure 32c, it can be observed that the current signals increase linearly with the incremental glucose concentration in the entire physiological concentration range, 3–8 mM. In particular, the amperometric response to glucose of the NPG with a pore size (18 nm) presents the highest sensitivity as can be recognized from the curve in Figure 32d: the sensitivity of 20.1 $\mu A/cm^2$ mM in the 1–18 mM concentration range, with a detection limit of 3 μM at a signal-to-noise ratio of 3.0. The NPG glucose sensor is, also, stable against cycling tests of glucose oxidation in the neutral PBS solution: after 500 cycling tests, the electrocatalytic activity of NPG reduces by less than 10%, corresponding to slight increases in pore size. Finally, regarding the NPG glucose sensor selectivity, the authors investigated the amperometric response of glucose on NPG in the simultaneous presence of 0.1 mM ascorbic acid (AA) and 0.02 mM uric acid (UA) in a PBS solution, see Figure 33: no interference from AA or UA in the glucose detection can be recognized. Such a selectivity is attributed to the different dependences of glucose and the interfering molecules on the NPG electrode since the glucose electro-oxidation is a kinetically controlled process (which is very sensitive to the surface area of NPG, while the oxidations of UA and AA are diffusion-controlled processes (which do not depend significantly on the electrode area).
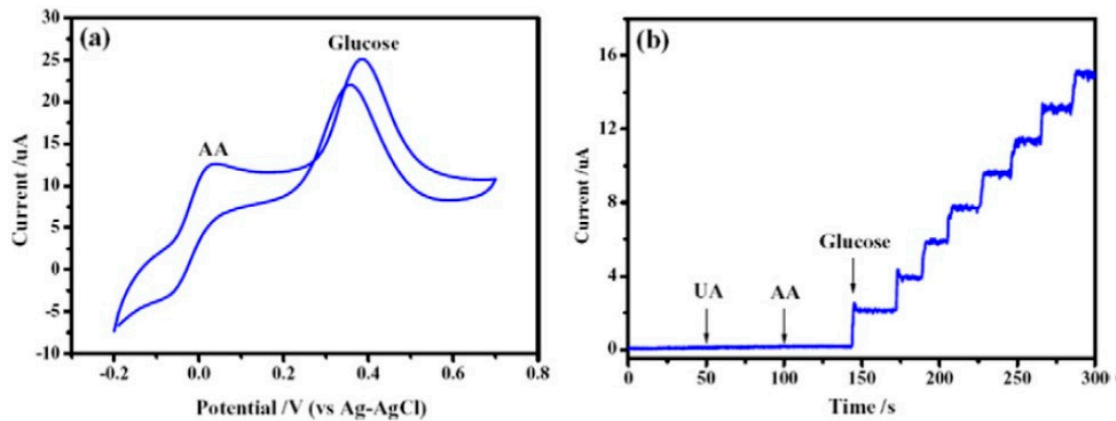
Figure 33. (**a**) Cyclic voltammograms curves of NPG with pore size of 18 nm in 0.1 M PBS and KCl solution containing 10 mM glucose and 0.1 mM ascorbic acid (AA) (scan rate 50 mV/s). (**b**) Chronoamperometry curves of NPG with pore size of 18 nm in 0.1 M PBS and KCl solution with successive addition of 0.02 mM uric acid (UA), 0.1 mM AA, and 1 mM glucose. Reproduced with permission from [76]. Copyright Elsevier, 2011.

NPG films finds excellent application, also, as an electrochemical DNA bio-sensor, according to Daggumati et al. [77]. The authors chose NPG due to its affinity to nucleic acid. Hence, they prepared NPG films on glass siles by dealloying 600 nm-thick Au-Ag alloy layer. In addition, a group of dealloyed samples were annealed (225 °C–210 s) to change the average pores size. In the as-dealloyed samples, the typical pore size was between 20 and 120 nm. During the annealing process, the increase of the surface diffusion of Au atoms causes the coarsening of Au ligaments and expansion of cracks. The side walls of cracks in the annealed NPG films offer additional surfaces for ionic transport and additional surfaces for molecular permeation into the NPG film. DNA was immobilized on the NPG electrodes: after electrodes cleaning, the electrodes were incubated in an immobilization solution containing 25 mM phosphate buffer (PB), 2 μM thiolated probe DNA, and 50 mM $MgCl_2$ for 1.5 h at room temperature. In addition, the authors investigated the DNA−MB (methylene blue) interaction by incubating the DNA functionalized NPG electrodes in 20 μM MB prepared in 1× PBS solution. The electrochemical measurements were performed by using a standard three-electrodes electrochemical cell and by using the NPG electrode as the working electrode (Pt wire and Ag/AgCl electrodes were used as counter and reference electrodes, respectively). For control measurements, covalently conjugated MB−DNA was employed. The probe modified NPG electrode was challenged with different concentrations of target DNA. In addition, the electrochemical measurements were, also, performed by using a bulk flat Au leaf as comparison. The authors performed both cyclic voltammetric measurements (with the electrodes in 0.05 M sulfuric acid) and square wave voltammetry (to study the probe grafting and target hybridization on the electrodes, and these measures were performed in 1× PBS over the potential range of 0 to −0.5 mV with an amplitude of 40 mV, step size of 4 mV, and pulse frequencies ranging from 3 to 60 Hz). Figure 34 reports the cyclic voltammograms recorded for flat bulk Au and NPG films, indicating a strong increase in the current values for NPG respect to the flat bulk Au electrode. The electrical charge under the Au oxide reduction peak between the potentials 720 and 970 mV is converted into the effective surface area by using 450 μC/cm² as the specific charge required for Au oxide reduction. Hence, an enhancement factor, E_h, is defined as the ratio of the effective surface areas of different NPG electrodes (as-dealloyed and annealed) to the effective surface area of control flat bulk Au electrode. Following this definition, the inset in Figure 34 shows the enhancement factor for the three tested electrodes (flat bulk Au, as-dealloyed NPG, annealed NPG): E_h = 9.26 for as-dealloyed NPG, E_h = 2.41 for annealed NPG (and, obviously E_h = 1 for flat bulk Au), a much lower value probably resulting from larger pores and from a smaller density of pores as determined by the pores coalescence process induced by the thermal annealing. So, as dealloyed NPG film and annealed NPG film are characterized by a surface, respectively, 9.26 and 2.41 times higher than the surface area of the flat bulk Au.
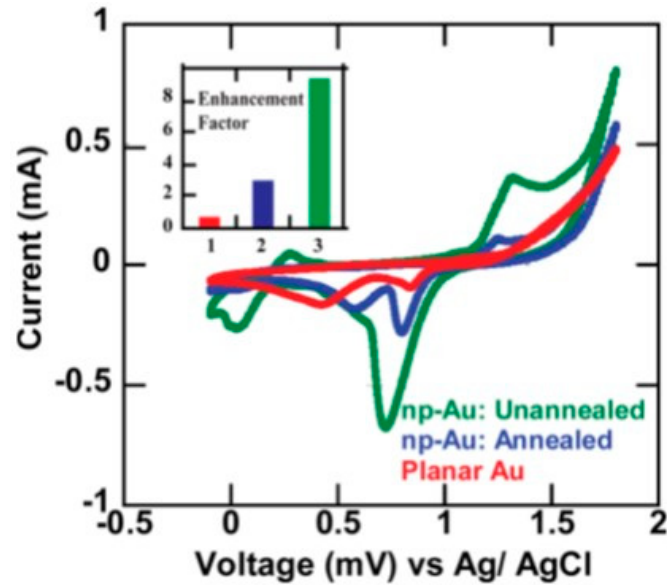
Figure 34. Cyclic voltammograms using as electrode NPG film (green curve), annealed NPG film (blue curve), and bulk planar Au (red curve) and acquired in 0.05 M sulfuric acid solution (scan rate of 50 mV/s). The inset shows the enhancement factors obtained by using (1) the bulk planar Au film, (2) the annealed NPG film, (3) the as-fabricated NPG. Reproduced with permission from [77]. Copyright American Chemical Society, 2015.

Concerning the interaction of methylene blue (MB) DNA-probe functionalized NPG electrodes, the authors stydies are conducted by using square wave voltammetry, see Figure 35a. In this case, the recorded peak current in NPG films is ten times higher than reference flat bulk Au (Figure 35b), corresponding to the 9.26 times higher surface area: therefore, this is an indication that the entire NPG surface is participating in the electrochemical reaction. The authors observed, as is clear from Figure 35a,b a decrease in the MB peak current with successive square wave voltammetry cycles in both NPG and flat bulk Au electrodes, ascribing this phenomenon to the dissociation of MB from electrode surface into the electrolyte solution.
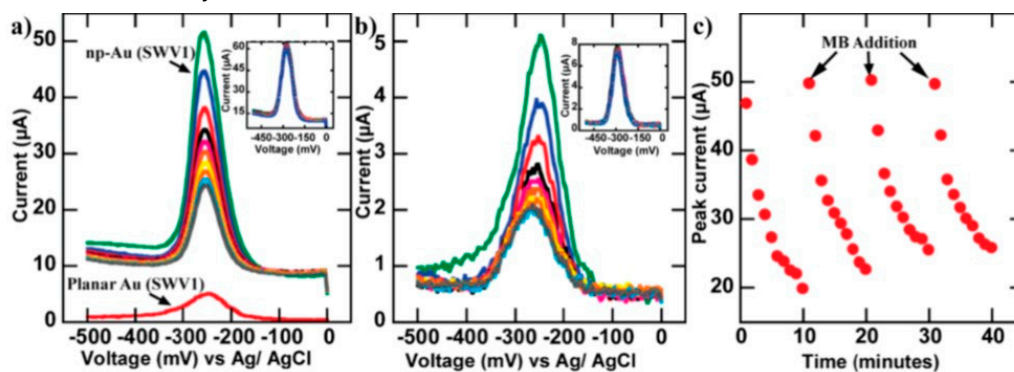

Figure 35. Square wave voltammetry measurements obtained from probe-modified electrodes towards methylene blue in 1× PBS solution. Signal decay with successive square wave voltammetry scans for (**a**) as-fabricated NPG film, (**b**) bulk planar Au film. Insets: square wave voltammetry scans of methylene blue-tagged probe DNA in 1× PBS solution on (**a**) as-fabricated NPG film, (**b**) bulk planar Au film. (**c**) Signal regeneration by addition of fresh methylene blue after every ten square wave voltammetry scans. The plot shows signal decay and regeneration upon methylene blue replenishment in NPG films. Reproduced with permission from [77]. Copyright American Chemical Society, 2015.

Transport limitation, especially for MB to penetrate the porous structure once dispersed into the electrolyte, is more significant in NPG films due to their three-dimensional complex structure. Therefore, the extent of signal reduction is greater in NPG (65%) compared to flat bulk Au (50%). The MB signal, then, is regenerated before performing DNA target hybridization. To this end, the authors depleted the MB signal by performing 10 consecutive square wave voltammetry cycles and the probe-grafted sample was again incubated with fresh MB to instate a definite. The initial signal is, so, regenerated multiple times by successive depletion and regeneration steps, as shown in Figure 35c. The regenerated signal was within 5% of the initial signal after each MB replenishment cycle. This ensures that the signal reduction is only ascribed to the target and not to the signal decay upon multiple scans. This technique of MB replenishment enables the same NPG electrode to be used successively for the detecting multiple concentrations of target DNA molecules. The amplitude of the peak current, therefore, can be used to characterize the bound target in case of square wave voltammetry-based sensors. The electrode morphology affects the signal amplitude and the NPG electrode, presenting the highest surface area, results as the best sensor since displays the highest signal enhancement. However, to obtain the best sensitivity, the frequency that allows the participation of the entire surface in the redox reaction should be selected. Hence, the authors, investigated the response of probe-functionalized NPG films (both unannealed and annealed) to MB at square wave voltammetry frequencies in the range 3 to 60 Hz, see Figure 36.
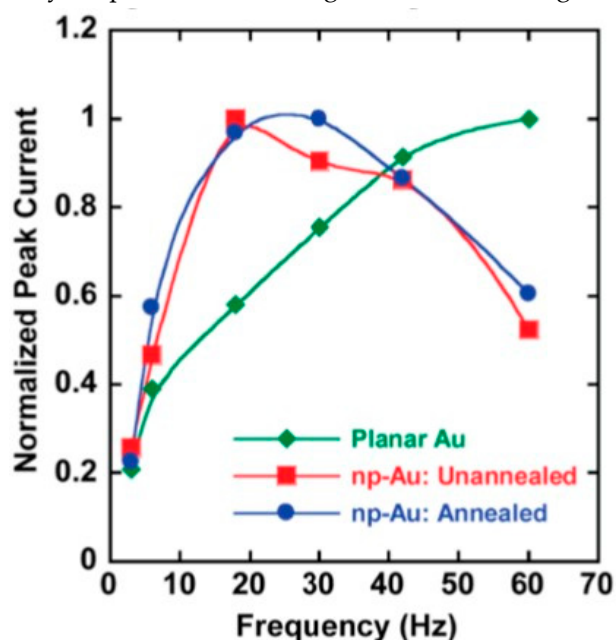

Figure 36. Square waves voltammograms obtained from probe-modified electrodes response to methylene blue (MB) from 3 to 60 Hz. The plot reportss the peak current versus the frequency for as-fabricated NPG film (red dots), annealed NPG film (blue dots) and bulk planar Au film (red dots). The peak current is normalized to the maximum peak current value obtained at the critical frequency for NPG films and the saturation current value for bulk planar Au. Full lines are only guides for the eyes. Reproduced with permission from [77]. Copyright American Chemical Society, 2015.

Regarding the flat bulk Au electrode, the signal amplitude increases with frequency until 60 Hz and then saturated: 60 Hz is, therefore, the best frequency for sensor operation. However, in case of NPG films, signal amplitude increased until a certain critical frequency (18 and 30 Hz for as-dealloyed and annealed NPG, respectively) and decreased at higher frequencies. Thus, critical frequency for obtaining the maximum square wave voltammetry amplitude depends on the morphology of the NPG film: this result can be ascribed to the fact that the flux area available for ionic transport increased in annealed NPG films making the structure more accessible, thereby incrasing the critical frequency from 18 Hz in unannealed films to 30 Hz in thermally treated films. These critical frequencies are, hence, the best operating frequencies for as-dealloyed and annealed NPG electrodes-

based sensors. Finally, the authors, to determine the detection range of target DNA, investigated the sensors response with different concentrations of target DNA. The results of these studies demonstrated that the square wave voltammetry-based sensors were able to detect DNA target concentrations as low as 500 pM with annealed NPG films.

In addition to the use of NPG as electrochemical sensor for various analytes, also NPG-based composites were largely tested: essentially, systems formed by NPG and a second decorating component are produced so as to obtain artificial functional nanomaterials presenting new properties and functionalities arising from the synergistic effects of both the components [82–84]. So, exploiting the specific interaction from NPG and the second nanosystem, an overall composite can be obtained presenting improved sensing performances with respect to the single components.

As an example, Qiu and Huang [82] studied the effects of Pt decoration on the electrocatalytic activity of NPG electrode toward glucose and its potential application for producing a nonenzymatic glucose sensor. In particular, the authors verified, by using voltammetry and amperometric approaches, that the electrocatalytic activity of NPG in neutral condition is improved by the addition of selected amount of Pt which decorates the NPG. This improved electrocatalytic activity, in turn, results in improved performance of NPG-based electrodes toward the glucose oxidation (i.e., glucose electrochemical sensing). After preparing the NPG films, the authors decorated these NPG films by means of 'immersion–electrodeposition (IE): the produced NPG electrode was immersed in 10 mM H_2PtCl_6 solution for 600 s to allow soak and then the sample was transferred into 0.1 M $HClO_4$ solution. So, Pt is electrodeposited on the NPG by continuously sweeping the potential from −0.3 to 0.9 V for three cycles in the $HClO_4$ solution and the relative amount of deposited Pt can be controlled from about 20% to more than 80% (and in this last case, scanning electron microscopy images show Pt as agglomerated in nanoparticles). Using these electrodes as working electrodes in a standard three-electrodes electrochemical cell (which uses, aslso, a Pt wire as counter electrode and a saturated calomel electrode (SCE) as reference electrode), the electrochemical experiments were conducted. Figure 37 reports the cyclic voltammograms of the NPG-Pt electrodes with the increase of IE treatment, i.e., by increasing the amount of Pt decorating the NPG.
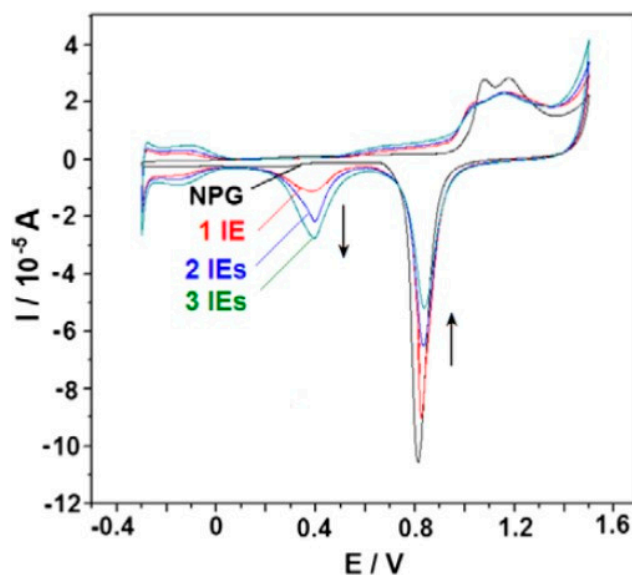

Figure 37. Cyclic voltammograms of NPG and Pt-decorated NPG electrodes acquired in 0.1 M $HClO_4$ solution (scan rate 50 mV/s). IE: refers to the NPG–Pt electrode fabricated by one time ''immersion electrodeposition'', 2IEs: refers to the NPG–Pt electrode fabricated by two times ''immersion-electrodeposition'', 3IEs: refers to the NPG–Pt electrode fabricated by three times ''immersion-electrodeposition''. Reproduced with permission from [82]. Copyright Elsevier, 2010.

In the plot, NPG refers to the curve acquired by using the basre NPG electrode, IE refers to the the NPG–Pt electrode fabricated by one time ''immersion electrodeposition'' (low amount of

deposited Pt), 2IEs refers to the NPG–Pt electrode fabricated by two times ''immersion-electrodeposition'' (increased amount of deposited Pt), 3IEs refers to the The NPG–Pt electrode fabricated by three times ''immersion-electrodeposition'' (further increased amount of deposited Pt). The peak around 0.9 V during the negative scan is determined by Au species, while the peak at 0.45 V is determined by Pt species. Increasing the treatment times of IE, the deposited amount of Pt increases and, correspondently, the charge corresponding to Pt oxides (0.4 V) increases. At the same time, the charge corresponding to Au oxides (0.8 V) decreases. As already observed by Chen et al. [76], also in this case Qiu and Huang [82] observe that, in comparison to a bulk flat Au disk electrode, the NPG electrode has a higher electrocatalytic activity toward the oxidation of glucose: by studying the cyclic voltammograms in PBS solution containing glucose, the authors observed, during the positive potential scan process, two anodic current peaks located at 0 V and 0.32 V, respectively: the first peak (0 V) is due to the electrosorption of glucose on NPG to form adsorbed intermediate, releasing one proton per glucose molecule, however intermediates are accumulated and occupied the active sites of the NPG surface and the current decreases as the number of scans increases. The second peak (0.32 V) is due to the direct oxidation of glucose by the active sites of NPG. Further increase of the potential results in the formation of gold oxide, which reduces the active sites for direct electro-oxidation of glucose and decreases the current signal. During the negative potential scan, the formed Au oxide is reduced, which made more active sites of NPG available for the direct oxidation of glucose resulting in an oxidation current peak at 0.37 V. To quantitatively study the effect of Pt addition to NPG, in Figure 38 the authors report the cyclic voltammograms of Pt-decorated NPG electrode with different, quantified, Pt amount and acquired in 0.1 M PBS solution (pH = 7.4) containing 50 mM glucose. In Figure 38A the cyclic voltammograms are acquired using positive scans (from −0.5 V to 0.6 V), in Figure 38B the cyclic voltammograms are acquired by negative scans (from 0.6 V to −0.5 V). The inset of (a) reports chronoamperograms for the electrooxidation of 10 mM glucose at +0.35 V at NPG (curve a), Au bulk disk (curve b), and NPG–Pt (24%) (curve c).

Figure 38. Cyclic voltammograms of Pt-decorated NPG electrode with different Pt amount and acquired in 0.1 M PBS solution (pH = 7.4) containing 50 mM glucose. In (**A**) the cyclic voltammograms are acquired using positive scans (from -0.5 V to 0.6 V), in (**B**) the cyclic voltammograms are acquired by negative scans (from 0.6 V to −0.5 V). The voltammograms are acquired with scan rate of 50 mV/s. The inset of (**A**) reports chronoamperograms for the electrooxidation of 10 mM glucose at +0.35 V at NPG (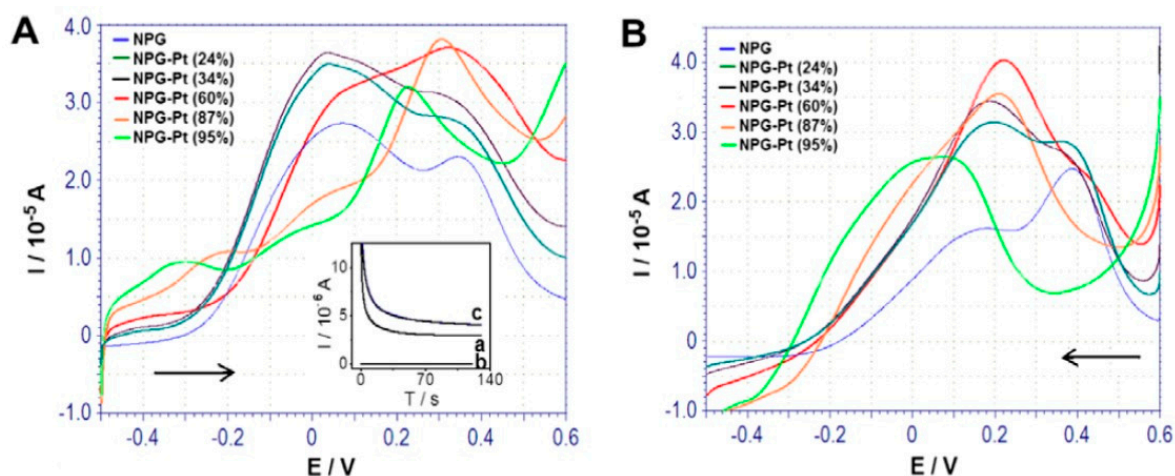curve a), Au bulk disk (curve b) and NPG–Pt (24%) (curve c). Reproduced with permission from [82]. Copyright Elsevier, 2010.

It can be recognozed that when the Pt coverage is ≤60%, the NPG–Pt electrode presents an improved electrocatalytic activity towards the oxidation of glucose indicated by the negatively shifted onset potential and the enhanced current signal. This is due to the electrocatalytic activity of Pt toward glucosa oxidation in addition to NPG (resulting in a synergistic effect on the oxidation of glucose). However, when the Pt coverage is >60% the current signal decreased (Figure 38B) indicating

a decreased electrocatalytic activity. This is explained by considering the morphology of Pt on the NPG surface by increasing the Pt amount, i.e., by increasing the Pt coverage: for small Pt amount (≤60%,), i.e., in the early stage, Pt forms an atomically thin layer, while for high Pt amount (>60%), three-dimensional Pt islands are formed (to minimize the total surface energy of the system). However, according to the authors, the Pt thin layer is more electrocatalytic active than Pt islands. The authors, in addition, confirmed the higher electrocatalytic activity of the Pt decorated NPG (24%) confirmed by chronoamperometric measurements (inset in Figure 38A). However, in order to verify practical applications of this sensor towards glucose sensing, itas performace was, also, tested under physiological conditions, in addition to alkline (or neutral or acidic) solution. Hence, the authors proceeded to analyze the NPG-Pt electrode amperometric response to glucose detection in neutral media miming physiological conditions, see Figure 39. As can be observed, both NPG (Figure 39A) and NPG–Pt (Figure 39B) electrodes respond quickly and sensitively to each addition of 1 mM glucose.
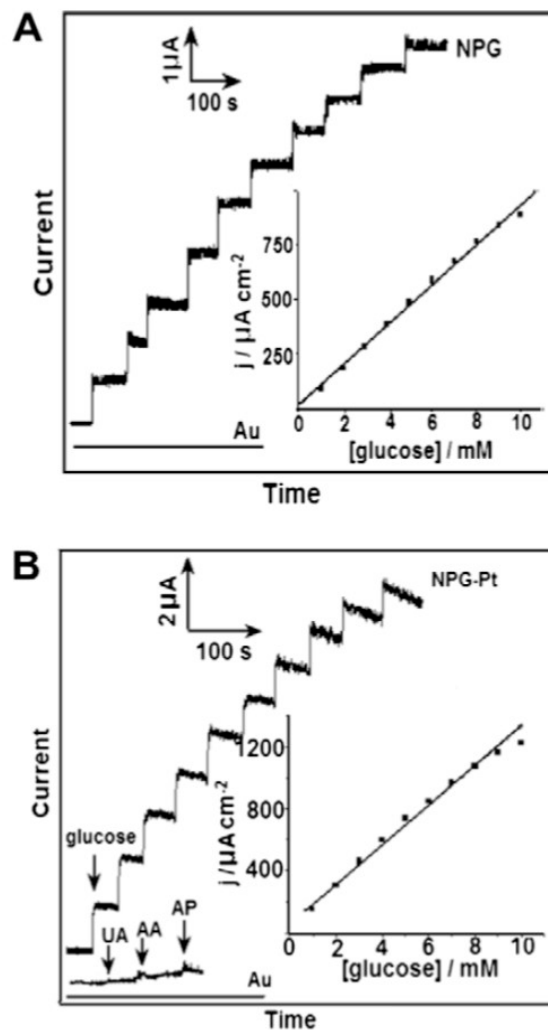

Figure 39. Current–time measurements obtained for (**A**) the NPG electrode (at +0.35 V) and (**B**) Pt-decorated NPG electrode (at +0.2 V) with successive addition of glucose (1 mM) or UA (0.02 mM), AA (0.1 mM), 4-acetamidophenol (AP) (0.1 mM). Electrolyte: 0.1 M pH 7.4 PBS containing 0.1 M KCl. The insets show the calibration curves for glucose at NPG and Pt-decorated NPG electrodes. Reproduced with permission from [82]. Copyright Elsevier, 2010.

The insets in Figure 39 show the linear dependence of the current signals on the concentration of glucose over the range of 0.5–10 mM for both NPG-based electrodes with a slope of 76.4 $\mu A/cm^2$ mM for NPG electrode and 145.7 $\mu A/cm^2$ mM for NPG–Pt electrode. In addition, the detection limit is derived as 1.0 μM for NPG electrode and 0.6 μM for NPG–Pt electrode. The authors verified, also,

the reproducibility of the electrodes by finding a relative standard deviation of 2.6% (NPG) and 3.0% (NPG–Pt) by controlling the current response for five replicate injections of 4.0 mM glucose. Finally, concerning the electrodes selectivity, the authors considered ascorbic acid (AA) (0.1 mM) 4-acetamidophenol (AP) (0.1 mM) and uric acid (UA) (0.02 mM) as interferents in the buffer solution, see Figure 39B: they have negligible interferences for the glucose detection. As already stated, this is due to the fact that electrochemical oxidation of the interfering species is a diffusion-controlled process whereas the electrochemical oxidation of glucose is a kinetic-controlled process. To conclude, in this work the authors found for glucose sensing that the NPG–Pt electrode show a linear range of 0.5–10 mM with a sensitivity of 145.7 $\mu A/cm^2$ mM and a detection limit of 0.6 μM. The sensor is highly reproducible, stable, and selective.

A further example is reported by Xiao et al. [84]: they investigated the nonenzymatic glucose sensing properties of NPG/ultrathin CuO film nanocomposite finding a great electrocatalytic activity towards glucose oxidation, a linear response to glucose up to 12 mM, a sensitivity of 374.0 $\mu A/cm^2$ mM, a detection limit of 2.8 μM, a strong tolerance against chloride poisoning and interference of ascorbic acid and uric acid. In this work, the authors used standard dealloyed NPG films and then developed a simple two-step electrodeposition approach to produce the NPG/CuO hybrid electrodes (see Figure 40A). In particular, Cu is electrodeposited on the NPG surface under a constant potential in $CuCl_2$ solution and then electrochemically oxidized into CuO via cyclic voltammetry in alkaline solution. Using microscopic techniques, the authors verified that the starting NPG preserves its original bicontinuous three-dimensional nanoporous morphology and a nanoscale-thick CuO film simply cover the NPG surface. Concerning the role of CuO, it is expected that the composites of NPG CuO film would present enhanced electrochemical activity, improved biocompatibility, and, in addtion, CuO should promote electron transfer.
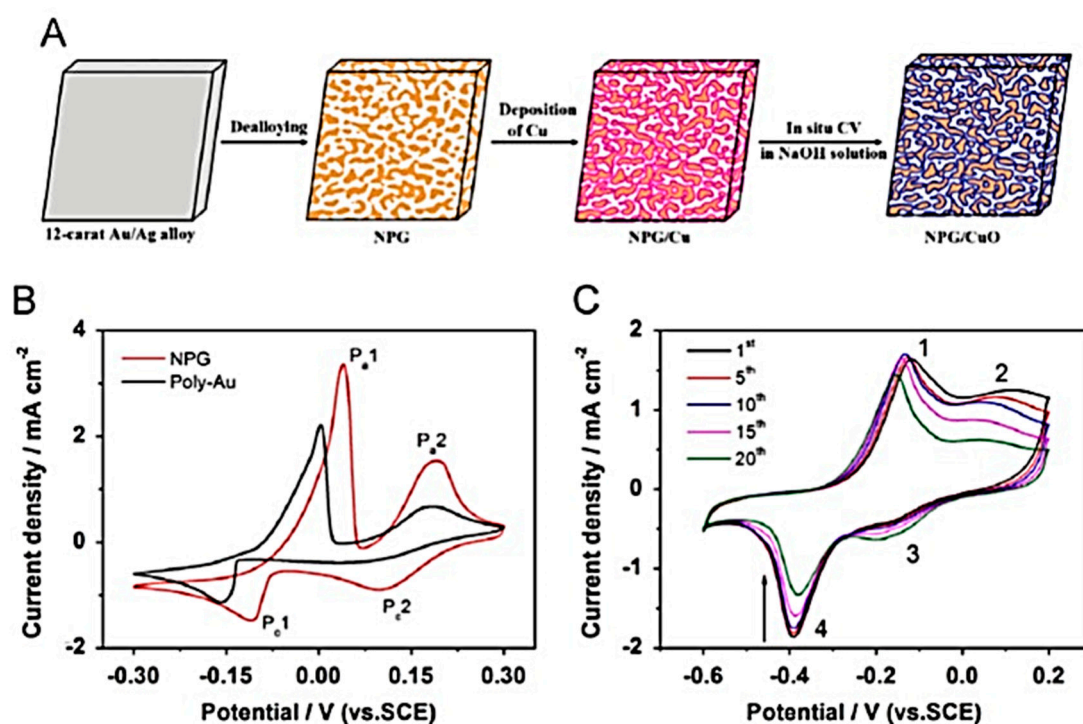

Figure 40. (**A**) Representative picture of the fabrication steps for the NPG/CuO composite electrode. (**B**) Cyclovoltammograms corresponding to the NPG electrode (red curve) and to poly Au (black curve) in 0.1 M KCl solution containing 10 mM $CuCl_2$ (scan rate 10 mV/s. (**C**) Cyclovlotammograms corresponding to NPG/Cu electrode in 0.1 M NaOH (scan rate 100 mV/s). Reproduced with permission from [84]. Copyright Elsevier, 2014.

The authors tested the NPG/CuO electrochemical properties by using it as the working electrode in a classical three-electrode cell with a Pt wire used as counter electrode, NPG/CuO working and a

saturated calomel reference electrode. Regarding the electrochemical deposition of Cu, Figure 40B reports cyclicvoltammograms acquired by using as working electrode NPG and bulk polycrystalline Au (poly-Au) in 10 mM $CuCl_2$ solution. For NPG, two pairs of redox peaks, namely P_a1/P_c1 and P_a2/P_c2, are observed and indicating two different deposition/stripping processes. In particular, the P_c1/P_a1 peak is the signature of the redox pair of freely Cu^{2+} and deposited Cu from the overpotential deposition (OPD). The P_c2/P_a2 peak is associated to the redox Cu underpotential deposition and stripping of Cu on the Au electrode. In NPG, these peaks are enhanced with respect to the same peaks observed in poly-Au electrode. In addition, Figure 40C shows the cyclic voltammograms of as-fabricated NPG/Cu in 0.1 M NaOH solution. In this case, two pairs of redox peaks can be recognized in the range from −0.6 V to 0.2 V, indicating a series in-situ redox transformations from Cu(0) to CuO. Peak named 1 and peak named 2 observed during the anodic scans are determined by the transition of $Cu(0)/Cu_2O$ and CuOH/CuO, respectively. Correspondingly, the peaks named 3 and 4 observed during the cathodic scan are due to the conversion of $CuO/Cu_2O(CuOH)$ and $Cu_2O(CuOH)/Cu(0)$, respectively. Changing the number of scans (Figure 40C), the potentials and process duration, the thickness of the grown CuO film can be adjusted to optimize, then, the system response signal to glucose. In this sense, the effects of deposition potential and deposition time on the response of the NPG/CuO system to 5 mM glucose in 0.1 M NaOH solution are reported in Figure 41A,B, respectively. The optimal potential and time, to maximize the current signal, is determined to be −0.2 V and 120s: in fact, a too low CuO amount causes the formation of CuO nanoclusters (instead of a continuous film) which have not enough electrocatalytic activity. On the other hand, a too thick CuO film decreases the capability of electron transfer during electrocatalysis. By microscopic analyses, the authors verified that the best conditions (−0.2 V and 120 s) result in 5 nm-thick CuO film evenly covering the NPG surface.
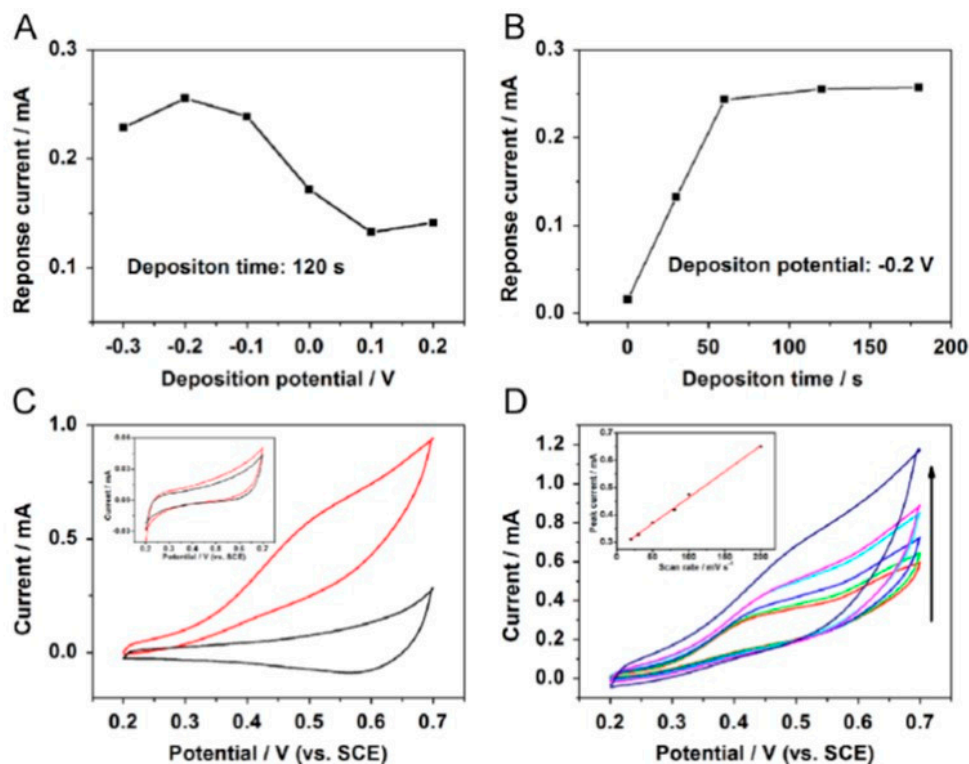

Figure 41. Plots elucidating (**A**) the effect of the deposition potential and (**B**) the effect of the deposition time on the response ofNPG/CuO electrode to 5 mM glucose. (**C**) Cyclic voltammograms acquired by using NPG electrode (inset), NPG/CuO electrode (scan rate 100mV/s) in 0.1 M NaOH in the absence (black curve) and presence (red curve) of 5 mM glucose. (**D**) Cyclic voltammograms acqired by using NPG/CuO electrode in 0.1 M NaOH containing 5 mM glucose at different scan rate from 20 to 200 mV/s. Inset reports the anodic peak current as a function of the scan rate. Reproduced with permission from [84]. Copyright Elsevier, 2014.

The response of the NPG and NPG/CuO electrode towards glucose sensing is evaluated by the cyclic voltammograms reported in Figure 41C, acquired with the electrode in 0.1 M NaOH solution with presence of 5 mM glucose (potential range from 0.2 V to o.7 V, scan rate 100 mV/s): In a blank solution, neither the bare NPG nor NPG/CuO systems present oxidation peaks. However, after the addition of glucose, the NPG/CuO electrode shows strong activity in the oxidation of glucose with an initial potential of ~0.25 V and a broad peak at ~0.45 V. In contrast, after the addition of glucose, the pure NPG electrode shows lower current signals. The involved reactions can be summarized, in sequence, as: $CuO+H_2O+2OH^-\rightarrow Cu(OH)_4^-+e^-$, $Cu(III)+Glucose+e^-\rightarrow Gluconolactone+Cu(II)$, $Gluconolactone\rightarrow Gluconic$ acid (hydrolysis). Futhrmore, Figure 41D reports the cyclic voltammograms acquired by using the NPG/CuO electrode in 5 mM glucose solution and changing the scan rate, so to study more specifically the oxidation process: by increasing the scan rate, the anodic peak current increases linearly and the anodic peak potential shifts positively, indicating that the electro-oxidation of glucose on NPG/CuO is a surface adsorption/selectivity and diffusion controlled process. Finally, Figure 42 reports the studies concerning the amperometric response of the NPG/CuO electrode.
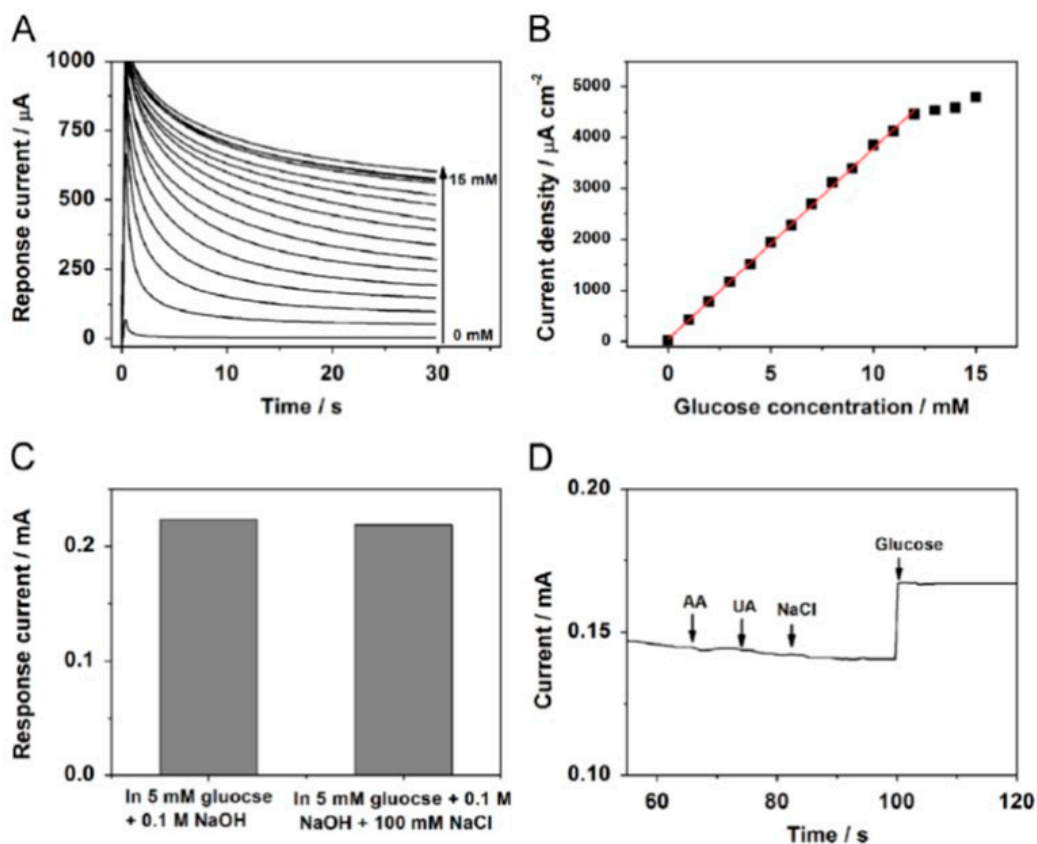

Figure 42. (**A**) Chronoamperometry plot of NPG/CuO electrode with various glucose concentrations in 0.1M NaOH solution at 0.4V. (**B**) Calibration plot of the NPG/CuO electrode. (**C**) Responses of the electrode to 5mM glucose in 0.1 M NaOH solution with and without 100 mM NaCl. (**D**) Responses of the electrode in 0.1 M NaOH with the successive addition of 0.1 mM AA, 0.1 mM UA, 1 mM NaCl, and 3 mM glucose. Reproduced with permission from [84]. Copyright Elsevier, 2014.

Concerning these analyses, 0.4 V is chosen as the constant detecting potential to investigate the glucose sensor response, since this potential is relatively low to avoid interference from other possible electroactive elements. Figure 42A shows the amperometric response of the NPG/CuO electrode at the constant potential to successive additions of 1 mM glucose in 0.1 M NaOH solution. The NPG/CuO electrode responds to any glucose addition by plateau current ignal linearly increasing along with glucose concentration increment, followed by steady-state reached within 10 s. The corresponding calibration curve reported in Figure 42B allows to evaluate the electrode sensitivity in

374.0 mA/cm² mM. The upper of the linear range is 12mM and the limit of detection is 2.8 μM. Such high sensitivity and wide linear range are attributed to the unique bicontinuous nanoporous structure of NPG, which significantly enhances the diffusion of glucose and to the electroactivity of the ultrathin CuO film.

4. Perspectives and Challenges

The future of the use of NPG in advanced sensing applications relies on the possibility to further push the material sensitivity towards more strict limits. In order to reach this goal, recently, NPG nanostructures are investigated replacing NPG leafs or films. In fact, the surface area of NPG leafs or films is of the order of 10 m²/g while NPG nanostructures as nanoparticles or nanowires are characterized by surface area of the order of 10^4–10^5 m²/g (and innovative particles porosity characterization approaches are, often, required [109]): this enormous enhancement of the surface area makes the material more reactive to analytes and, so, more sensitive to smaller amounts of the analytes. In this sense, recently, several efforts were made to obtain complex NPG nanoscale architectures and on the characterization of their optical and electrochemical properties so as to produce innovative materials which could find forefront applications in the ultra-sensitive detection of analytes. In this section, we discuss some of these works.

Vidal et al. [99] produced NPG nanoparticles (namely, "nanosponges") and investigated their plasmonic properties. The authors fabricated AuAg alloy nanoparticles by solid-state thermal-induced alloying and dewetting of deposited Au/Ag bilayers [30,96–99]. Then, these nanoparticles were dealloyed in HNO_3 so to remove the Ag atoms from the nanoparticles. Hence, NPG nanoparticles are obtained [30,96–99]. In addition, the authors transferred the NPG nanoparticles on an indium tin oxide covered glass slide so to perform both scanning electron microscopy imaging and scattering and photoluminescence (PL) spectra acquisition from one and the same individual nanoparticle in a darkfield/fluorescence confocal configuration. As an example, Figure 43 reports, in this setup, the plan view (in (a)) and cross-sectional (in (b), after focused-ion-beam cutting) scanning electron microscopy images of a NPG nanoparticle, and the corresponding photoluminescence (PL) spectra (in (c)). As can be seen, the major spectral weight of PL is in the range between 500 and 800 nm. Concerning the resolution of the electron microscopy scans performed on the cross-section of the particles, we mention that this resolution is, surely, affected by the low amount of probed material. However, this resolution is typically lower than 10 nm and in the best condition can also reach ~1 nm [110]. The particles cross-sectional estimated pores size is, hence, reliable when compared to the technique resolution.
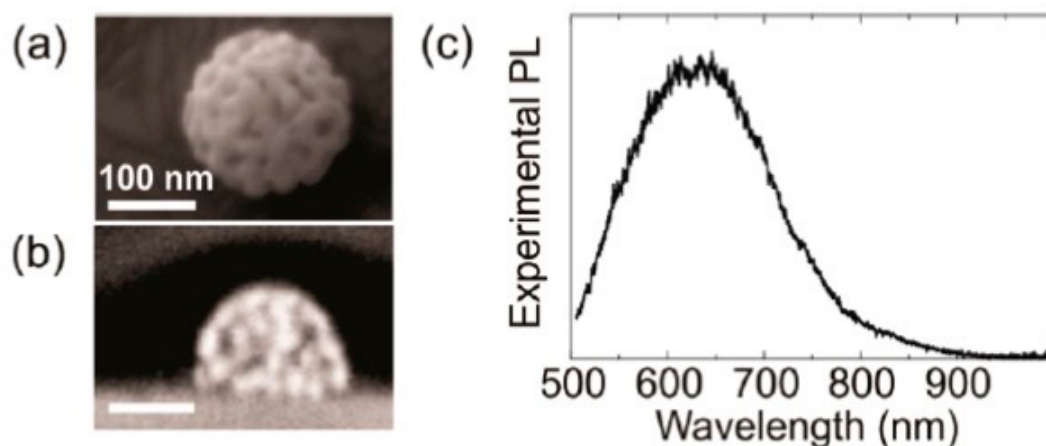

Figure 43. (**a**) Plan view and (**b**) cross-sectional (after focused-ion-beam cutting) scanning electron microscopy images of an NPG nanoparticle. (**c**) Photoluminescence (PL) spectra corresponding to an NPG nanoparticle. Reproduced with permission from [99]. Copyright American Chemical Society, 2018.

Figure 44 reports reports the polarized scattering spectra and the corresponding scanning electron micrographs of 3 single NPG nanoparticles, two with an almost spherical shape and diameters of 115 nm and 155 nm, and one NPG nanoparticles with an half-spherical shape having a long axis of 410 nm and a short axis of 195 nm. The scattering spectra are acquired changing the polarization of the incident light and, correspindently, these spectra show a strong polarization dependence even for the spherical Au nanosponges, due to their highly nanoporous (i.e., inhomogeneous) structure.
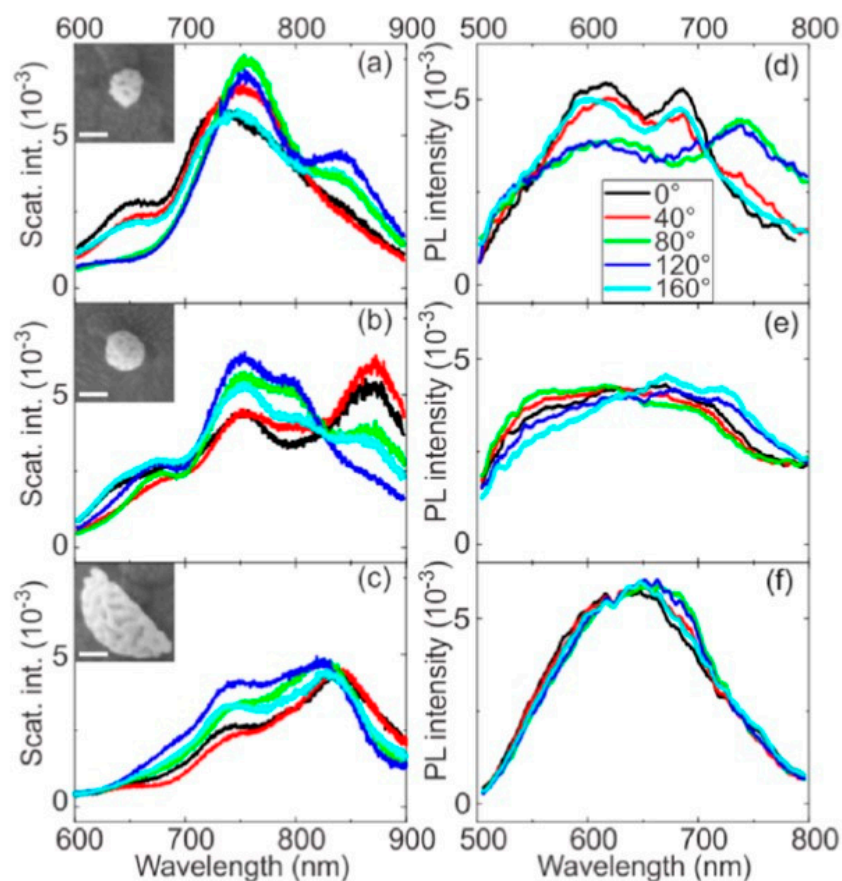

Figure 44. Plan-view scanning electron microscopy images (scale bars 100 nm) of NPG nanoparticles and corresponding polarization dependent scattering and photoluminescence (PL) spectra (**d**–**f**): (**a**,**b**) two almost spherical NPG nanoparticles with diameters of 115 and 155 nm, respectively; (**c**) half-spherical NPG nanoparticles characterized by lateral dimensions of 410 and 195 nm. (**d**–**f**) In each plot, the different coloured spectra correspond to the polarization of the incident light. Reproduced with permission from [99]. Copyright American Chemical Society, 2018.

Figure 44d–f reports the corresponding polarization-dependent PL spectra, and draws the following conclusions: in the case of the smallest Au NPG nanoparticle, the polarization dependence of the PL spectra (Figure 44d) is strongly affected by the polarization dependence of the scattering spectra (Figure 44a). In stark contrast, the PL of the larger, 155 nm NPG nanoparticle (Figure 44e) is much less affected by polarization, while its scattering spectra (Figure 44b) show quite strong polarization dependence. So, when the size of the NPG nanoparticles increases, the strong influence of the system nanoporous structure is much less pronounced (tending to vanish) and it responds as a homogeneous effective medium in the sense that the substructure of the components (pores and ligaments sizes) is small compared to the wavelength and, also, that the size of the medium itself is at least on the scale of the wavelength. However, the PL anisotropy ceases much more quickly with increasing size. For most of the Au nanosponges larger than 120 nm, the polarization anisotropy of the scattering spectra is larger than the polarization anisotropy of the PL. Only NPG nanoparticles

smaller than 120 nm in diameter show large PL polarization anisotropy. The polarization dependence of light scattering from NPG nanoparticles is due to their individual interior percolation (nanoporous structure), which causes a unique pattern of hot-spots throughout the nanoparticles. Correspondently, the PL from the NPG nanoparticle is affected by localized plasmons. To better investigate these aspects, the authors performed electric field simulations by finite difference time-domain calculations and the main results are reported in Figure 45. Regarding the calculations, these were performed by considering the NPG nanoparticles on ITO substrate as half-spheres, perforated by randomly distributed air spheres, allowed to overlap by 20% in all directions. This permits the formation of intertwined air filaments and hence adequately imitates the 3D Au−air percolation of the nanoparticles. White light excitation was modeled by an external incoming plane wave (blue arrow in Figure 45a), while an electron−hole recombination was modeled by an internal electric dipole source (blue double arrow in Figure 45b). In both cases, a temporally defined excitation with a Gaussian envelope of 3.3 fs full width half-maximum is considered.
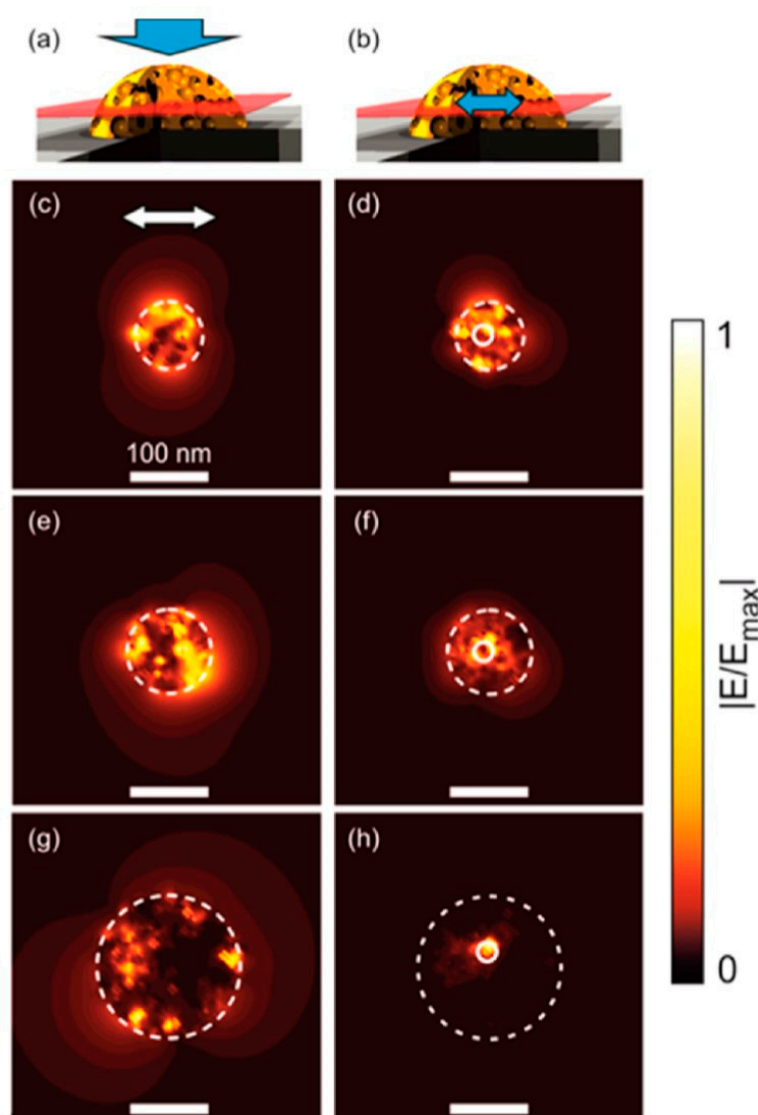

Figure 45. Distribution (numerical calculations) of the electric field (E) through a cross-section (red plane) inside NPG nanoparticles. In particular, the NPG nanoparticles, in the calculations, are excited by an external plane wave ((**a**), left column) or by an inside dipole ((**b**), right column). For the calculations, the following diameters for the NPG nanoparticls are assumed: (**c,d**) 90 nm, (**e,f**) 115 nm, (**g,h**) 195 nm. In addition, (**c,e,g**) show lane wave excitation, (**d,f,h**) show inside point dipole excitation. The dipole positions are indicated by small white circles. Reproduced with permission from [99]. Copyright American Chemical Society, 2018.

The absolute value of the total electric fields within 3 NPG nanoparticles is reported considering, respectively, nanoparticles with diameter of 90 nm, 115 nm, and 195 nm and an external plane wave irradiation (left column, Figure 45c,e,g) or an excitation by an internal dipole (right column, Figure 45d,f,h). The fields are determined in the planes where the dipole is located (red planes in Figure 45a,b). All images are acquired 10 fs after the peak of the excitation, so that only the scattered fields are shown (without the incident field). Figure 45c,d shows the distribution of the excited plasmonic hot-spots inside the small (90 nm) NPG nanoparticle for plane wave and for internal excitation, respectively. In both cases, hot-spots throughout the whole volume of the nanosponge are excited in a similar way. The situation is different in the case of the 115 nm NPG nanoparticle: while the plane wave from outside again excites a pattern of hot-spots throughout the nanoparticle (Figure 45e), the local dipole emitter cannot excite all the hot-spots anymore (Figure 45f). In the case of the largest NPG nanoparticle, the failure to excite hot-spots with a local dipole throughout the nanoparticle is even more pronounced (see Figure 45g,h). Apparently, and in contrast to plane wave excitation, a plasmonic horizon of about 57 nm is generatred via local excitation from inside the nanoparticle. Qualitatively, regarding small NPG nanoparticles, there is only a limited number of anisotropic modes, extending over the whole nanoparticle. Both a plane wave from outside and a local inside dipole excite similar modes (Figure 45c,d), and, consequently, scattering and PL anisotropies are high. For large NPG nanoparticles, there are many more anisotropic modes that do not span the whole NPG nanoparticle when excited from a local, inside dipole (Figure 45f,h). The PL, arising from the modes of restricted volume, shows a significant polarization dependence, however, modes localized elsewhere in a large nanoparticles, excited by a subsequent electron–hole recombination outside the coherence volume of the previous event, show a different polarization pattern resulting in unpolarized PL. The key information which can be drawn is that a localized plasmon has been created by a local electron–hole recombination event and it can propagate to coherently excite neighboring hot-spots only within the lifetime of the plasmon. This limited lifetime, together with a finite speed with which the information can travel, results in a plasmonic horizon. Considering a mean lifetime of 6.3 fs (for 115 nm NPG nanoparticle) and an event horizon of 57 nm, an information propagation velocity $v = 9.0 \times 10^6$ m/s is evaluated. This velocity is about 6 times larger than the Fermi velocity of sp-electrons in bulk Au (1.4×10^6 m/s). These results are fundamentals towards the understanding of behaviour of NPG nanoparticles when used as plasmonic-based sensors because the holes percolate throughout the NPG nanoparticles, and hence organic molecules may access the hot-spots easily. In this sense, for example, Santos et al. [94] used NPG nanodisks as label-free plasmonic biosensor for ERBB2 cancer gene DNA target based on the distance-dependent detection of surface-enhanced fluorescence, achieving an impressive detection of 2.4 zeptomole of DNA target with an upper concentration detection limit of 1 nM. The plasmon resonance associated with the nano-disk shape of NPG promotes effective light coupling and determines higher field enhancement compared to that in NPG films, and the high-density of hot-spots in NPG nanostructures allows to reach the very high level of sensitivity. In this work, the NPG nanodisks were fabricated by firstly depositing a 120 nm-thick film of alloy $Au_{30}Ag_{70}$ on glass substrate. Then, a 600 nm-thick layer of of polystyrene beads was deposited on the surface of the metallic alloy film. Plasma etching was, then, used to shrink and isolate each polystyrene bead and, after this step, Ar plasma etching was employed to induce the alloy nanodisks formation on the glass surface. Finally, the remaining polystyrene beads were removed by means of sonication in chloroform. As a final step, the AuAg alloy nanodisks were dealloyed in HNO_3, resulting in the formation of NPG nanodisks with diameter of 400 nm, thickness of 75 nm, and mean pores size of 13 nm. Figure 46 presents the scheme of the hairpin probe and probe-target (dsDNA) configurations of the ERBB2 cancer gene and their immobilization on the surface of the NPG nanodisks. The hairpin probe sequence is complementary to the ERBB2 oncogene, a target breast cancer DNA biomarker. The authors used fluorescence measurements to investigate the sensing properties of the NPG nanodisks. In this scheme, hairpin ssDNA (single-stranded DNA) probe is employed to detect ERBB2. The probe features a Cy3 on the 3'-end and a sulfur (S) on the 5'end that allows the binding to the Au surface. When fluorophores are near metal surfaces, electronic energy transfer from the molecule may occur which generally leads to

fluorescence quenching. However, the peculiar plasmonic properties of the NPG nanpdisks play a key role in this process. In particular, if the probe alone is bonded, the Cy3 molecule is positioned at the close proximity of the NPG nanodisk surface, which promotes quenching. In contrast, a hybridized dsDNA (double-stranded DNA) has the Cy3 molecule on the opposite end of the S and far away from the NPG nanodisksurface after binding. Such conformation induced modulation of plasmonic enhancement is at the basis of the plasmonic-enhanced fluorescence mechanism.
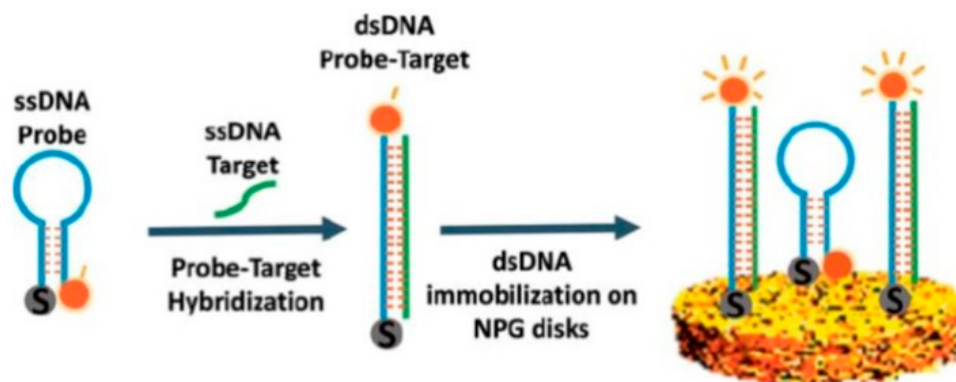

Figure 46. Picture of the hairpin probe and probe-target (dsDNA) configurations of the ERBB2 cancer gene, and their immobilization on NPG nanodisks. In the figure ssDNA is single-stranded DNA, dsDNA is double-stranded DNA. Reproduced with permission from [94]. Copyright Wiley-VCH, 2015.

On the basis of these premises, the authors mixed different amounts (0–5 μL) of the ssDNA target sequence (40 nM) and hybridized with a fixed amount of hairpin probe (5 μL, 40 nM). Then they added phosphate buffer solution (PBS) to a total 10 μL volume and the resulting concentrations of hybridized dsDNA were fixed in 6 couples: (0; 20) nM, (4; 20) nM, (8; 20) nM, (12; 20) nM, (16; 20) nM, (20; 20) nM. 5 μL of each solution was dispersed on the glass substrate with on top the NPG nanodisks and (after incubation), the fluorescence spectra were recorded, as reported in Figure 47A.
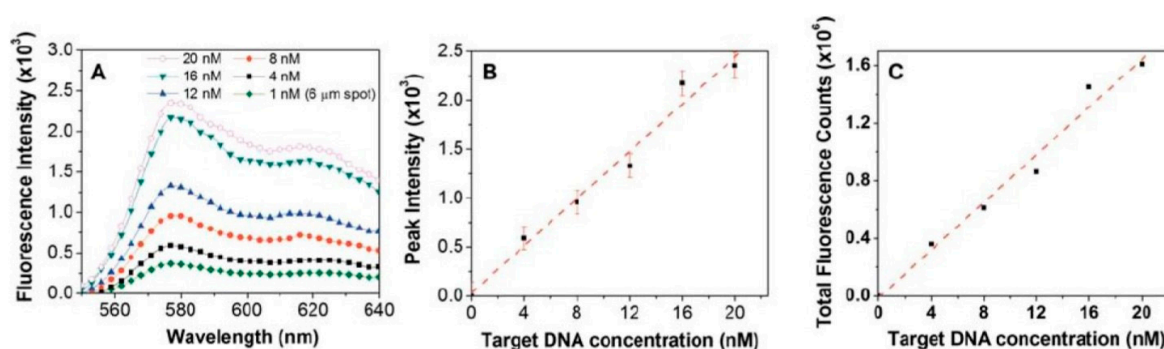

Figure 47. (**A**) Fluorescence spectra of the NPG nanodisks with the proble signal used as reference baseline and the different spectra correspond to different target DNA concentration (as indicated in the label). (**B**) Plot of the evolution of the fluorescence peak intensity versus the target DNA concentration. (**C**) Plot of the evolution of the total fluorescence conts versus the target DNA concentration Reproduced with permission from [94]. Copyright Wiley-VCH, 2015.

Figure 47A indicates an increase of the fluorescence intensity as the target concentration increases. Hence, Figure 47B,C report, respectively, the peak fluorescence intensity and the total fluorescence counts versus the target concentration indicating a linear response over all the investigated range of concentration. By using these plots, the authors estimate the amount of detectable dsDNA molecules in about 2.4 zeptomole for a signal-to-noise ratio of about 123 and, in principle, an ultimate limit of detection 0f about 0.06 zeptomole for a signal-to-noise ratio of 3. Such

an enhancement of sensitivity with respect to standard methods is attributed to the near-field effect of localized surface plasmon resonance typical of NPG, however in combination with the enormous surface area of NPG nanodisks and the higher density of internal hot-spots in NPG nanostructures with respect to NPG films (i.e., higher field enhancement within the high density plasmonic hot-spots).

As already discussed for NPG films and foils, also for NPG particles we mention that the pores size and population can be correlated to corrosion of the particles. This is connected to the mechanical properties of the NPG particles. In this regard, Khristosov et al. [111] investigated the mechanical properties of NPG particles, by means of nanoindentation, before and after annealing processes. For smaller ligament sizes, hardness increased with annealing temperature up to 300 °C and then strongly decreased. For larger ligament sizes, hardness decreased with increasing annealing temperature. Young's modulus was unchanged up to 300 °C. The NPG particles hardness behaviour suggests a dependence of the pores size and population on the corrosion characteristics of the particles. However, also, in the case of the dealloying process of AuAg alloy particles in order to produce NPG particles, a volume shrinkage (~39%) of the particles was observed [30] and ascribed, as in the case of NPG films and foils, to the creation of a large number of lattice defects and by local plastic deformation.

To complete the overview regarding optical-sensing by complex-morphology NPG, we discuss the work by Zhang et al. [73] concerning the use of wrinkled NPG films for ultrahigh-sensitivity SERS measurements by using the high density of hot-spots (nanogaps and sharp nanotips) in complex-morphology NPG leading to enormous enhancement in the electromagnetic field. In this work, the authors prepared wrinkled NPG films by thermal contraction of NPG/PS (polystyrene) composites: in particular, as pictured in Figure 48, three 100 nm thick NPG films with pores sizes of 12 nm, 26 nm, and 38 nm were fabricated by dealloying $Au_{35}Ag_{65}$ (at.%) alloy leafs in HNO_3 at room temperature for 600, 3600, and 21,600 s, respectively. The as-fabricated NPG films with an area of 2 cm × 2 cm were physically attached to the prestrained PS and heated at 80 °C for 3600 s to strengthen the bonding between NPG and PS. Finally, the NPG/PS composites were heated at 160 °C for 360 s.
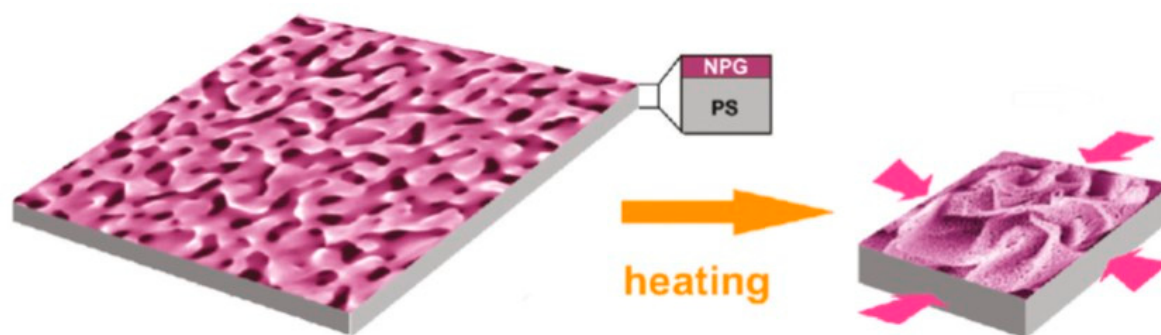

Figure 48. Schematic picture of the wrinkled NPG film obtained by thermal contraction of a prestrained polymer sheet. Reproduced with permission from [73]. Copyright American Chemical Society, 2011.

The prestrained PS is an amorphous polymer which shrinks when heating up to a temperature above its glass transition point (95 °C). So, the 160 °C thermal process leads to more than half volume shrinking of the PS determining a contraction of the NPG films and imposong to the NPG films a superstructure made of sharp nanotips. Crystal violet (CV) and Rhodamine 6G (R6G) in methanol solutions were used as probe molecules for SERS measurements (incident wavelength of 514.5 nm and 632.8 nm) was used in the Raman study. Figure 49a–c reports plan-view scanning electron microscopy images of the as-dealloyed NPG films increasing the etching time, so increasing the average pores size from 12 nm, to 26 nm and to 38 nm, passing from (a) to (b) and to (c). The low magnification image in Figure 49d shows as an example that the as-prepared NPG film is flat on a micrometer scale. After annealing at 160 °C for 360 s, the shrinking of the PS substrate leads to the formation of a wrinkled NPG film, Figure 49e, giving place to a two-levels complex morphology

characterized on a high level by sharp tips and on a low level by the standard bicontinous three-dimensional morphology of the NPG. The distribution of the wrinkles is uniform across the entire film with a biaxial periodicity (about 35 μm along the primary wrinkle direction and about 2030 μm along the secondary direction). The biaxial wrinkling gives rise to rose-petal-shape 3D nanostructure as reported in the zoom-in scanning electron microscopy images in Figure 49f–h. The annealing process detrmining the formation of the wrinkled structure does not affect the NPG nanoporosity feature and the length scale of the wrinkles appears to be solely controlled by the contraction ratios but independent of nanopore sizes, since it is identical in the three samples. Higher resolution structural analyses were performed by using scanning transmission electron microscopy imaging, see Figure 50, revealing the formation of ridge cracks with width ranging from smaller than one nanometer to tens of nanometers, which forms various nanogaps edged with fractured Au ligaments (Figure 50d,e). These analyses allow to recognize the presence of broken ligaments having apexes less than 5 nm in diameter, which is much smaller than the original ligaments of the as-prepared sample. Deformation defects, such as deformation twins and stacking faults, can be frequently observed in the ligament, indicating that the formation of the sharp tips is associated with the localized plastic deformation of Au ligament during breaking.
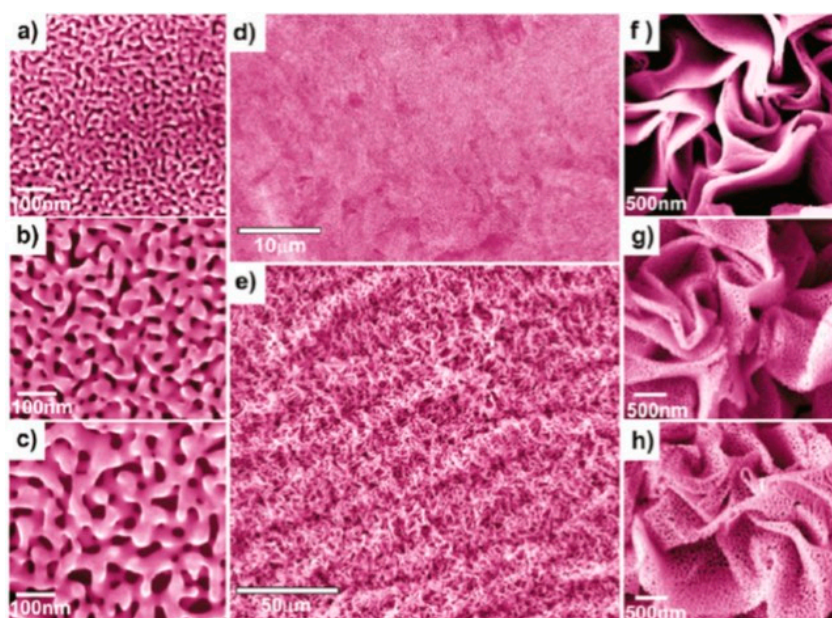

Figure 49. Scanning electron microscopy images of: (**a–c**) as-produced NPG films with pores sizes of 12 nm (**a**), 26 nm (**b**), 38nm (**c**); (**d**) as-produced NPG film with pores size of 38 nm (lower magnification) showing the large-area flat morphology; (**e**) wrinkled NPG film with pores size of 38 nm; (**f–h**) wrinkled NPG films (higher magnifications) with pores sizes of 12 nm (**f**), 26 nm (**g**), 38 nm (**h**) showing the local morphology. Reproduced with permission from [73]. Copyright American Chemical Society, 2011.

A submonolayer of CV molecules were adsorbed on the wrinkled NPG surface by immersion of the wrinkled NPG substrates in 10^{-8} M CV solution for 120 min, and then the SERS spectra were acquired. The laser beam size for the Raman measurements is set as large as 5 μm in diameter to acquire averaged SERS spectra. As presented in Figure 51a, the wrinkling structure causesa clear improvement in the SERS enhancements of the three samples in comparison with the flat NPG films. The enhancements show strong dependence on the pores size, and the wrinkled NPG with the pores size of 26 nm has the highest enhancement, about 60-fold higher than that of the as-prepared NPG. On the other hand, the Raman intensity of the wrinkled NPG films with pores sizes of 12 nm and 38 nm are about 20-fold and 50-fold stronger than those of the corresponding flat NPG films. Although the SERS enhancement of as-prepared NPG increases by decreasing the pores sizes, and the sample with the smallest pore size of 12 nm possesses the highest SERS enhancement among the three as-

prepared samples, the strongest SERS enhancement of the wrinkled samples is observed from the one with a pore size of 26 nm (Figure 51b) indicating that the microstructure changes determined by wrinkling play an dominant role in the improved SERS effect. The authors, then, used a small laser beam size of 1 μm in diameter, in order to investigate the SERS inhomogeneity of the wrinkled NPG films by acquiring the Raman signals from different sites.
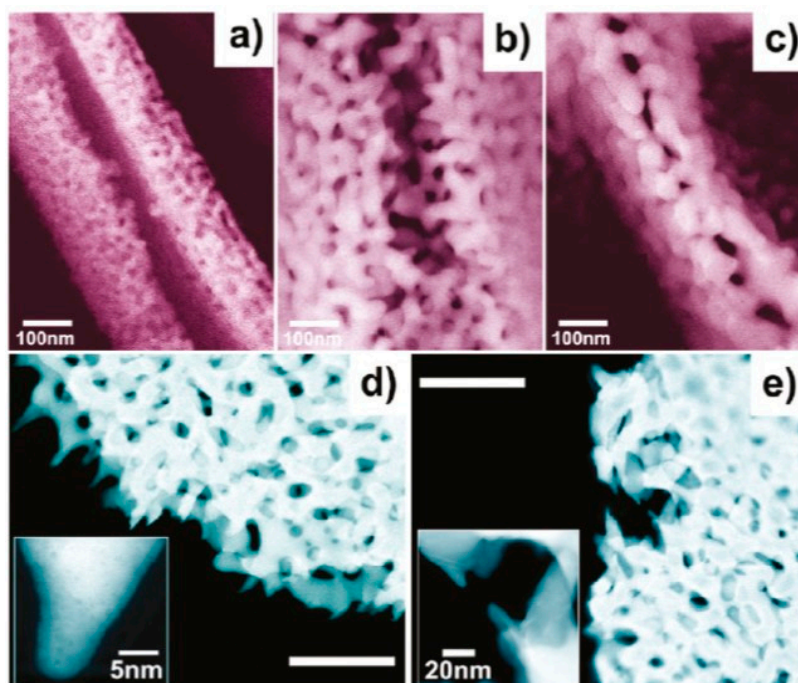

Figure 50. Scanning electron microscopy (**a**–**c**) and scanning transmission electron microscopy (**d**,**e**) of wrinkled NPG films. (**a**–**c**) The ridges of the wrinkled NPG with the pores size of 12 nm (**a**), 26 nm (**b**) and 38 nm (**c**) imaged by scanning electron microscopy. (**d**,**e**) Scanning transmission electron microscopy images of the fractured ridges of the wrinkled NPG with pores size of 26 nm. The inserts of panel (**d**,**e**) show individual sharp nanotips. The scale bars shown in panels (**d**,**e**) are 200 nm. Reproduced with permission from [73]. Copyright American Chemical Society, 2011.

So, scanning the beam along a wrinkle ridge, they found that the Raman intensity also changes dramatically from site to site and the enhancements corresponding to sites identified as hot spots are more than ten times stronger than those of the weakest ones at the ridges (Figure 51c,d). The enhancement factor (EF) of the wrinkled NPG film with the nanopore size of 26 nm is measured, also, by using R6G molecules adsorbed on the wrinkled NPG surface, Figure 51d. authors calculated the EF by comparing the intensity of the single molecule from the surface-enhanced resonance Raman scattering (SERRS) signal with that from the RRS signal by the formula EF = (I_{SERRS}/N_{SERRS})/(I_{RRS}/N_{RRS}) being N_{RRS} the number of probe molecules contributing to the bulk Raman signal, N_{SERRS} the number of probe molecules contributing to the SERRS signal, and I_{SERRS} and I_{RRS} the intensities of the selected scattering bands in the SERRS and resonance Raman spectra, respectively. On the basis of these calculations, the authors estimated the average EF of the winkled NPG films as 0.7×10^8, much higher than that of the as-prepared original NPG films, for which 10^6. In addition, since the magnitude of the intensity at the best enhanced sites is more than 10 times larger than that at the weak enhanced sites, as reported in Figure 51c,d, the local EF at the "hot spots" is approximately larger than 10^9, approaching the requirement for single molecule detection.
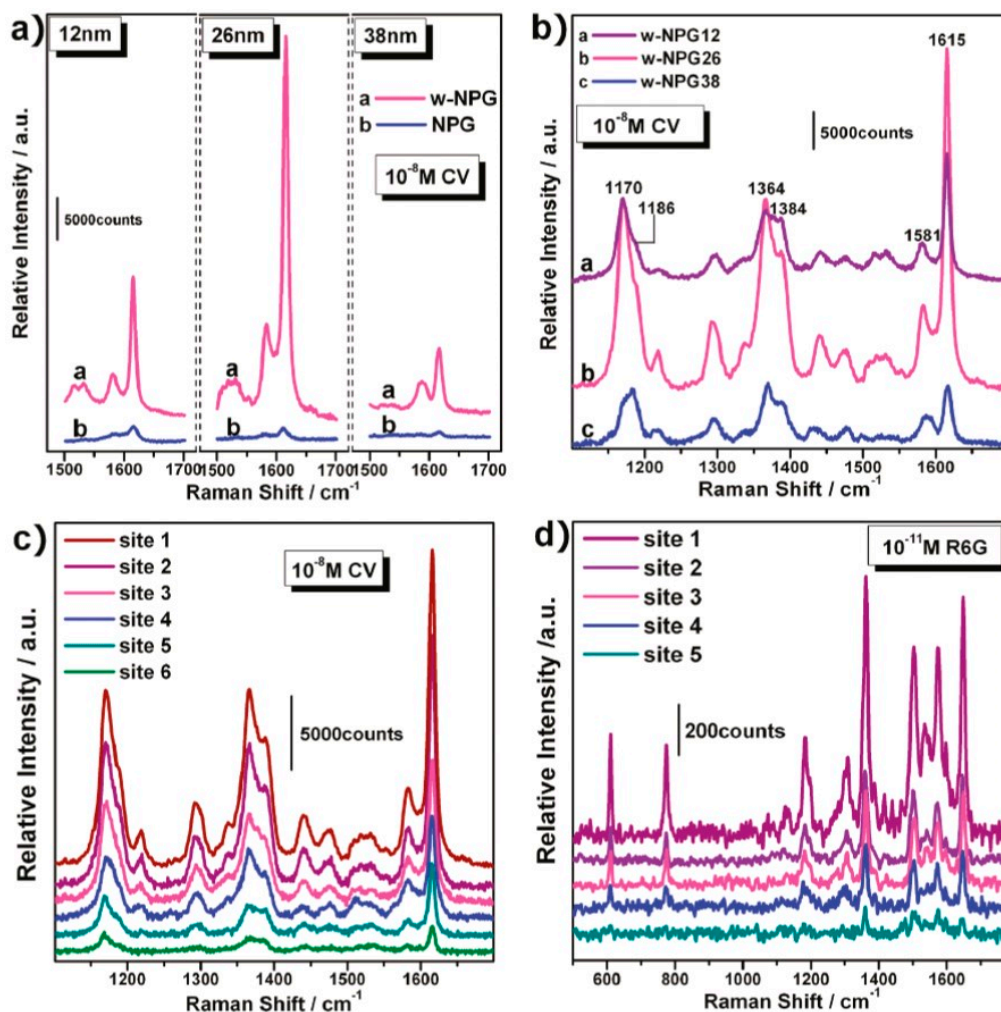
Figure 51. SERS spectra of Crystal Violet (CV) and Rhodamyne (R6G) molecules on wrinkled NPG films. (**a**) Comparison of SERS intensity between wrinkled and as-produced NPG films with different pores size. (**b**) SERS spectra from wrinkled NPG with different pores size of 12 nm (w-NPG12), 26 nm (w-NPG26), and 38 nm (w-NPG38). (**c**) Variation of SERS spectra of CV on w-NPG26 at different sites along a wrinkle ridge. (**d**) Variation of SERS spectra of R6G on w-NPG26 at different sites along a wrinkle ridge. The excitation wavelength is 632.8 nm for CV and 514.5 nm for R6G. Reproduced with permission from [73]. Copyright American Chemical Society, 2011.

　　　　Concerning the enhancement mechanisms of the wrinkled NPG films, the authors observe that the SERS band shift observed in this study is very small when compared with that in the FT-Raman spectra reported in literature, hence indicating that the chemical interaction between CV molecules and the wrinkled NPG substrates is very weak. Therefore, they conclude that the chemical effect is not the main cause of the SERS enhancement. They conclude, instead, that the significant enhancements are achieved from the nanosized Au ligaments and pores, in combination with the strong effect on the electromagnetic field as determined by the "hot-spots" at nanogaps and sharp nanotips have imposed by the wrinkled structure. In particular, the ductile cracking of the 26 nm-pores NPG films, different from the brittle failure of the 12 nm NPG, produces a large number of microcracks with various gap widths, which can generate plenty of "hot spots" by the local optical coupling with suitable gap width. Moreover, the sharp nanotips of the broken ligaments can also provide strongly localized electromagnetic fields for ultrahigh SERS enhancements because of the additional lightning rod effect.

　　　　To conclude, we discuss an example of the use of NPG nanostructures as amperometric sensor. In particular, Liu and Searson [92] fabricated single NPG nanowires and verified that its resistance

changes upon adsorption of octadecanethiol and its concentration can be related to the resistance changes so to obtain an amperometric sensor with sensitivity factor of 1.0×10^{-16} cm^2 which is comparable to values reported for adsorption at ultrathin films. The authors fabricated $Au_{0.18}Ag_{82}$ alloy nanowires (15–20 μm in length, 360 nm in diameter) by electrochemical template synthesis. The nanomires were removed from the substrate on which they were grown and dispersed in a solution. From the solution, the nanowires were then dispersed on an insulating substrate and contact electrodes were patterned so to have nanowires contacted from both sides, see Figure 52. In this way, it was possible to electrically contact single nanowire from single nanowire electrical measurements. The length of the nanowires between the contacts was typically 5–8 m. Finally, Ag was removed from the nanowire, by HNO$_3$ dealloying, so to obtain NPG nanowires ready for electrical testing. Figure 52 shows the chip carrier (a), the lead pattern (b), and a single nanowire (c). The measured resistance of single nanowire (length = 5–8 μm) $Au_{0.18}Ag_{0.82}$ (reference sample) 10–50 Ω (see baseline in Figure 53a). Upon addition of HNO$_3$ the resistance of the nanowire increases with the etching time, as reported in Figure 53a. Specifically, upon addition of HNO$_3$, the resistance of the nanowire increases by a few ohms within the first minute; then, it remains about constant for 4–5 min, after which it increases dramatically. The etching was stopped when the resistance was in the range of 100–500 Ω by rinsing with water. If etching was allowed to continue further, the resistance continues to increase, and eventually the nanowire breaks. Figure 53b reports an experiment where a Au nanowire is exposed to HNO$_3$, indicating no change in resistance. However, the HNO$_3$ etching, by removing the Ag atoms, also causes a modification of the nanowire diameter and porosity with the etching time.
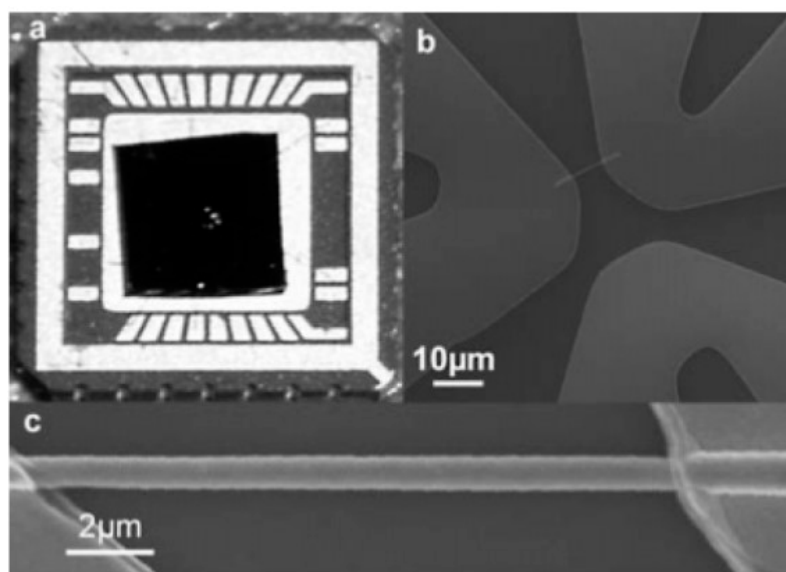

Figure 52. (**a**) Optical microscope image of a chip carrier with a single nanowire device, (**b**) plan view scanning electron microscopy micrograph of a single nanowire showing the Au pads photolitographically patterned, (**c**) plan view scanning electron microscopy micrograph of an NPG nanowire. Reproduced with permission from [92]. Copyright American Chemical Society, 2006.

Figure 54a reports a cross-section scanning electron microscopy micrograph (acquired after cutting the nanowire by focused ion beam) of a $Au_{0.18}Ag_{0.82}$ alloy nanowire allowing to recognize it as a solid (i.e., without internal empties) cilinder of diamter about 360 nm. Similarly, Figure 54b shows a cross-section image of an NPG nanowire after etching allowing to recognize its internal nanoporous structure. During the etching process the Ag atoms are removed, leaving Au-rich zones. Diffusion of the Au atoms at the surface results in coarsening of the structure. The coarsening of the remaining Au results in a decrease of the diameter of the nanowire. In addition, Figure 54c–e show high-magnification cross-section images of the porous structure of the nanowire after dealloying for 60, 300, and 1200 s, respectively.
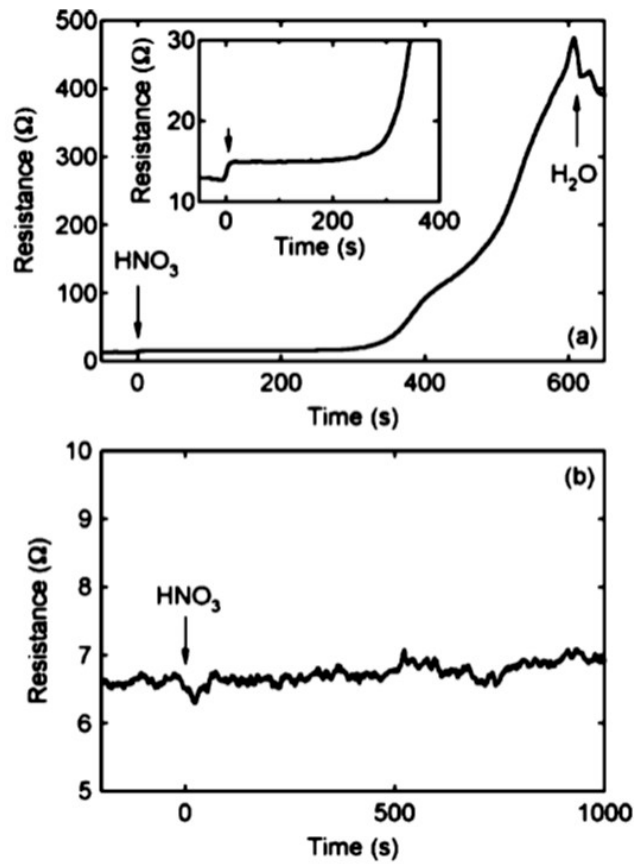
Figure 53. (**a**) Change in the resistance of the alloy $Au_{0.18}Ag_{0.82}$ nanowire during in situ dealloying by of a single HNO_3 etching. The inset reports an expanded plot of the resistance during the initial steps of etching. (**b**) Resistance the pure Au nanowire in dilute HNO_3, further increasing etching time. Reproduced with permission from [92]. Copyright American Chemical Society, 2006.

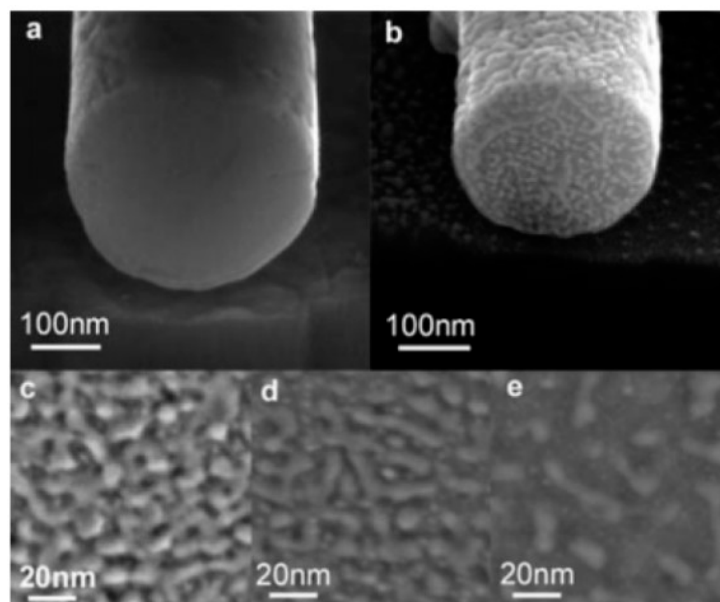**Figure 54.** Cross-sectional scanning electron microscopy micrograph of (**a**) a pure Au nanowire and (**b**) a NPG nanowire. Cross-sectional scanning electron microscopy micrograph of $Au_{0.18}Ag_{0.82}$ nanowires after in situ etching in HNO_3 for (**c**) 60 s, (**d**) 300 s, and (**e**) 1200 s. Reproduced with permission from [92]. Copyright American Chemical Society, 2006.

After 60 s of etching, Figure 54c, the HNO_3 has penetrated to the center of the nanowire and the morphology is relatively uniform. Considering Figure 54d,e, it is evident that the porosity continues to increase by increasing the dealloying time, indicating that Ag is still being removed from the nanowire. Using the scanning electron microscopy images, the authors evaluated that the diameter of the nanowire decreased to about 230 nm after 1200 s of etching and that the porosity reached about 60%, and, by using energy X-ray spectroscopy, that almost no Ag remained in the nanowire, indicating that the etching process is complete. The continued coarsening eventually results in break of the nanowire since both ends of the nanowire are constrained by the contact electrodes. At this point, the authors compare the resistance change during etching with the nanowire diameter and porosity, Figure 53a. After the initial increase, the resistance remains essentially constant for the next 4–5 min. During this time coarsening is relatively fast, resulting in a significant decrease in the diameter of the nanowires. The remaining Ag is also etched during this time so that there is little change in the porosity. At longer times coarsening continues, ultimately resulting in fracture of the Au ligaments in the porous structure and hence a rapid increase in the resistance. The analysis of the cross-section scanning electron microscopy images were, also, used to evaluate the mean Au ligament size in the porous structure versus the etching time: it increases from 0 s to 600 s where reaches a maximum value of about 15 nm and, then, decreases reaching the minimum value of about 7 nm after 1200 s. So, it is important to consider, according to the authors, that the mean free path for electrons in Au is about 50 nm significantly larger than the average ligament size: this means that the electrical conduction through the Au lugaments must be largely affected by the surface scattering processes. This is important in establishing the amperometric sensing properties of the NPG nanowires upon adsorbing the probing molecules on the Au ligaments surface. In fact, the change in the Au ligaments surface must result in significant change in the nanowire resistance. The resistance change is dominated by the change in surface scattering since the change in resistance is related to the increase in diffusive scattering at the surface due to the presence of adsorbates. At an ideal surface, all electrons are specularly reflected (elastically scattered with no change in momentum in the direction of the electric field).

The presence of adsorbates or other defects can lead to diffusive (inelastic) scattering of electrons that is associated with a change in momentum. Thus at a real surface, as long as the fraction of specularly reflected electrons is sufficiently large, then adsorption will introduce scattering centers that will increase the fraction of diffusively scattered electrons. If the dimensions of the solid are smaller than the electron mean free path such that the resistance is dominated by surface scattering, then adsorption can lead to a measurable change in resistance. In fact, Figure 55 reports the result of an experiment where small aliquots (5×10^{-11} mol) of ODT (octadecanethiol) were sequentially injected into the ethanol on the chip carrier. The initial resistance of the nanowire is 236 Ω, and each aliquot results in a 1 Ω increase in the resistance. On the basis of these results, upon plotting the resistance change versus the ODT surface concentration, the authors found a linear relation over all the investigated concentration range and a slope (sensitivity factor) of 1.0×10^{-16} cm^2.
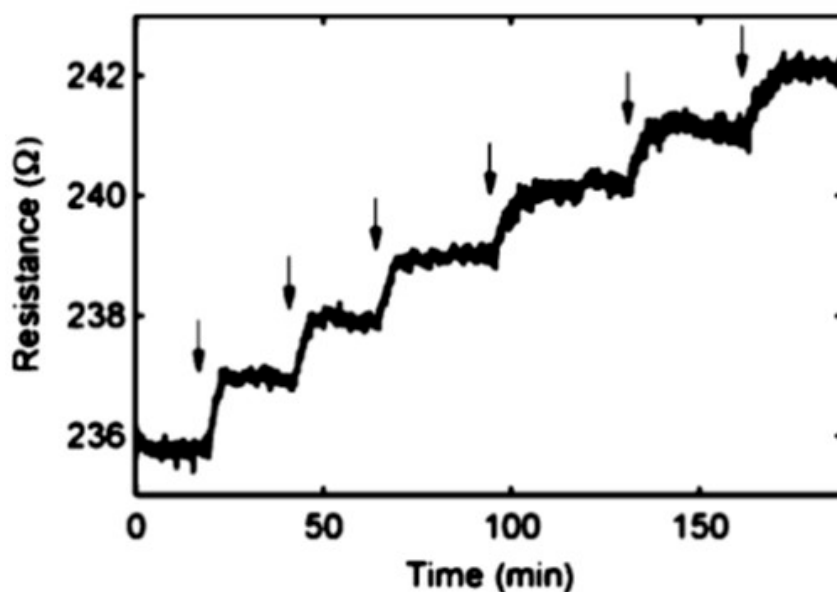
Figure 55. Resistance versus time for a single NPG nanowire device. The arrows indicate the injection of aliquots of 5×10^{-11} mol ODT. Reproduced with permission from [92]. Copyright American Chemical Society, 2006.

5. Conclusions

In this paper we reviewed the basic concepts related to the exploitation of NPG-based materials for sensing applications. In particular, we focused our attention on the use of NPG systems as optical-based or electrochemical-based sensing elements highlighting the possibility to control the NPG characteristics (as pores size, ligaments size, morphology and dimensionality) towards the design of sensing devices with advanced and desired sensitivity, selectivity, stability properties. The fine wide-range control of the NPG characteristics allows the wide-range tuning of its properties, such as the electrical, electrocatalytic, and optical ones, and we tried to set a general connecting scheme in view of the sensing applications optimization. The use of NPG-based leafs and films was extensively discussed in view of sensing applications. The combination of NPG leafs of films with other typology of nano-sized materials (Pt or CuO nanoscale thick films) was also discussed as a method to further improve the sensing performances. Finally, the role of nanostructured NPG-based materials (nanoparticles, nanodisks, nanowires) in improving devices sensing performances was discussed as a recent field of study and, possibly, as the main promising perspective in this framework.

References

1. Zhigal'skii, G.P.; Jones, B.K. *The Physical Properties of Thin Metal. Films*; Taylor and Francis: New York, NY, USA, 2003.
2. Barmak, K.; Coffey, K. *Metallic Films for Electronic, Optical and Magnetic Applications-Structure, Processing and Properties*; Woodhead Publishing: Cambridge, UK, 2014.
3. Johnston, R.L.; Wilcoxon, J.P. *Metal. Nanoparticles and Nanoalloys*; Elsevier: Amsterdam, The Netherlands, 2012.
4. Xiong, Y.; Lu, X. *Metallic Nanostructures-From Controlled Synthesis to Applications*; Springer: New York, NY, USA, 2014.
5. Cui, Z. *Nanofabrication-Principles, Capabilities, and Limits*; Springer: New York, NY, USA, 2008.

6.　Ruffino, F.; Crupi, I.; Simone, F.; Grimaldi, M.G. Formation and evolution of self-organized Au nanorings on indium-tin-oxide surface. *Appl. Phys. Lett.* **2011**, *98*, 023101.

7.　Sanzone, G.; Zimbone, M.; Cacciato, G.; Ruffino, F.; Carles, R.; Privitera, V.; Grimaldi, M.G. Ag/TiO₂ nanocomposite for visible light-driven photocatalysis. *Superlatt. Microstruct.* **2018**, *123*, 394–402.

8.　Gentile, A.; Ruffino, F.; Grimaldi, M.G. Complex-morphology metal-based nanostructures: Fabrication, characterization, and applications. *Nanomaterials* **2016**, *6*, 110.

9.　Ruffino, F.; Pugliara, A.; Carria, E.; Romano, L.; Bongiorno, C.; Fisicaro, G.; La Magna, A.; Spinella, C.; Grimaldi, M.G. Towards a laser fluence dependent nanostructuring of thin Au films on Si by nanosecond laser irradiation. *Appl. Surf. Sci.* **2012**, *258*, 9128–9137.

10.　Ruffino, F.; Grimaldi, M.G. Self-organized patterned arrays of Au and Ag nanoparticles by thickness-dependent dewetting of template-confined films. *J. Mater. Sci.* **2014**, *49*, 5714–5729.

11.　Ruffino, F.; De Bastiani, R.; Grimaldi, M.G.; Bongiorno, C.; Giannazzo, F.; Roccaforte, F.; Spinella, C.; Raineri, V. Self-organization of Au nanoclusters on the SiO₂ surface induced by 200 keV-Ar⁺ irradiation. *Nucl. Instr. Meth. Phys. Res. B* **2007**, *257*, 810–814.

12.　Mishra, Y.K.; Kabiraj, D.; Sulania, I.; Pivin, J.C.; Avasthi, D.K. Synthesis and characterization of gold nanorings. *J. Nanosci. Nanotechnol.* **2007**, *7*, 1878–1881.

13.　Mishra, Y.K.; Adelung, R.; Kumar, G.; Elbahri, M.; Mohapatra, S.; Singhal, R.; Tripathi, A.; Avasthi, D.K. Formation of Self-organized Silver Nanocup-Type Structures and Their Plasmonic Absorption. *Plasmonics* **2013**, *8*, 811–815.

14.　Maier, S.A. *Plasmonic: Fundamentals and Applications*; Springer: New York, NY, USA, 2007.

15.　Pelton, M.; Bryant, G. *Introduction to Metal-Nanoparticle Plasmonics*; Wiley: Hoboken, NJ, USA, 2013.

16.　Long, Y.-T.; Jing, C. *Localized surface plasmon resonance based nanobiosensors*; Springer: Heidelberg, Germany, 2014.

17.　Hodes, G. *Electrochemistry of Nanomaterials*; Wiley: Weinheim, Germany, 2001.

18.　Eftekhari, A. *Nanostructured materials in electrochemistry*; Wiley: Weinheim, Germany, 2008.

19.　Pumera, M. *Nanomaterials for Electrochemical Sensing and Biosensing*; CRC Press: Boca Raton, FL, USA, 2013.

20.　Van der Zalm, J.; Chen, S.; Huang, W.; Chen, A. Review-Recent Advances in the Development of Nanoporous Au for Sensing Applications. *J. Electrochem. Soc.* **2020**, *167*, 037532.

21.　Xu, Q. *Nanoporous Materials-Synthesis and Applications*; CRC Press: Boca Raton, FL, USA, 2013.

22.　Wittstock, A.; Biener, J.; Erlebacher, J.; Bäumer, M. *Nanoporous Gold-From Ancient Technology to a High.-Tech. Material*; RSC Publishing: Dorchester, UK, 2012.

23.　Kim, S.H. Nanoporous Gold: Preparation and applications to catalysis and sensors. *Curr. Appl. Phys.* **2018**, *18*, 810–818.

24.　Ding, Y.; Kim, Y.-J.; Erlebacher, J. Nanoporous Gold Leaf: "Ancient Technology"/Advanced Material. *Adv. Mater.* **2004**, *16*, 1897–1900.

25.　Yan, M. *Development of New Catalytic Performance of Nanoporous Metals for Organic Reactions*; Springer: Tokyo, Japan, 2014.

26.　Webster, T.J. *Nanomedicine-Technologies and Applications*; Woodhead Publishing: Cambridge, UK, 2012.

27.　Tan, Y.H.; Davis, J.A.; Fujikawa, K.; Ganesh, N.V.; Demchenko, A.V.; Stine, K.J. Surface area and pore size characteristics of nanoporous gold subjected to thermal, mechanical, or surface modification studied using gas adsorption isotherms, cyclic voltammetry, thermogravimetric analysis, and scanning electron microscopy. *J. Mater. Chem.* **2012**, *22*, 6733–6745.

28.　Grillo, R.; Torrisi, V.; Ruffino, F. Nanoporous Au: An experimental study on the porosity of dealloyed AuAg leafs. *Superlatt. Microstruct.* **2016**, *100*, 780–791.

29.　Abdelaziz, R.; Disci-Zayed, D.; Hedayati, M.K.; Pöhls, J.-H.; Zillohu, A.U.; Erkartal, B.; Chakravadhanula, V.S.K.; Duppel, V.; Kienle, L.; Elbahri, M. Green chemistry and nanofabrication in a levitated Leidenfrost drop. *Nat. Comm.* **2013**, *4*, 2400.

30.　Ruffino, F.; Torrisi, V.; Griallo, R.; Cacciato, G.; Zimbone, M.; Piccitto, G.; Grimaldi, M.G. Nanoporous Au structures by dealloying Au/Ag thermal- or laser-dewetted bilayers on surfaces. *Superlatt. Microstruct.* **2017**, *103*, 28–47.

31.　Volkert, C.A.; Lilleodden, E.T.; Kramer, D.; Weissmüller, J. Approaching the theoretical strength in nanoporous Au. *Appl. Phys. Lett.* **2006**, *89*, 061920.

32.　Qian, L.H.; Chen, M.W. Ultrafine nanoporous gold by low-temperature dealloying and kinetics of nanopore formation. *Appl. Phys. Lett.* **2007**, *91*, 083105.

33. Chen, A.Y.; Shi, S.S.; Liu, F.; Wang, Y.; Li, X.; Gu, J.F.; Xie, X.F. Effect of annealing atmosphere on coarsening of nanoporous gold films. *Appl. Surf. Sci.* **2015**, *355*, 133–138.

34. Chen-Wiegart, Y.-C.K.; Wang, S.; Chu, Y.S.; Liu, W.; McNulty, I.; Voorhees, P.W.; Dunand, D.C. Structural evolution of nanoporous gold during thermal coarsening. *Acta Mater.* **2012**, *60*, 4972–4981.

35. Chen-Wiegart, Y.-C.K.; Wang, S.; Lee, W.-K.; McNulty, I.; Voorhees, P.W.; Dunand, D.C. In situ imaging of dealloying during nanoporous gold formation by transmission x-ray microscopy. *Acta. Mater.* **2013**, *61*, 1118–1125.

36. Chen-Wiegart, Y.-C.K.; Wang, S.; McNulty, I.; Voorhees, P.W.; Dunand, D.C. Effect of Ag-Au composition and acid concentration on dealloying front velocity and cracking during nanoporous gold formation. *Acta. Mater.* **2013**, *61*, 5561–5570.

37. Van Petegem, S.; Brandstetter, S.; Maass, R.; Hodge, A.M.; El-Dasher, B.S.; Biener, J.; Schmitt, B.; Borca, C.; Van Swygenhoven, H. On the microstructure of nanoporous gold: An x-ray diffraction study. *Nano Lett.* **2009**, *9*, 1158–1163.

38. Fujita, T.; Qian, L.-H.; Inoke, K.; Erlebacher, J.; Chen, M.-W. Three-dimensional morphology of nanoporous gold. *Appl. Phys. Lett.* **2008**, *92*, 251902.

39. El Mel, A.-A.; Boukli-Hacene, F.; Molina-Luna, L.; Bouts, N.; Chauvin, A.; Thiry, D.; Gautron, E.; Gautier, N.; Tessier, P.-Y. Unusual dealloying effect in gold/copper alloy thin films: The role of defects and column boundaries in the formation of nanoporous gold. *ACS Appl. Mater. Interf.* **2015**, *7*, 2310–2321.

40. Dotzler, C.J.; Ingham, B.; Illy, B.N.; Wallwork, K.; Ryan, M.P.; Toney, M.F. In situ observation of strain development and porosity evolution in nanoporous gold foils. *Adv. Funct. Mater.* **2011**, *21*, 3938–3946.

41. Biener, J.; Hodge, A.M.; Hamza, A.V. Microscopic failure behavior of nanoporous gold. *Appl. Phys. Lett.* **2005**, *87*, 121908.

42. Mathur, A.; Erlebacher, J. Size dependence of effective Young's modulus of nanoporous gold. *Appl. Phys. Lett.* **2007**, *90*, 061910.

43. Detsi, E.; Chen, Z.G.; Vellinga, W.P.; Onck, P.R.; De Hosson, J.T.M. Reversible strain by physisorption in nanoporous gold. *Appl. Phys. Lett.* **2011**, *99*, 083104.

44. Wahl, P.; Traußnig, T.; Landgraf, S.; Jin, H.-J.; Weissmüller, J.; Würschum, R. Adsorption-driven tuning of the electrical resistance of nanoporous gold. *J. Appl. Phys.* **2010**, *108*, 073706.

45. Hopkins, P.E.; Serrano, J.R.; Phinney, L.M.; Li, H.; Misra, A. Boundary scattering effects during electron thermalization in nanoporous gold. *J. Appl. Phys.* **2011**, *109*, 013524.

46. Smith, G.B.; Maaroof, A.I.; Cortie, M.B. Percolation in nanoporous gold and the principle of universality for two-dimensional to hyperdimensional networks. *Phys. Rev. B* **2008**, *78*, 165418.

47. Zheng, L.-T.; Wei, Y.-L.; Gong, H.-Q.; Qian, L. Application Progress of Nanoporous Gold in Analytical Chemistry. *Chinese J. Anal. Chem.* **2013**, *41*, 137–144.

48. Bhattarai, J.K.; Neupane, D.; Nepal, B.; Mikhaylov, V.; Demchenko, A.V.; Stine, K.J. *Structure and Applications of Gold in Nanoporous Form*; IntechOpen: Rijeka, Croatia, 2018.

49. Collinson, M.M. Nanoporous Gold Electrodes and Their Applications in Analytical Chemistry. *ISRN Anal. Chem.* **2013**, *2013*, 692484.

50. Wittstock, A.; Biener, J.; Bäumer, M. Nanoporous Gold: A new material for catalytic and sensor applications. *Phys. Chem. Chem. Phys.* **2010**, *12*, 12919–12930.

51. Seker, E.; Reed, M.L.; Begley, M.R. Nanoporous Gold: Fabrication, Characterization, and Applications. *Materials* **2009**, *2*, 2188–2215.

52. Biener, J.; Wittstock, A.; Baumann, T.F.; Weissmüller, J.; Bäumer, M.; Hamza, A.V. Surface Chemistry in Nanoscale Materials. *Materials* **2009**, *2*, 2404–2428.

53. Kucheyev, S.O.; Hayes, J.R.; Biener, J.; Huser, T.; Talley, C.E.; Hamza, A.V. Surface-enhanced Raman scattering on nanoporous Au. *Appl. Phys. Lett.* **2006**, *89*, 053102.

54. Chen, A.Y.; Shi, S.S.; Qiu, Y.D.; Xie, X.F.; Ruan, H.H.; Gu, J.F.; Pan, D. Pore-size tuning and optical performances of nanoporous gold films. *Microporous Mesoporous Mater.* **2015**, *202*, 50–56.

55. Lang, X.Y.; Guan, P.F.; Zhang, L.; Fujita, T.; Chen, M.W. Characteristic length and temperature dependence of surface enhanced Raman scattering of nanoporous gold. *J. Phys. Chem. C* **2009**, *113*, 10956–10961.

56. Lang, X.Y.; Guan, P.F.; Fujita, T.; Chen, M.W. Tailored nanoporous gold for ultrahigh fluorescence enhancement. *Phys. Chem. Chem. Phys.* **2011**, *13*, 3795–3799.

57. Zhang, L.; Chang, H.; Hirata, A.; Wu, H.; Xue, Q.-K.; Chen, M. Nanoporous gold based optical sensor for sub-ppt detection of mercury ions. *ACS Nano* **2013**, *7*, 4595–4600.

58. Ruffato, G.; Garoli, D.; Cattarin, S.; Barison, S.; Natali, M.; Canton, P.; Benedetti, A.; De Salvador, D.; Romanato, F. Patterned nanoporous-gold thin layers: Structure control and tailoring of plasmonic properties. *Microporous Mesoporous Mater.* **2012**, *163*, 153–159.

59. Jiao, Y.; Ryckman, J.D.; Ciesielski, P.N.; Escobar, C.A.; Jennings, G.K.; Weiss, S.M. Patterned nanoporous gold as an effective SERS template. *Nanotechnology* **2011**, *22*, 295302.

60. Ruffato, G.; Romanato, F.; Garoli, D.; Cattarin, S. Nanoporous gold plasmonic structures for sensing applications. *Optics Express* **2011**, *19*, 13164–13170.

61. Qian, L.H.; Yan, X.Q.; Fujita, T.; Inoue, A.; Chen, M.W. Surface enhanced Raman scattering of nanoporous gold: Smaller pore sizes stronger enhancements. *Appl. Phys. Lett.* **2007**, *90*, 153120.

62. Qian, L.H.; Inoue, A.; Chen, M.W. Large surface enhanced Raman scattering enhancements from fracture surfaces of nanoporous gold. *Appl. Phys. Lett.* **2008**, *92*, 093113.

63. Lang, X.Y.; Chen, L.Y.; Guan, P.F.; Fujita, T.; Chen, M.W. Geometric effect on surface enhanced Raman scattering of nanoporous gold: Improving Raman scattering by tailoring ligament and nanopore ratios. *Appl. Phys. Lett.* **2009**, *94*, 213109.

64. Lang, X.Y.; Guan, P.F.; Zhang, L.; Fujita, T.; Chen, M.W. Size dependence of molecular fluorescence enhancement of nanoporous gold. *Appl. Phys. Lett.* **2010**, *96*, 073701.

65. Lang, X.; Qian, L.; Guan, P.; Zi, J.; Chen, M. Localized surface plasmon resonance of nanoporous gold. *Appl. Phys. Lett.* **2011**, *98*, 093701.

66. Kim, N.; Choi, M.; Leem, J.W.; Yu, J.S.; Kim, T.W.; Kim, T.-S.; Byun, K.M. Improved biomolecular detection based on a plasmonic nanoporous gold film fabricated by oblique angle deposition. *Opt. Express* **2015**, *23*, 18777.

67. Chen, H.-A.; Long, J.-L.; Lin, Y.-H.; Weng, C.-J.; Lin, H.-N. Plasmonic properties of a nanoporous gold film investigated by far-field and near-field optical techniques. *J. Appl. Phys.* **2011**, *110*, 054302.

68. Dixon, M.C.; Daniel, T.A.; Hieda, M.; Smilgies, D.M.; Chan, M.H.W.; Allara, D.L. Preparation, structure, and optical properties of nanoporous gold thin films. *Langmuir* **2007**, *23*, 2414–2422.

69. Jalas, D.; Canchi, R.; Petrov, A.Yu.; Lang, S.; Shao, L.; Weissmüller, J.; Eich, M. Effective medium model for the spectral properties of nanoporous gold in the visible. *Appl. Phys. Lett.* **2014**, *105*, 241906.

70. Detsi, E.; Salverda, M.; Onck, P.R.; De Hosson, J.T.M. On the localized surface plasmon resonance modes in nanoporous gold films. *J. Appl. Phys.* **2014**, *115*, 044308.

71. Yu, F.; Ahl, S.; Caminade, A.-M.; Majoral, J.-P.; Knoll, W.; Erlebacher, J. Simultaneous excitation of propagating and localized surface plasmon resonance in nanoporous gold membranes. *Anal. Chem.* **2006**, *78*, 7346–7350.

72. Maarof, A.I.; Gentle, A.; Smith, G.B.; Cortie, M.B. Bulk and surface plasmons in highly nanoporous gold films. *J. Phys. D Appl. Phys.* **2007**, *40*, 5675.

73. Zhang, L.; Lang, X.; Hirata, A.; Chen, M. Wrinkled nanoporous gold films with ultrahigh surface-enhanced Raman scattering enhancement. *ACS Nano* **2011**, *5*, 4407–4413.

74. Liu, Z.; Du, J.; Qiu, C.; Huang, L.; Ma, H.; Shen, D.; Ding, Y. Electrochemical sensor for detection of p-nitrophenol based on nanoporous gold. *Electrochem. Commun.* **2009**, *11*, 1365–1368.

75. Meng, F.; Yan, X.; Liu, J.; Gu, J.; Zou, Z. Nanoporous gold as non-enzymatic sensor for hydrogen peroxide. *Electrochim. Acta* **2011**, *56*, 4657–4662.

76. Chen, L.Y.; Lang, X.Y.; Fujita, T.; Chen, M.W. Nanoporous gold for enzyme-free electrochemical glucose sensors. *Scr. Mater.* **2011**, *65*, 17–20.

77. Daggumati, P.; Matharu, Z.; Seker, E. Effect of nanoporous gold thin film morphology on electrochemical DNA sensing. *Anal. Chem.* **2015**, *87*, 8149–8156.

78. Xiao, X.; Ulstrup, J.; Li, H.; Wang, M.; Zhang, J.; Si, P. Nanoporous gold assembly of glucose oxidase for electrochemical biosensing. *Electrochim. Acta* **2014**, *130*, 559–567.

79. Chen, A.Y.; Wang, J.W.; Wang, Y.; Jia, Y.Q.; Gu, J.F.; Xie, X.F.; Pan, D. Effects of pore size and residual Ag on the electrocatalytic properties of nanoporous gold films prepared by pulse electrochemical dealloying. *Electrochim. Acta* **2015**, *153*, 552–558.

80. Graf, M.; Haensch, M.; Carstens, J.; Wittstock, G.; Weissmüller, J. Electrocatalytic methanol oxidation with nanoporous gold: Microstructure and selectivity. *Nanoscale* **2017**, *9*, 17839–17848.

81. Wang, X.; Frenzel, J.; Wang, W.; Ji, H.; Qi, Z.; Zhang, Z.; Eggeler, G. Length-scale modulated and electrocatalytic activity enhanced nanoporous gold by doping. *J. Pys. Chem. C* **2011**, *115*, 4456–4465.

82. Qiu, H.; Huang, X. Effects of Pt decoration on the electrocatalytic activity of nanoporous gold electrode toward glucose and its potential application for constructing a nonenzymatic glucose sensor. *J. Electroanal. Chem.* **2010**, *643*, 39–45.

83. Ge, X.; Wang, R.; Liu, P.; Ding, Y. Platinum-decorated nanoporous gold leafs for methanol electrooxidation. *Chem. Mater.* **2007**, *19*, 5827–5829.

84. Xiao, X.; Wang, M.; Li, H.; Pan, Y.; Si, P. Non-enzymatic glucose sensors based on controllable nanoporous gold/copper oxide nanohybrids. *Talanta* **2014**, *125*, 366.371.

85. Hu, K.; Lan, D.; Li, X.; Zhang, S. Electrochemical DNA biosensor based on nanoporous gold electrode and multifunctional encoded DNA-Au bio bar codes. *Anal. Chem.* **2008**, *80*, 9124–9130.

86. Qiu, H.; Xue, L.; Ji, G.; Zhou, G.; Huang, X.; Qu, Y.; Gao, P. Enzyme-modified nanoporous gold-based electrochemical biosensors. *Biosensors Bioelectron.* **2009**, *24*, 3014–3018.

87. Quynh, B.T.P.; Byun, J.Y.; Kim, S.H. Non-enzymatic amperometric detection of phenol and catechol using nanoporous gold. *Sensors Actuators B* **2015**, *221*, 191–200.

88. Ge, X.; Wang, L.; Liu, Z.; Ding, Y. Nanoporous gold leaf for amperometric determination of nitrite. *Electroanalysis* **2011**, *23*, 381–386.

89. Xia, Y.; Huang, W.; Zheng, J.; Niu, Z.; Li, Z. Nonenzymatic amperometric response of glucose on a nanoporous gold film electrode fabricated by a rapid and simple electrochemical method. *Biosensors Bioelectron.* **2011**, *26*, 3555–3561.

90. Seo, B.; Kim, J. Electrooxidation of glucose at nanoporous gold surfaces: Structure dependent electrocatalysis and its application to amperometric detection. *Electroanalysis* **2010**, *22*, 939–945.

91. Guo, M.-M.; Wang, P.-S.; Zhou, C.-H.; Xia, Y.; Huang, W.; Li, Z. An ultrasensitive non-enzymatic amperometric glucose sensor based on a Cu-coated nanoporous gold film involving co-mediating. *Sensors Actuators B* **2014**, *203*, 388–395.

92. Liu, Z.; Searson, P.C. Single nanoporous gold nanowire sensors. *J. Phys. Chem. B* **2006**, *110*, 4318–4322.

93. Shih, W.-C.; Santos, G.M.; Zhao, F.; Zenasni, O.; Arnob, M.P. Simultaneous chemical and refractive index sensing in the 1-2.5 μm near-infrared wavelength range on nanoporous gold disks. *Nano Lett.* **2016**, *16*, 4641–4647.

94. Santos, G.M.; Zhao, F.; Zeng, J.; Li, M.; Shih, W.-C. Label-free, zeptomole cancer biomarker detection by surface-enhanced fluorescence on nanoporous gold disk plasmonic nanoparticles. *J. Biophotonics* **2015**, *8*, 855–863.

95. Zeng, J.; Zhao, F.; Qi, J.; Li, Y.; Li, C.-H.; Yao, Y.; Randall Lee, T.; Shih, W.-C. Internal and external morphology-dependent plasmonic resonance in monolithic nanoporous gold nanoparticles. *RSC Adv.* **2014**, *4*, 36682–36688.

96. Wang, D.; Ji, R.; Albrecht, A.; Schaaf, P. Ordered arrays of nanoporous gold nanoparticles. *Beilstein J. Nanotechnol.* **2012**, *3*, 651–657.

97. Wang, D.; Schaaf, P. Nanoporous gold nanoparticles. *J. Mater. Chem.* **2012**, *22*, 5344–5348.

98. Wang, D.; Schaaf, P. Plasmonic nanosponges. *Adv. Phys. X* **2018**, *3*, 1456361.

99. Vidal, C.; Sivun, D.; Ziegler, J.; Wang, D.; Schaaf, P.; Hrelescu, C.; Klar, T.A. Plasmonic horizon in gold nanosponges. *Nano Lett.* **2018**, *18*, 1269–1273.

100. Arnob, M.M.P.; Zhao, F.; Zeng, J.; Santos, G.M.; Li, M.; Shih, W.-C. Laser rapid thermal annealing enables tunable plasmonics in nanoporous gold nanoparticles. *Nanoscale* **2014**, *6*, 12470–12475.

101. Zeng, J.; Zhao, F.; Li, M.; Li, C.-H.; Randall Lee, T.; Shih, W.-C. Morphological control and plasmonic tuning of nanoporous gold disks by surface modifications. *J. Mater. Chem. C* **2015**, *3*, 247–252.

102. Rao, W.; Wang, D.; Kups, T.; Baradácas, E.; Parditka, Z.; Schaaf, P. Nanoporous gold nanoparticles and Au/Al$_2$O$_3$ hybrid nanoparticles with large tunability of plasmonic properties. *ACS Appl. Mater. Interf.* **2017**, *9*, 6273–6281.

103. Chauvin, A.; Delacôte, C.; Molina.Luna, L.; Duerrschnabel, M.; Boujtita, M.; Thiry, D.; Du, K.; Ding, J.; Choi, C.-H.; Tessier, P.-Y.; et al. Planar arrays of nanoporous gold nanowires: When electrochemical dealloying meets nanopatterning. *ACS Appl. Mater. Interf.* **2016**, *8*, 6611–6620.

104. Zhang, J.; Li, C.M. Nanoporous metals: Fabrication strategies and advanced electrochemical applications in catalysis, sensing and energy systems. *Chem. Soc. Rev.* **2012**, *41*, 7016–7031.

105. Ruffino, F.; Canino, A.; Grimaldi, M.G.; Giannazzo, F.; Bongiorno, C.; Roccaforte, F.; Raineri, V. Self-organization of nanoclusters on hexagonal SiC and SiO$_2$ surfaces. *J. Appl. Phys.* **2007**, *101*, 064306.

106. Erlebacher, J.; Aziz, M.J.; Karma, A.; Dimitrov, N.; Sieradzki, K. Evolution of nanoporosity in dealloying. *Nature* **2001**, *410*, 450–453.

107. Parida, S.; Kramer, D.; Volkert, C.A.; Rosner, H.; Erlebacher, J.; Weissmuller, J. Volume Change during the Formation of Nanoporous Gold by Dealloying. *Phys. Rev. Lett.* **2006**, *97*, 035504.

108. Gunnarsson, L.; Bjerneld, E.J.; Xu, X.; Petronis, S.; Kasemo, B.; Kall, M. Interparticle coupling effects in nanofabricated substrates for surface-enhanced Raman scattering. *Appl. Phys. Lett.* **2001**, *78*, 802–804.

109. Gorji, N.E.; Saxena, P.; Corfield, M.; Clare, A.; Rueff, J.-P.; Bogan, J.; González, P.G.M.; Snelgrove, M.; Hughes, G.; O'Connor, R.; et al. A new method for assessing the recyclability of Powder Bed Fusion process. *Mater. Charact.* **2020**, *161*, 110167.

110. Goldstein, J.I.; Newbury, D.E.; Michael, J.R.; Ritchie, N.W.M.; Scott, J.H.J.; Joy, D.C *Scanning Electron. Microscopy and X-Ray Microanalysis*; Springer: New York, NY, USA, 2018.

111. Khristosov, M.K.; Dishon, S.; Noi, I.; Katsman, A.; Pokroy, B. Pore and ligament size control, thermal stability and mechanical properties of nanoporous single crystals of gold. *Nanoscale* **2017**, *9*, 14458–14466.